DOKUZ EYLÜL UNIVERSITY
GRADUATE SCHOOL OF NATURAL AND APPLIED SCIENCES

PERFORMANCE ASSESSMENT OF ANION EXCHANGE MEMBRANE ELECTROLYZER THROUGH MATHEMATICAL MODELING

Ceren ÇELEBİ

December, 2025

İZMİR

PERFORMANCE ASSESSMENT OF ANION EXCHANGE MEMBRANE ELECTROLYZER THROUGH MATHEMATICAL MODELING

A Thesis Submitted to the
Graduate School of Natural and Applied Sciences of Dokuz Eylül University
In Partial Fulfillment of the Requirements for Master of Science in
Department of Mechanical Engineering, Thermodynamics Program

by

Ceren ÇELEBİ

December, 2025

İZMİR

M.Sc THESIS EXAMINATION RESULT FORM

We have read the thesis entitled **"PERFORMANCE ASSESSMENT OF ANION EXCHANGE MEMBRANE ELECTROLYZER THROUGH MATHEMATICAL MODELING "** completed by **CEREN ÇELEBİ** under supervision of **PROF.DR. CAN ÖZGÜR ÇOLPAN** and **PROF.DR. YILSER DEVRİM** and we certify that in our opinion it is fully adequate, in scope and in quality, as a thesis for the degree of Master of Science.

Prof.Dr. Can Özgür ÇOLPAN	Prof.Dr.Yılser DEVRİM
Supervisor	Co-Supervisor
Prof.Dr. Azize AYOL	Prof.Dr. Hadi GENCELİ
Jury Member	Jury Member

Assoc.Prof.Dr. Mustafa Umut KARAOĞLAN

Jury Member

Prof. Dr. Abdullah SEÇGİN

Director

Graduate School of Natural and Applied Sciences

ACKNOWLEDGMENT

The author wishes to express her deepest gratitude to her supervisor, Prof. Dr. Can Özgür ÇOLPAN, for his invaluable supervision, guidance, support, and insight throughout the entire research process.

The author also extends her sincere appreciation to Prof. Dr. Yılser DEVRİM for her supervision, advice, and support, as well as for her guidance and contributions through the TÜBİTAK 1001 Project (Grant No: 123M878).

The author is profoundly grateful to Prof. Dr. Mehmet Akif EZAN, who greatly contributed to enriching this thesis with his valuable comments, encouragement, and constructive feedback. His academic contributions and continuous support are sincerely appreciated.

Special thanks are extended to the jury members, Prof. Dr. Azize AYOL, Prof. Dr. Hadi GENCELİ, and Assoc. Prof. Dr. Mustafa Umut KARAOĞLAN, for their valuable time, comments, and contributions to the evaluation of this thesis.

The author would also like to acknowledge the Scientific and Technological Research Council of Turkey (TÜBİTAK) for the financial support provided under the 1001 Program (Grant No: 123M878) throughout her MSc studies.

Finally, the author expresses her heartfelt gratitude to her family and close friends for their endless love, patience, and unconditional support throughout her life.

Ceren ÇELEBİ

PERFORMANCE ASSESSMENT OF ANION EXCHANGE MEMBRANE ELECTROLYZER THROUGH MATHEMATICAL MODELING

ABSTRACT

The anion exchange membrane water electrolyzer (AEMWE) is a promising technology for green hydrogen production due to its ability to maintain high efficiency while using cost-effective transition metals. The objective of this thesis is to develop modeling approaches that evaluate the electrochemical, thermal, and system-level behavior of AEMWE. First, a zero-dimensional model was developed to evaluate the electrochemical performance of the AEMWE cell, then used to compare the performance of different polybenzimidazole-based membranes at various operating temperatures and membrane thicknesses. Following this, the heating behavior of the electrolyzer stack and electrolyte tank was analyzed at the system level using MATLAB/Simulink. Finally, a system with photovoltaics (PV) and metal hydride (MH) tanks was modeled, and the hydrogen production and storage performance under typical July and January conditions in Izmir was investigated. The findings indicate that thinner membranes and higher operating temperatures increase system efficiency. The highest efficiency of 83.89%, based on higher heating value, was achieved at a current density of 20,000 A/m^2 using a 25 μm membrane operated at 80 °C in a 1 M potassium hydroxide solution. System-level results revealed that low tank mass and slower water inlet flow rates led to faster heating of the stack. The proposed PV-AEMWE-MH system can produce 0.295 and 0.1656 kg of hydrogen daily during summer and winter, respectively. The analyses showed that low convection coefficients reduce storage efficiency, as the tank temperature exceeds its operational limits, and the impact of higher values is not pronounced after a certain point.

Keywords: Anion exchange membrane water electrolyzer (AEMWE), polybenzimidazole (PBI), thermal management, metal hydride (MH), MATLAB/Simulink

MATEMATİKSEL MODELLEME İLE ANYON DEĞİŞİM MEMBRAN ELEKTROLİZÖRÜN PERFORMANS DEĞERLENDİRİLMESİ

ÖZ

Anyon değişim membran su elektrolizörü (AEMWE), uygun maliyetli geçiş metalleri kullanırken yüksek verimliliğini koruyabilmesi sayesinde yeşil hidrojen üretimi için umut vadeden bir teknolojidir. Bu çalışmanın amacı, AEMWE'nin elektrokimyasal, ısıl ve sistem düzeyindeki davranışlarını değerlendiren modelleme yaklaşımlarının geliştirilmesidir. Öncelikli olarak, AEMWE hücresinin elektrokimyasal performansını değerlendirmek amacıyla sıfır boyutlu detaylı bir model geliştirilmiş ve bu model aracılığıyla farklı polibenzimidazol temelli membranların farklı çalışma sıcaklıklarındaki ve membran kalınlıklarındaki performansları karşılaştırılmıştır. Ardından elektrolizör yığınının ve elektrolit tankının ısınma davranışı MATLAB ve Simulink ortamında sistem düzeyinde analiz edilmiştir. Son olarak, fotovoltaik (PV) ile beslenen ve metal hidrür (MH) tanklarıyla entegre edilmiş bir PV-AEMWE-MH sistemi modellenmiş ve İzmir'in tipik temmuz ve ocak ayı güneş koşulları altında hidrojen üretim ve depolama performansı incelenmiştir. Bulgular, daha ince membranların ve daha yüksek çalışma sıcaklıklarının sistem verimliliğini artırdığını göstermektedir. En yüksek verim, 25 μm membran kalınlığında, 80 °C çalışma sıcaklığında ve 1 M potasyum hidroksit elektrolitiyle çalışıldığında, 20.000 A/m^2 akım yoğunluğunda %83,89 yüksek ısıl değer esaslı verimlilik ile elde edilmiştir. Sistem seviyesindeki sonuçlar, düşük tank kütlesi ve yavaş su giriş debilerinin yığının daha hızlı ısınmasına yol açtığını ortaya koymuştur. PV-AEMWE-MH sisteminin yaz ayında günde yaklaşık 0,295 kg, kış ayında ise yaklaşık 0,1656 kg hidrojen üretebildiği belirlenmiştir. Yaz koşullarında düşük taşınım katsayılarında yetersiz ısı uzaklaştırılması nedeniyle depolama performansı düşerken, her iki mevsim için de belirli bir eşik değerin üzerindeki taşınım katsayılarında depolama performansındaki iyileşmenin sınırlı kaldığı görülmüştür.

Anahtar kelimeler: Anyon değişim membran su elektrolizörü (AEMWE), polibenzimidazol (PBI), ısıl yönetim, metal hidrür (MH), MATLAB/Simulink

CONTENTS

Page

M.Sc THESIS EXAMINATION RESULT FORM ii
ACKNOWLEDGMENT iii
ABSTRACT iv
ÖZ v
CONTENTS vi
LIST OF FIGURES viii
LIST OF TABLES xii
LIST OF SYMBOLS xiii
ABBREVIATIONS xv

CHAPTER ONE – INTRODUCTION 1

1.1 Introduction 1
1.2. Scope and Objectives 2
1.3. Thesis Outline 3

CHAPTER TWO – BACKGROUND AND LITERATURE REVIEW 5

2.1 Overview of Electrolysis Technologies 5
2.1.1 Alkaline Water Electrolyzer (AWE) 7
2.1.2 Proton Exchange Membrane Water Electrolyzer (PEMWE) 9
2.1.3 Anion Exchange Membrane Water Electrolyzer (AEMWE) 10
2.1.4 Solid Oxide Water Electrolyzer (SOEC) 11
2.1.5 Comparison of Water Electrolyzer Technologies 14
2.2 Anion Exchange Membrane Electrolyzer (AEMWE) 19
2.2.1 Principles of AEMWE 19
2.2.2 Performance Assessment of Water Electrolyzer 25
2.2.3 Materials for AEMWE 28
2.2.4 Selection of Membrane for AEMWE 29
2.3 System Architectures of AEMWE-Based Systems 31
2.3.1 Balance of Plant Components 31

2.3.2 System-Level Modeling Studies 34

CHAPTER THREE – METHODOLOGY 39

3.1 AEMWE Modeling 39
3.1.1 Cell-Level Modeling of AEMWE 39
3.1.1.1 Thermodynamic Cell Voltage 40
3.1.1.2 Overpotentials in AEMWE 41
3.1.2 System-Level Modeling of AEMWE 44
3.1.2.1 Modeling of Balance of Plant 45
3.1.2.2 Integration with Renewable Power and Storage Technologies . 51

CHAPTER FOUR – RESULTS AND DISCUSSION 62

4.1 Performance of AEMWE Based on PBI Membrane 62
4.2 Performance of AEMWE System 75
4.2.1 Simulation of AEMWE including Balance of Plant Components 75
4.2.2 Simulation of Integrated PV-AEMWE-MH System 82

CHAPTER FIVE – CONCLUSIONS 106

REFERENCES 109

LIST OF FIGURES

Page

Figure 2.1 Classification of hydrogen production routes. 5

Figure 2.2 Schematic representation of an alkaline water electrolyzer 7

Figure 2.3 Schematic representation of a proton exchange water electrolyzer 9

Figure 2.4 Schematic representation of an anion exchange membrane water electrolyzer 10

Figure 2.5 a) Proton-conducting solid oxide electrolysis cells (H-SOEC) b) oxygen ion-conducting solid oxide electrolysis cells (O-SOEC) 12

Figure 2.6 Schematic illustration of the primary hydroxide transport mechanisms in AEMs. 19

Figure 2.7 Water transport mechanisms in AEMWEs. 23

Figure 2.8 Typical system design and Balance of Plant (BoP) for an anion exchange membrane (AEM) electrolyzer 32

Figure 3.1 Recirculation and cooling concept of the electrolyzer system 45

Figure 3.2 Circulation of the electrolyte between the tank and the stack. 46

Figure 3.3 Energy balance of electrolyzer stack 46

Figure 3.4 Energy balance of electrolyte tank 48

Figure 3.5 Balance of Plant of AEMWE stack in Simulink 49

Figure 3.6 System schematic of PV-AEMWE-MH integration 52

Figure 3.7 MPPT system configuration for PV 53

Figure 3.8 Logic of MPPT 54

Figure 3.9 AEMWE-PV integration in Simulink 55

Figure 3.10 Electrolyzer Power Management Subsystem 55

Figure 3.11 Simulink architecture of the integrated metal hydride tank coupled with the electrolyzer hydrogen supply system 60

Figure 4.1 Variation of Nernst Voltage with temperature and a) pressure and b) molarity, highlighting the combined effects of these parameters 65

Figure 4.2 Comparison of model results with experimental data (Hager et al., 2023), depicting cell voltage and IR-corrected cell voltage versus current density 66

Figure 4.3 a) Absolute and b) squared error between model results and experimental data (Hager et al., 2023) 67

Figure 4.4 Variation of overpotential contributions and resulting cell voltage relative to current density 68

Figure 4.5 Cell voltage and HHV Efficiency for different PBI-based membranes . 70

Figure 4.6 Cell voltage and efficiency for varying a) temperatures, b) membrane thicknesses using P4HexPipSt/OPBI membrane 72

Figure 4.7 Cell voltage and efficiency for varying a) temperatures, b) membrane thicknesses using ABPBI-c-PVBC/OH 1:2 membrane 73

Figure 4.8 a) Time-dependent cell voltage and current density b) V-I curve 76

Figure 4.9 The stack and tank temperatures over time 76

Figure 4.10 Comparing the approaches of enthalpy calculations 77

Figure 4.11 Effects of the water tank mass on stack temperature 78

Figure 4.12 Effects of the inlet water mass flow rate on stack temperature 79

Figure 4.13 Effects of heat capacity on stack temperature 80

Figure 4.14 Comparison of the stack models in MATLAB and Simulink 81

Figure 4.15 Comparison of BoP models in MATLAB and Simulink..... 81

Figure 4.16 Results of the MPPT model 84

Figure 4.17 Validation of the metal hydride model developed in Simulink against the experimental data of Tong et al. (2019), presenting a) time-dependent weight fraction (%) b) average temperature of the MH bed. 85

Figure 4.18 Daily performance of the PV-AEMWE during summer, showing a) PV power (W), b) H_2 mass flow rate (kg/h), c) electrolyzer efficiency (LHV%), and d) total H_2 production (kg). 86

Figure 4.19 a) Surplus electrical power profile and b) daily accumulation of unused electrical energy.. 87

Figure 4.20 Maximum metal hydride bed temperature profiles during summer for convection coefficients of a) $h_c = 10$, b) $h_c = 50$, c) $h_c = 500$, d) $h_c = 2000$ ($W/m^2 \cdot K$)..... 89

Figure 4.21 Mean temperatures of each metal hydride tank bed during summer for convection coefficients of a) $h_c = 10$, b) $h_c = 50$, c) $h_c = 500$, d) $h_c = 2000$ ($W/m^2 \cdot K$)..... 90

Figure 4.22 Gas densities of each metal hydride tank bed during summer for convection coefficients of a) $h_c = 10$, b) $h_c = 50$, c) $h_c = 500$, d) $h_c = 2000$ ($W/m^2 \cdot K$)..... 92

Figure 4.23 Mean temperature, H_2 gas density, and pressure changes over time in Tank 1 during summer for a) $h_c = 10$ $W/m^2 \cdot K$, b) $h_c = 500$ $W/m^2 \cdot K$ 93

Figure 4.24 Weight fraction values of each metal hydride tank bed during summer with convection coefficients varying from 5 to 2000 $W/m^2 \cdot K$..... 94

Figure 4.25 Daily performance of the PV-AEMWE during winter, showing a) PV power (W), b) H_2 mass flow rate (kg/h), c) electrolyzer efficiency (LHV%), and d) total H_2 production (kg). 96

Figure 4.26 Maximum metal hydride bed temperature profiles during winter for convection coefficients of a) h_c = 5, b) h_c = 10, c) h_c = 50, d) h_c = 500 (W/m^2·K)..... 98

Figure 4.27 Mean metal hydride bed temperature profiles during winter for convection coefficients of a) h_c = 5, b) h_c = 10, c) h_c = 50, d) h_c = 500 (W/m^2·K).... 99

Figure 4.28 Gas densities of each metal hydride tank bed during winter for convection coefficients of a) h_c = 5, b) h_c = 10, c) h_c = 50, d) h_c = 500 (W/m^2·K).. 100

Figure 4.29 Temperature, gas density, and pressure changes over time in Tank 1 during winter for a) h_c = 10 W/m^2·K and b) h_c = 500 W/m^2·K 101

Figure 4.30 Final weight fraction values of each metal hydride tank bed during winter with convection coefficients varying from 5 to 2000 W/m^2·K..... 102

Figure 4.31 Effect of the convective heat transfer coefficient on the peak heat extraction rate and total extracted heat under summer and winter conditions 105

LIST OF TABLES

Page

Table 2.1 Advantages and disadvantages of AWE-, PEMWE-, AEMWE, and SOEC-based electrolysis technologies 15

Table 2.2 Summary of studies involving electrolyzer-metal hydride storage systems 35

Table 3.1 Coefficients for specific heat calculations of each gas species..... 41

Table 3.2 Parameters for stack and electrolyte tank modeling 50

Table 3.3 Thermophysical and kinetic properties of $LaNi_5$-based MH 60

Table 4.1 HER and OER characteristics 62

Table 4.2 Parameters used in the modeling 64

Table 4.3 Electrochemical and physical properties of PBI-based membranes 68

Table 4.4 Values of the convection heat transfer coefficient depending on the process 82

Table 4.5 Hourly solar and ambient temperature data and corresponding resistance values in July..... 83

Table 4.6 Comparison of simulation results of MPPT-PV with manufacturer's data sheets 85

Table 4.7 Hourly solar and ambient temperature data and corresponding resistance values in January 95

Table 4.8 Effect of convective heat transfer coefficient on hydrogen waste and heat extraction during summer 103

Table 4.9 Effect of convective heat transfer coefficient on hydrogen waste and heat extraction during winter. 103

LIST OF SYMBOLS

V_{cell}	: Cell voltage (V)
V_{Rev}	: Thermodynamic/reversible voltage (V)
η_{act}	: Activation overpotential (V)
η_{ohm}	: Ohmic overpotential (V)
η_{KOH}	: KOH overpotential (V)
η_{Bub}	: Bubble related overpotential (V)
R	: Universal gas constant (J/mol·K)
n	: Number of electrons transferred per mole of the species of interest (–)
F	: Faraday's constant (C/mol)
c_p	: Specific heat (J/kg·K)
M	: Molarity (mol/L)
T	: Temperature (K)
i_0	: Exchange current density (A/m^2)
α	: Charge transfer coefficient (–)
b	: Tafel slope (mV dec^{-1})
P	: Pressure (Pa)
R_{ohm}	: Ohmic Resistance (Ωm^2)
i	: Current density (A/m^2)
σ	: Conductivity (S/cm)
η	: Efficiency (–)
I	: Current (A)
$\dot{m}$	: Mass flow rate (kg/s)
$\dot{W}$	: Electrical power (J/s)
$\dot{E}$	: Enthalpy flow rate (J/s)
$\dot{Q}$	: Heat transfer (J/s)
h_c	: Convective heat transfer coefficient (W/m^2·K)
A	: Area (m^2)
h	: Enthalpy (J/kg)
$\bar{M}$	: Molar mass (kg/mol)

n_f : Faradaic efficiency (–)

C : Overall thermal capacity (J/K)

V : Volume (m^3)

$\dot{n}$: Molar mass flow rate (mol/s)

ρ : Density (kg/m^3)

$\dot{m}'''$: Volumetric mass flow rate ($kg/m^3 \cdot s^1$)

C_a : Reaction constant of absorption (J/kg·K)

E_a : Activation energy of absorption (J/mol)

q_{gen} : Generated heat (W/m^3)

ε : Porosity (–)

Subscripts

ref : Reference conditions

ext : External

amb : Ambient conditions

cell : Electrolyzer cell

stack : Electrolyzer stack

ss : Fully saturated state

s : Pure metal state

eff : Effective

eq : Equilibrium

ABBREVIATIONS

AWE	: Alkaline Water Electrolyzers
PEMWE	: Proton Exchange Membrane Water Electrolyzers
SOEC	: Solid Oxide Electrolyzers
AEMWE	: Anion Exchange Membrane Water Electrolyzers
PBI	: Polybenzimidazole
BOP	: Balance of Plant
MH	: Metal Hydride
PV	: Photovoltaic Panel
AEM	: Anion Exchange Membrane
PEM	: Proton Exchange Membrane
CCUS	: Carbon Capture, Utilization and Storage
GW	: Gigawatt
DC	: Direct Current
HER	: Hydrogen Evolution Reaction
OER	: Oxygen Evolution Reaction
MW	: Megawatt
HHV	: Higher Heating Value
PM	: Precious Metal
O-SOEC	: Oxygen Ion-Conducting Solid Oxide Electrolysis Cells
H-SOEC/P-SOEC	: Proton-Conducting Solid Oxide Electrolysis Cells
TRL	: Technology Readiness Level
RWGS	: Reverse Water Gas Shift
YSZ	: Yttria-Stabilized Zirconia
CGO	: Gadolinium-Doped Ceria
PGM	: Platinum-Group Metal
PTL	: Porous Transport Layer
LCOH	: Levelized Cost of Hydrogen
IEC	: Ion Exchange Capacity
LHV	: Lower Heating Value
DI	: Deionized

WU	: Water Uptake
QA	: Quaternary Ammonium
IM	: Imidazolium
PIP	: Piperidinium
PSU	: Power Supply Unit
AC	: Alternating Current
PID	: Proportional-Integral-Derivative
PSA	: Pressure Swing Adsorption
PTX	: Power to X
EC	: Electrolyzer Cell
FC	: Fuel Cell
0D	: Zero-Dimensional
MPPT	: Maximum Power Point Tracking
MPP	: Maximum Power Point
FDM	: Finite Difference Method
STC	: Standard Test Conditions

CHAPTER ONE
INTRODUCTION

1.1 Introduction

The increasing global energy demand and the urgent need to reduce carbon emissions are driving the search for sustainable energy solutions. The fluctuating nature of many renewable energy sources highlights the importance of efficient and reliable energy storage systems. Hydrogen, in addition to its potential as a fuel source, has become a promising energy carrier thanks to its high gravimetric energy density, versatility, and long-term storage capabilities. Water electrolysis is an important method for producing green hydrogen without carbon emissions. Common technologies include alkaline water electrolyzers (AWE), proton exchange membrane water electrolyzers (PEMWE), solid oxide electrolyzers (SOEC), and anion exchange membrane water electrolyzers (AEMWE). AEMWE is gaining increasing attention because it maintains its efficiency under alkaline conditions despite using low-cost, non-precious metal catalysts. However, the overall performance of AEMWE cells is significantly affected by operating conditions, electrochemical processes, thermal, and mass transfer phenomena. In line with energy needs, it is crucial that these systems be suitable for large-scale applications. Ongoing advancements in AEMWE technology for large-scale applications highlight the need to develop membranes with improved stability and conductivity. In this context, polybenzimidazole (PBI)-based membranes are considered promising candidates due to their improved thermal and chemical stability and the good ionic conductivity they exhibit after successful synthesis. Accurately predicting the impact of membrane properties on cell performance requires modeling studies that can resolve the coupled electrochemical interactions within the cell.

In practice, AEMWE systems consist of auxiliary components, collectively referred to as balance of plant (BoP). These systems also include components that ensure the operation of electrolyzer stacks at desired temperatures. In particular, the heat exchange associated with the electrolyte flow between the electrolyzer and the electrolyte tank affects the stack temperature and the overall thermal balance of the system. Electrolyzers are often integrated with intermittent renewable energy sources

and hydrogen storage units. Among the storage methods, metal hydride (MH) tanks provide a safe and compact option. However, they require effective thermal management because of the exothermic and endothermic nature of hydrogen absorption and desorption reactions. Analyzing the thermal behavior of components within a system is essential for understanding their potentials and limitations and enhancing their efficiency.

1.2. Scope and Objectives

The scope of this study covers the modeling and analysis of an AEMWE operating under alkaline conditions. An electrochemical AEMWE cell model is developed to describe voltage-current behavior, where the overpotential terms are considered material-dependent, reflecting the electrochemical characteristics of the selected electrodes and membranes. The model is applied to investigate the performance of PBI-based membranes, which are chosen for their favourable thermal and chemical stability compared to conventional anion exchange membranes. Several PBI membranes are compared, considering their conductivity values at different temperatures, to assess their influence on cell performance. The response of the selected membranes to temperature variation is further examined in relation to membrane thickness and its impact on overall efficiency.

The subsequent part of the study examines the balance of plant (BoP) effects, particularly the heat exchange between the electrolyte tank and the electrolyzer, which governs the stack temperature and overall thermal response of the system. Finally, the developed AEMWE model is integrated into a photovoltaic-metal hydride (PV-AEMWE-MH) configuration to investigate the coupled production-storage behavior and the role of thermal management in determining storage capacity under variable solar and ambient temperature conditions.

Objectives of the thesis can be given as follows.

- To develop a model of the AEMWE cell that characterises the voltage-current relationship.
- To evaluate the baseline performance of several PBI-based membranes by comparing their voltage-current behavior under similar operating conditions.

- To investigate the effect of temperature on cell performance by incorporating the temperature-dependent conductivity values of selected PBI membranes, thereby assessing the relationship between thermal stability, conductivity, and overall efficiency.
- To examine the influence of membrane thickness on the voltage-current characteristics and efficiency of the cell.
- To investigate the thermal coupling between the electrolyte tank and the electrolyzer to determine its influence on stack temperature through sensitivity analysis.
- To integrate the developed AEMWE model with photovoltaic panels and metal hydride tanks (PV-AEMWE-MH) system to analyse the coupled hydrogen production-storage dynamics under fluctuating solar and ambient conditions.
- To assess the role of thermal management in storage performance and capacity of metal hydride (MH) tanks while considering safety limitations such as MH bed temperature and gas pressure.

1.3. Thesis Outline

Chapter 2 – Background and Literature Review provides a detailed overview of electrolysis technologies, including alkaline, proton exchange membrane (PEM), anion exchange membrane (AEM), and solid oxide water electrolyzers. The operational principles and performance characteristics of AEMWEs are reviewed, along with an evaluation of membrane materials and system-level configurations. The chapter concludes by summarising the role of the balance of plant (BoP) components and reviewing existing modeling approaches for electrolyzer and metal hydride (MH)-based systems.

Chapter 3 – Methodology describes the modeling framework developed in this study. It introduces the electrochemical equations used in the cell-level AEMWE model, detailing the calculation of thermodynamic cell voltage and overpotential losses. The system-level model is then presented, including the energy balance equations for the stack and the thermal coupling between the electrolyte tank and the electrolyzer. Finally, the modeling of metal hydride storage tanks and the Simulink-based system integration with renewable power sources are explained.

Chapter 4 – Results and Discussion presents and discusses the detailed outcomes of the AEMWE modeling and simulations conducted. The initial section focuses on the cell-level model validation and performance evaluation, where the model's outputs, particularly the overpotential values (activation, ohmic, etc.), are analyzed to determine their contribution to the cell's overall voltage-current behavior and efficiency. This is followed by a specific analysis of PBI-based membrane performance, detailing how changes in operating temperature and membrane thickness affect their cell voltage and efficiency. The second section examines the system-level dynamics, focusing on the thermal interactions between the electrolyte tank and the electrolyzer. Finally, it presents the system's dynamic behavior when configured in an integrated photovoltaic-metal hydride (PV-AEMWE-MH) setup under realistic, variable operating conditions, considering safety limitations.

The final chapter summarizes the key findings obtained from the developed modeling framework. It highlights how the model enhanced the understanding of operational effects on AEMWE performance and emphasizes the promising potential of PBI-based membranes for future system optimization. The chapter concludes with an evaluation of the system-level components, assessing the importance of effective thermal management between the electrolyte tank and the electrolyzer stack. Finally, it underlines how vital thermal control is for the safe and efficient operation of MH tanks used for hydrogen storage.

CHAPTER TWO
BACKGROUND AND LITERATURE REVIEW

2.1 Overview of Electrolysis Technologies

Hydrogen is produced through various processes that could utilise either renewable or non-renewable resources. It is often categorized by color according to its production method (Shiva Kumar & Lim, 2022), however no definitive standard has been established, and different colors can be seen from different sources found in the literature. Most hydrogen is still gray hydrogen, produced from fossil fuels, mostly without carbon capture, utilization and storage (CCUS) technologies. Global hydrogen production reached 100 metric tons in 2024, but only 1% of this was low-emission hydrogen, which includes hydrogen produced by water electrolysis and hydrogen derived from biomass or fossil fuels with CCUS technologies. This trend has been increasing steadily since 2020, with a 10% increase compared to production in 2023. Among these, the installed capacity of hydrogen production by water electrolysis reached 2 Giga-Watt (GW) by the end of 2024 (IEA, 2025). The main hydrogen production pathways are explained in greater detail in Figure 2.1.

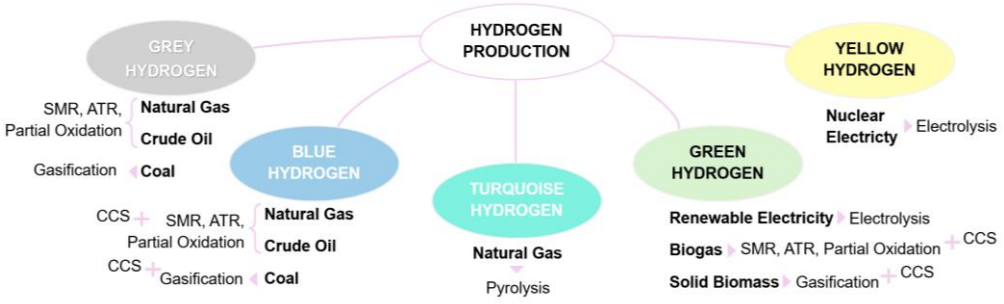

Figure 2.1 Classification of hydrogen production routes, adapted from Noussan et al. (2020).

Among the available pathways to produce hydrogen from renewable energy sources, water electrolysis is the most mature and advanced technology (J. Yang et al., 2025). Unlike fossil fuels, which are limited by countries' geopolitical flexibility, renewable resources are abundant in almost every region of the world and can be directly converted into hydrogen through electrolysis. This independence, combined

with hydrogen's versatility as both a fuel and an energy carrier, further highlights its strategic importance in future energy systems.

The term electrolysis originates from the Greek words “electro” (electricity) and “lysis” (to break apart), and thus literally means “breaking apart using electricity.” (J. P. Chen et al., 2005). Michael Faraday first proposed the scientific basis for electrolysis in the early 1800s, introducing terms such as electrode, electrolyte, anode, and others (Sandstede et al., 2010). Beyond hydrogen production, electrolysis has been widely utilized in areas such as wastewater treatment (J. P. Chen et al., 2005).

Electrolysis is a process that utilizes electricity to initiate the chemical reaction. Water electrolyzers are electrochemical devices that use direct current (DC) to break down water into hydrogen and oxygen, turning electrical energy into chemical energy (Khalid Ratib et al., 2024). At standard conditions, a voltage of at least 1.23 V is required to commence the process, corresponding to an energy input of $\Delta G^\circ = 237.1$ kJ/mol (Tijani et al., 2018). However, in practice, additional energy is needed to overcome kinetic barriers.

Water electrolysis consists of two half-reactions: the hydrogen evolution reaction (HER) at the cathode, where hydrogen gas is produced, and the oxygen evolution reaction (OER) at the anode, where oxidation occurs (Shih et al., 2022). A selectively conductive membrane or diaphragm is employed to separate the two electrodes and prevent gas crossover. (Abdel Haleem et al., 2023). The efficiency and performance of an electrolyzer depend strongly on its operating conditions (temperature, pressure, water flow rate) and the selection of electrode, electrolyte, and membrane materials (Choi et al., 2021; Kiessling et al., 2021; Y. Li et al., 2022; Majasan et al., 2018).

Electrolyzer technologies are commonly classified based on their operating temperature and the type of conducting ion (proton-, hydroxide-, or oxide-conducting). Low-temperature electrolyzers, such as alkaline water electrolyzers (AWEs), proton exchange membrane water electrolyzers (PEMWEs), and anion exchange membrane water electrolyzers (AEMWEs), typically operate below 100 °C. In contrast, SOECs operate at high temperatures (600-850 °C), taking advantage of favorable thermodynamics at elevated conditions (Ayers & Marina, 2024). Each technology has

its own advantages and limitations, making their suitability dependent on the intended application. In earlier decades, electrolyzers were often coupled with stable and low-cost steady power sources, while recent studies increasingly explore integration with intermittent renewable sources such as wind (Cooper et al., 2022). Besides that, the scalability of the systems is crucial to meeting the worldwide goals of net-zero carbon emissions. Electrolyzer systems must scale up from the current megawatt (MW) capacity to a widespread gigawatt (GW) scale for industrial hydrogen production (Riaz et al., 2025).

2.1.1 Alkaline Water Electrolyzer (AWE)

AWE electrolysis systems contain an electrolyte solution between two electrodes and a selectively permeable diaphragm. This diaphragm allows hydroxide anions to pass through the electrolyte while preventing the produced hydrogen and oxygen from mixing, as shown in Figure 2.2.

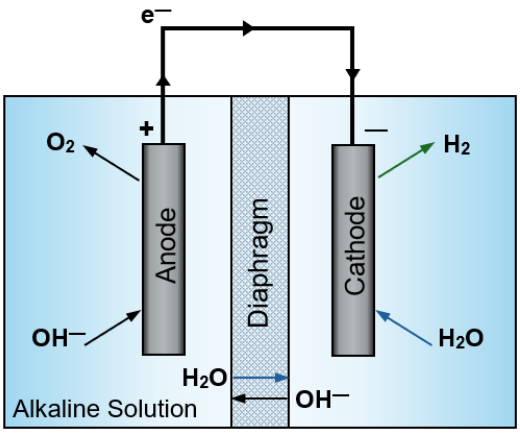

Figure 2.2 Schematic representation of an alkaline water electrolyzer

With an external current applied to the electrolyzer, water molecules undergo a reduction reaction at the cathode to produce hydrogen, while hydroxide ions undergo an oxidation reaction at the anode to produce oxygen. These electrochemical half-reactions are presented in Eqs. (2.1-2.3), together with the overall cell reaction (M. Zhang et al., 2024).

Anode:

$$2OH^- \rightarrow \frac{1}{2}O_2 + H_2O + 2e^- \quad (2.1)$$

Cathode:

$$2H_2O + 2e^- \rightarrow H_2 + 2OH^- \quad (2.2)$$

Overall Reaction:

$$H_2O \rightarrow H_2 + \frac{1}{2}O_2 \quad (2.3)$$

AWE is the most mature electrolysis technology, with large-scale applications dating back to the early 20th century. Typical operating conditions include temperatures between 70-100 °C, current densities of 0.2-2 A/cm², and pressures ranging from 1 to 40 bar (Ehlers et al., 2023). They are generally characterized by the circulation of a 20-30 wt.% (4.2-6.9 M) aqueous KOH solution (Henkensmeier et al., 2024; Ikhsan et al., 2025). Reported higher heating value (HHV) efficiencies are between 65-80%, corresponding to a specific energy consumption of 4.5–5.5 kWh/Nm³ H_2 (Rabillard et al., 2025). With a stated lifetime exceeding 30 years, AWEs offer one of the most durable and established solutions among water electrolysis technologies (Ren et al., 2022). Its performance is also influenced by the diaphragm's properties (e.g., porosity and thickness) (Muhsen et al., 2024; Niblett et al., 2024) and the distance between electrodes and adjacent components (Ouabi et al., 2024; Rodríguez & Amores, 2020). The energy efficiency of AWEs could be improved by up to 80% by optimizing voltage losses associated with the ionic resistance of the electrolyte between the electrode and the diaphragm (Mei et al., 2024; Ouabi et al., 2024). The alkaline-media operation also mitigates cost limitations by enabling the use of earth-abundant elements (i.e., nickel or cobalt) for water electrolysis (Ďurovič et al., 2021; Galkina et al., 2024; Thangavel et al., 2023; Y. Zheng et al., 2023).

Recent developments, such as zero-gap cell designs, aim to reduce ohmic losses by pressing the diaphragm directly against the electrodes, thereby increasing efficiency. Nevertheless, AWE continues to face performance and flexibility limitations when integrated with intermittent renewable energy sources (Ehlers et al., 2023).

2.1.2 Proton Exchange Membrane Water Electrolyzer (PEMWE)

A Proton Exchange Membrane (PEM) electrolyzer uses electricity to split water into hydrogen and oxygen. Water is oxidized at the anode to produce oxygen, while protons move through the membrane and electrons travel through an external circuit to form hydrogen at the cathode. This process is illustrated in Figure 2.3.

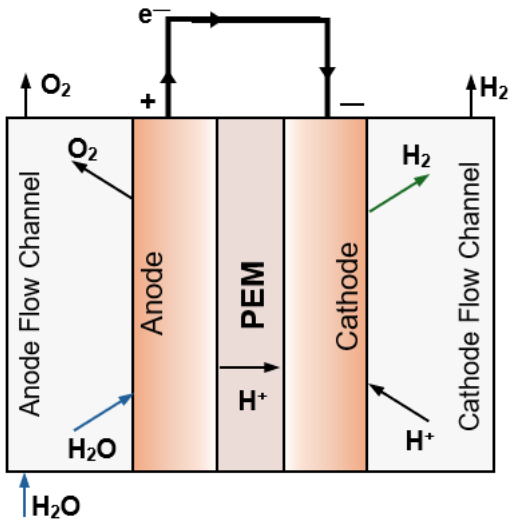

Figure 2.3 Schematic representation of a proton exchange water electrolyzer

Eqs. 2.4 and 2.5 show the reactions that occur at the anode and cathode, respectively, while Eq. 2.6 represents the overall reaction of the electrolysis process for PEMWE.

Anode:

$$H_2O \rightarrow 2H^+ + \frac{1}{2}O_2 + 2e^- \tag{2.4}$$

Cathode:

$$2H^+ + 2e^- \rightarrow H_2 \tag{2.5}$$

Overall Reaction:

$$H_2O \rightarrow H_2 + \frac{1}{2}O_2 \tag{2.6}$$

The zero-gap electrolyzers equipped with proton exchange membranes (PEMs), owing to the minimized voltage losses and promoted H^+ transport, enable energy efficiencies of 70-80% (Carmo et al., 2013; Sebbahi et al., 2024) at industrially relevant current densities of 1-1.5 A cm^{-2} (J. Chen, Wang, et al., 2025; Lamy, 2016). PEMWEs require no pressure equilibrium between the electrodes (Abdel Haleem et al., 2023), allowing hydrogen production at pressures even up to 700 bar (Bin et al., 2024; Dang et al., 2023). This capability is particularly advantageous for integrating hydrogen generation with storage systems, as it eliminates or reduces the need for additional compression, thereby lowering the overall energy consumption of the system (Huang et al., 2024). However, the acidic environment necessary for proton conduction demands materials with high corrosion resistance. As a result, noble metal catalysts such as platinum, iridium, and ruthenium are typically employed at the electrodes (Hammi et al., 2023; Makhsoos et al., 2023; Xie et al., 2024), which significantly increases system cost and limits large-scale deployment (Tamilarasi et al., 2024).

2.1.3 Anion Exchange Membrane Water Electrolyzer (AEMWE)

Anion exchange membrane water electrolyzers (AEMWEs) enable hydrogen production under alkaline conditions by conducting hydroxide ions (OH^-) through an anion exchange membrane, as shown in Figure 2.4.

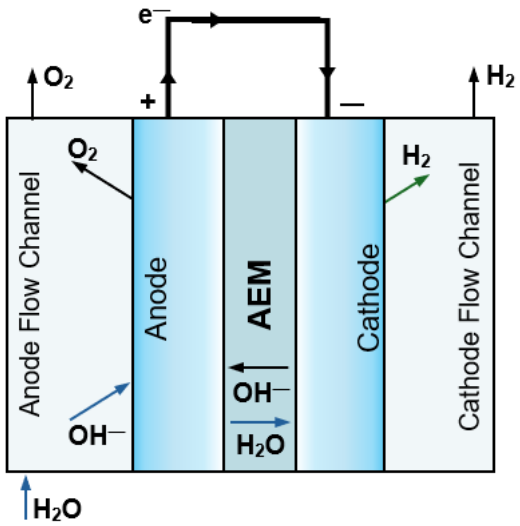

Figure 2.4 Schematic representation of an anion exchange membrane water electrolyzer

In this configuration, water oxidation occurs at the anode, producing oxygen, electrons, and hydroxide ions, while at the cathode, water molecules are reduced to form hydrogen gas. The hydroxide ions generated at the cathode migrate through the membrane toward the anode, maintaining charge balance. The electrochemical reactions occurring at the anode and cathode, as well as the overall cell reaction, are expressed by Eqs. (2.7-2.9), respectively (Ďurovič et al., 2021; J. Li, 2022).

Anode:

$$2OH^- \rightarrow \frac{1}{2}O_2 + H_2O + 2e^- \quad (2.7)$$

Cathode:

$$2H_2O + 2e^- \rightarrow H_2 + 2OH^- \quad (2.8)$$

Overall Reaction:

$$H_2O \rightarrow H_2 + \frac{1}{2}O_2 \quad (2.9)$$

In AEMWE, similar to PEMWE, Pt-based (HER) and Ru/Ir-based (OER) are often used for cathode and anode electrodes, respectively, due to their very high performance despite their scarcity and high price (Sankar et al., 2023; Y. Xu et al., 2022). However, significant progress has been made in non-noble catalysts and ion-conducting membranes under alkaline conditions. Ni-Fe oxyhydroxides may demonstrate superior catalytic performance in alkaline conditions, despite their limited durability in electrolyzer systems (Krivina et al., 2022). Recent advancements in non-precious metal catalysts indicate improved performance and durability (Krivina et al., 2022). For OER, precious metal (PM)-free oxide-based electrocatalysts show promising performance for AEM applications due to their cost-effectiveness, abundance, and tunable electronic structure, which reduces the kinetic and thermodynamic barriers in oxygen electrocatalysis under alkaline conditions (J. Tang et al., 2021).

2.1.4 Solid Oxide Water Electrolyzer (SOEC)

Solid oxide electrolyzer cells (SOECs) consist of an oxide-ion conductive electrolyte and two porous electrodes. As a result of favorable thermodynamics and

reaction kinetics, SOECs can show up to 100% energy efficiency, with operating temperatures typically between 600°C and 900°C (Wolf et al., 2023). The process in SOECs is based on the principles of electrochemical reactions and ion transfer, achieved through the migration of ion species between two electrodes with catalytic active sites in an electrolyte. SOECs require mechanical support for stability under these high-temperature operating conditions (Gallandat et al., 2017).

Solid oxide electrolysis cells (SOECs) can be divided into two types, depending on the type of ions transported in the electrolyte: oxygen ion-conducting solid oxide electrolysis cells (O-SOEC) and proton-conducting solid oxide electrolysis cells (H-SOEC or P-SOEC). In brief, O-SOECs transport oxygen ions, while H-SOECs transport protons. The basic operating principle of H-SOEC allows the production of pure hydrogen without an extra step for gas separation (L. Lei et al., 2019). It has a lower activation energy for proton diffusion, which allows lower operating temperatures than O-SOEC, making them preferable for low-temperature SOECs due to their higher ionic conductivity and electrical efficiency. However, the technology readiness level (TRL) of H-SOEC is currently lower than that of conventional O-SOEC, and no commercial systems have been demonstrated yet. The remaining challenges with H-SOEC arise from the structures and materials used in different stack/cell designs (X. Zhang et al., 2023). The general working principles of H-SOEC and O-SOEC are shown in Figure 2.5, respectively.

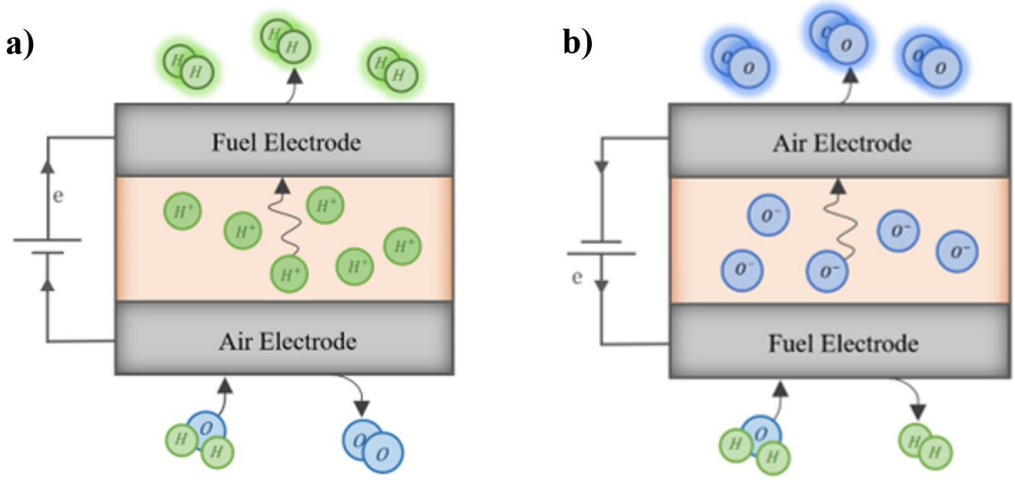

Figure 2.5 a) Proton-conducting solid oxide electrolysis cells (H-SOEC) b) oxygen ion-conducting solid oxide electrolysis cells (O-SOEC)

In an oxygen ion-conducting solid oxide electrolysis cell (O-SOEC), the cathode is exposed to a gas stream comprising H_2O, CO_2, or a combination of both. This gas stream is then reduced to produce H_2, CO, or syngas fuel, as shown in Eqs. 2.10 and 2.11, respectively. Simultaneously, oxygen ions produced at the cathode side migrate through the dense electrolyte toward the anode, driven by an external voltage. Subsequently, the oxygen ions are oxidized to form oxygen molecules in the anode, releasing electrons, as in Eq. 2.12 (Y. Xu et al., 2023; X. Zhang et al., 2017).

Cathode:

$$H_2O + 2e^- \rightarrow H_2 + O^{2-} \quad (2.10)$$

$$CO_2 + 2e^- \rightarrow CO + O^{2-} \quad (2.11)$$

Anode:

$$2O^{2-} \rightarrow O_2 + 4e^- \quad (2.12)$$

For the co-electrolysis of H_2O and CO_2 in the H-SOEC process, steam (H_2O) is electrochemically decomposed at the anode and dissociates into oxygen, protons, and electrons, as shown in Eq. 2.13. When protons diffuse through the electrolyte to the cathode, hydrogen is produced by the combination of protons and electrons at the interface (Eq. 2.14). At the same time, CO_2 fed from the cathode reacts with hydrogen through the reverse water gas shift (RWGS) reaction as in Eq. 2.15, thus producing CO and H_2O on the cathode side. This is an indication of synthesis gas production on the cathode side and the presence of excess steam on the anode side (Patcharavorachot et al., 2023; X. Zhang et al., 2017).

Anode:

$$H_2O \rightarrow 2H^+ + \frac{1}{2}O_2 + 2e^- \quad (2.13)$$

Cathode:

$$2H^+ + 2e^- \rightarrow H_2 \quad (2.14)$$

$$CO_2 + H_2 \rightarrow CO + H_2O \quad (2.15)$$

Solid oxide electrolyzer consists of three main components: an anode electrode where the fuel is oxidized, a cathode electrode or reduction electrode where the oxidized fuel is reduced, and the electrolyte layer between these two ensures ion transfer from the anode to the cathode. In the context of Solid Oxide Electrolysis Cells (SOECs), the electrodes and electrolytes play pivotal roles in influencing overall performance. The Fuel electrode is where steam is electrochemically reduced into hydrogen, requiring a porous electronic-ionic conductor. Ni-YSZ (ceramic-metal composite) is the leading material, combining YSZ electrolyte and nickel for better efficiency. The air electrode oxidizes O^{2-} ions to oxygen, demanding high mixed ionic-electronic conductivity. Perovskite-based materials, such as (La, Sr) (Co, Fe)O_3 and $La_{0.8}Sr_{0.2}MnO_{3-\delta}$, excel in electrocatalytic performance. Meanwhile, the electrolyte, typically 8YSZ or Gadolinium-doped ceria (CGO), ensures high ionic conductivity, stability, and durability in the SOEC environment (Nechache & Hody, 2021).

2.1.5 Comparison of Water Electrolyzer Technologies

Each technology has its own advantages and disadvantages, which are compared in Table 2.1. It should be emphasized that the performance of each system depends on the specific application and operational requirements; therefore, no single technology can be considered universally optimal. A system that excels in one aspect may be disadvantaged in another, highlighting the need to support the advancement of all electrolysis technologies to address diverse operational needs.

Table 2.1 Advantages and disadvantages of AWE-, PEMWE-, AEMWE, and SOEC-based electrolysis technologies (Acevedo et al., 2023; Bazarah et al., 2022; Bin et al., 2024; Büsch et al., 2024; Y. Du et al., 2024; Hong et al., 2026; Hou et al., 2025; Huang et al., 2024; International Renewable Energy Agency (IRENA), 2020; James et al., 2024; Jolaoso et al., 2023; Kim et al., 2024; Q. Liu et al., 2025; Meharban et al., 2024; Mulk et al., 2024; Nicholas et al., 2025; Noor Azam et al., 2023; Rizwan et al., 2021; Salehmin et al., 2022; Z. Tang et al., 2025; C. R. Wang et al., 2025; Wei et al., 2024; Y. Xu et al., 2024).

Electrolysis Technology	Advantages	Disadvantages
SOEC	• High efficiency • Reversible operation • Utilization of thermal energy • Affordable materials	• High operation costs due to elevated temperatures (600-850 °C). • Complex thermal management • High manufacturing costs • Material degradation • Limited long-term reliability
AEMWE	• Cutting-edge and promising technology • Lower cost while maintaining high efficiency • Use of transition metals instead of (platinum-group metal) PGMs • Capable of moderate pressure operation (up to ~ 30 bar) • Ability to operate at differential pressure • Operates with pure water or low-molarity electrolyte (0.1-1 M) • Fast response under dynamic conditions • Compact design	• Low durability • Poor long-term stability • Limited long-term demonstration at an industrial scale
PEMWE	• Operates at high current densities (1-4 A/cm^2) • Enables high-pressure hydrogen production (up to 70 bar) • Ability to operate at differential pressure • Compact design • High gas purity (>99.999%) • Fast response under dynamic conditions	• Corrosive acidic environment • Dependence on PGM catalysts • High capital cost, primarily due to expensive catalysts • Sensitive to water purity

Table 2.1 (Continued)

Electrolysis Technology	Advantages	Disadvantages
Traditional AWE	• Most mature and commercialized technology • Proven large-scale deployment • Long operational lifetime • Lower initial capital costs • Use of affordable catalysts (e.g., Ni, Fe)	• Limited to low-pressure operation due to safety risks; capable of high-pressure operation when equal pressure is maintained on both sides. • Lowest current densities • Higher risk of gas crossover • Poor dynamic response, posing greater difficulty for integration with intermittent renewables • Requires high-molarity KOH and additional components for electrolyte management • Bulkier design

The feasibility of electrolyzer systems is often evaluated based on cost, scalability, durability, and hydrogen production efficiency (Nzaba Madila et al., 2025). For industrial applications, scalability is a critical parameter, as systems are expected to operate at MW-scale power levels (Rizwan et al., 2021). Currently, AWEs are the most established at the multi-MW scale, PEMWEs are increasingly deployed in this range, and AEMWEs and SOECs remain at smaller pilot and early commercial scales (Büsch et al., 2024).

Cost competitiveness plays a decisive role in large-scale adoption, and as electricity supply is the main operating cost in electrolysis (Aslam et al., 2023), improving electrolyzer performance to maximize hydrogen output per unit of electricity is essential for reducing costs. A cost analysis study conducted by the Fraunhofer Institute for Solar Energy Systems ISE (Marius Holst et al., 2021) considered fixed costs such as investment and maintenance of the installed system, as well as electricity costs and annual full-load hours. For 5 MW plants, the study reports 2030 targets of around €726/kW for AWEs and €729/kW for PEMWEs, while for large-scale 100 MW plants, decreasing to €444/kW and €502/kW, respectively. According to The European Hydrogen Market Landscape, 2024, the stack, BoP, and total CAPEX costs of AWE in 2023 were approximately 408, 686, and 1666 €/kW, respectively. In comparison,

PEMWE exhibited higher costs, except for the BoP, with 732, 464, and 1970 €/kW for the stack, BoP, and total system, respectively. Furthermore, according to International Renewable Energy Agency (IRENA), 2020 analysis, Capital costs for large-scale (>1 MW, stack-only) systems are around 270 $/kW for AWE, 400 $/kW for PEM, and >2000 $/kW for SOEC. At the system level (>10 MW), total costs range between 500-1000 USD/kW for AWE, 700-1400 USD/kW for PEM. By 2050, stack costs are expected to fall below 100 $/kW for AWE, PEM, and AEM, and around 200 $/kW for SOEC; corresponding system costs are projected below 200 $/kW for low-temperature technologies and 300 $/kW for SOEC.

On the other hand, the Ionomr Innovations Report (2020), provides their insights, estimating 5 MW system costs at $587/kW for PEMWEs, $596/kW for AWEs, and $554/kW for pressurized AWEs. AEMWEs show lower costs, about $444/kW and $459/kW (without and with PGM). Cost advantages for AEMWEs arise from reduced BoP requirements, due to the absence of additional pressurization, unlike traditional AWEs, as well as the avoidance or significant reduction of PGM use compared to PEMWEs. Similar trends are reported by Kim et al. (2024), showing that compared to PEMWEs, replacing PGMs with non-noble catalysts (~36% catalyst cost reduction) and using stainless-steel bipolar plates instead of titanium (~26% stack cost reduction) can significantly lower costs. Despite the study's estimate of higher PTL prices for AEMWEs compared to PEMWEs, the overall direct capital cost is reduced by about 12%. The study highlights that if stack lifetimes could be extended to PEMWE levels, the levelized cost of hydrogen (LCOH) would drop by roughly 21%, underscoring lifetime as a key factor for cost competitiveness and directly linking durability to economic viability.

Durability is a critical parameter that directly influences scalability and overall system cost, as limited lifetimes lead to more frequent replacements and higher long-term expenditures. Design measures such as thinner membranes or more active catalysts can enhance efficiency, but often at the expense of lifespan and higher initial cost (Meharban et al., 2024). This highlights the need for a holistic approach that balances efficiency, cost, and durability. In the case of PEMWEs, one of the main disadvantages for large-scale deployment is their reliance on costly titanium- and

platinum-based components, as high PGM loadings are still required to achieve durability targets, significantly increasing capital costs (Feng et al., 2017; C. R. Wang et al., 2025). To be viable for industrial use, electrolyzers are expected to reach operational lifetimes of up to 100,000 hours (Meharban et al., 2024). AWEs are the most established technology in this regard, with commercial systems typically exceeding 60,000 - 90,000 hours of operation (Bernäcker et al., 2019; Emonts et al., 2022; He et al., 2025; International Renewable Energy Agency (IRENA), 2020). PEMWEs have demonstrated more than 50,000 operating hours in certain cases, with recent reports indicating that up to 90,000 hours have been achieved with only a minor efficiency penalty (Endrődi et al., 2025; International Renewable Energy Agency (IRENA), 2020; Salehmin et al., 2022). SOECs, which operate at elevated temperatures, exhibit lifetimes that are highly dependent on stack design and heat management, as thermal gradients strongly influence degradation rates. In the literature, smaller-scale SOEC systems have demonstrated operational lifetimes ranging from 10,000 h to 20,000 h with minimal degradation, whereas larger stacks report shorter durability, often limited to a few thousand hours under continuous operation (Beyrami et al., 2025). The GrInHy2.0 project, which integrates SOEC technology with waste heat from the steelmaking process, has successfully achieved 13,000 h of efficient system operation, with stack-level targets approaching approximately 20,000 h (*Green Industrial Hydrogen via Steam Electrolysis*, 2019). On the other hand, AEMWEs generally operate for more than 5,000 hours (Henkensmeier et al., 2024; International Renewable Energy Agency (IRENA), 2020), with recent advancements extending lifetimes to around 10,000 hours (S. Han et al., 2024; D. Li et al., 2021; Volk et al., 2024). These improvements represent significant progress toward the 100,000-hour endurance target for AEMWEs; however, for them to be adopted in large-scale commercial systems, the performance and durability capabilities of PEMWE and AWE systems must be achieved (D. Li et al., 2021). Nevertheless, further improvements in performance while reducing costs are vital for the widespread adoption of all electrolysis technologies.

2.2 Anion Exchange Membrane Electrolyzer (AEMWE)

AEMWEs combine the advantages of both alkaline and proton exchange membrane systems, operating under alkaline conditions while maintaining a compact design, high current densities, and lower overall cost through the use of non-precious metal catalysts. The following subsections outline the principles of AEMWEs, their performance characteristics, material considerations, and criteria for membrane selection.

2.2.1 Principles of AEMWE

A comprehensive understanding of the transport mechanisms within the electrolyzer is essential not only for high-rate and energy-efficient hydrogen production (J. Li et al., 2023) but also for prolonging operational stability and inhibiting safety concerns (J. Lei et al., 2024; Rossi et al., 2023; Zelovich et al., 2019). Mass transport mechanisms in an AEM are governed by the identity of the species, transport mechanisms, and driving forces. The hydroxide transport is one of the most important factors affecting the membrane performance. The hydroxide ions are produced at the cathode under negative potential, crossing over to the anode through the AEM. The transport of hydroxide ions is facilitated by a combination of mechanisms: migration and diffusion mechanisms. The migration is driven by the electric field. The diffusion is governed by concentration gradients: the Grotthuss transport mechanism – also referred to as the proton hopping and surface-site hopping, each driven by distinct forces (Cavaliere, 2023). Figure 2.6 schematically illustrates the primary transport mechanisms of hydroxide ions in AEMs.

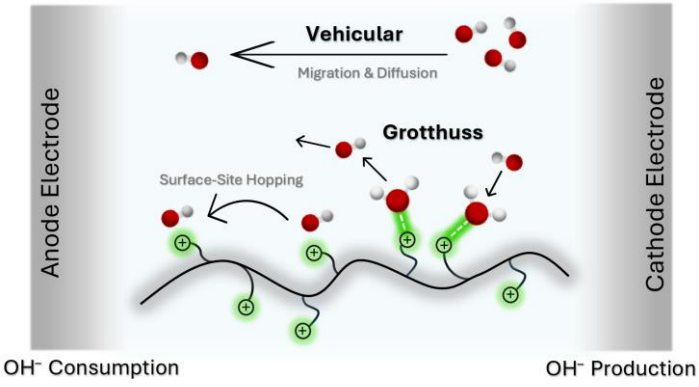

Figure 2.6 Schematic illustration of the primary hydroxide transport mechanisms in AEMs adapted from Ma & Wang (2024).

The transport mechanisms of hydroxide ions can be examined under the main category of diffusion. The diffusion-governed transport can also be classified into two different transport mechanisms: Grotthuss and vehicular (Dubey et al., 2020; Dubey & Daschakraborty, 2022; Hellström et al., 2019; C. Hu et al., 2024; Ma & Wang, 2024), as structural diffusion and translational transport, respectively (Dong, Zhang, et al., 2018). The hydroxide transport by diffusion captures the coupled effect of hydrodynamic and structural processes (M. Chen et al., 2018). Alternatively, they can be examined as different mechanisms, such as Grotthuss, migration and diffusion, surface transport, convection, and vehicular (Cavaliere, 2023; Karibayev et al., 2022). The migration process involves the transport of hydroxide ions from the cathode to the anode driven by an electric potential gradient (Vincent et al., 2018). Poor membrane conductivity is often correlated with a low ion migration rate (L. Liu et al., 2024). The ionic conductivity represents the combined influence of all active mechanisms and is an indicator of the membrane's ability to facilitate ion transport. The diffusion capacity exerts a significant impact on the migration rate of ions across a membrane. For instance, a lower diffusion capacity of hydroxide ions in comparison to H^+ ions would cause efficiency discrepancies between AEM- and PEM-based systems (Firouz Tadavani et al., 2023). The migration of hydroxide ions depends on the ionic vibrations and the changes in the strength of hydrogen bonds between hydroxide ions and water molecules. The hydroxide ions typically exhibit a higher degree of mobility at higher temperatures, due to the increasing kinetic energy of a molecule (C. Wang et al., 2018). Dubey & Daschakraborty (2022), investigated the effect of membrane hydration and temperature on vehicular motion. Results show that reduced hydration lowers the diffusion of water and hydroxide ions, while higher temperatures enhance this process. Results further demonstrate that the diffusion of water and hydroxide ions is more sensitive to hydration than temperature. Taken together, the dominant mechanism for H_2O and hydroxide transport, at high temperature and hydration, is the vehicular motion, while at low temperature and hydration, it is the Grotthuss mechanism.

Albeit the ongoing debate on the dominancy of diffusion-governing mechanisms (C. Chen et al., 2016; Dubey & Daschakraborty, 2022), the prevailing view is that the Grotthuss mechanism is more effective (Cavaliere, 2023; Dubey et al., 2020). According to the Grotthuss mechanism, the hydroxide ions transport through a

network of hydrogen bonds formed by the continuous formation and dissociation of water molecules (Cavaliere, 2023; Z. Yu et al., 2023). This mechanism is characterized by a structural process (M. Chen et al., 2018), where hydroxide ions diffuse by accepting a proton from neighboring water molecules (Jensen et al., 2005). While the vehicular diffusion of hydroxide ions, considering the viscosity of the medium, exhibits hydrodynamic behavior (Dubey et al., 2020), the Grotthuss mechanism remains the primary transport mechanism, surpassing the influence of hydrodynamic motion (M. Chen et al., 2018). Additionally, the predominance of these two mechanisms varies depending on the availability of water channels. The limited contribution of the vehicular to the total hydroxide diffusivity (<3%) renders the Grotthuss mechanism dominant hydroxide transport process through water channels (Dong, Zhang, et al., 2018). Nevertheless, a network of water channels in the membrane structure is also crucial for efficient hydroxide transport via the vehicle mechanism (C. Hu et al., 2024). Sun et al. (2022), formed effective ion channels as an alternative to swelling-induced ion exchange capacity (IEC) enhancement to achieve effective hydroxide transport. Highly ordered ion transport channels were created via attractive forces between porphyrins and the polarity difference between hydrophilic and hydrophobic segments. This enabled the development of AEMs with a high conductivity at a relatively low IEC. As a result, the AEM combined impressive characteristics, including an IEC of 0.35 $meq \cdot g^{-1}$, an ionic conductivity of 152.5 mS cm^{-1} OH^-, a swelling ratio of 14.6%, and a water uptake ratio of 53.3% at 80 °C. Additionally, the AEM demonstrated notable chemical stability of 1000 hours at 80 °C.

J. Han et al. (2017), investigated the correlation between hydration, conductivity, and ion transport, revealing how these variables change in response to alterations in IEC. An increasing diffusivity was observed with rising hydration; however, the AEMs showed varying responses to these changes, with some exhibiting impressive conductivities, while others showing only modest improvements. This phenomenon was attributed to the chemical structure of the AEMs under study. These findings revealed that, for a given membrane type, the enhanced diffusivity originates from superior hydroxide conductivity. In AEMs, hydroxide mobility is also negatively impacted by the narrow cross-sectional diameters in the membrane structure,

constraining the diffusion of fully hydrated hydroxide ions (Dong, Wei, et al., 2018; K. Zhang et al., 2018). Transport across these narrow pathways solely via the carrier mechanism requires hydroxide ions to be partially dehydrated, which is thermodynamically uphill. On the other hand, the Grotthuss is an efficient mechanism for hydroxide transport that would proceed without any significant loss of hydration structure (Dong, Zhang, et al., 2018).

The presence of cation domains is essential for facilitated ion transport. These domains attract water molecules and create interconnected channels for OH^- migration, enhancing the ionic conductivity of the AEM (Q. Zhang et al., 2024). Water content plays a critical role in hydroxide transport. Unlike other ions, hydroxide ions (along with H^+) demonstrate high mobility and improved transport dynamics in aqueous environments (Tuckerman et al., 2002). An increase in water uptake can enhance ionic conductivity. The water uptake is closely linked to and correlates with a higher IEC (Khalid et al., 2022; Msomi et al., 2020; Salma et al., 2020; Varcoe et al., 2014). However, excessive water uptake could have a detrimental impact on the mechanical strength of AEMs. Additionally, excess water could widen the ion channel opening, suppressing the hydrogen bond jumping and surface transport mechanisms (C. Wang et al., 2024). In the context of cation areas, R. Yang et al. (2023) found that the long-side chains containing multiple ionic groups are effective in augmenting the local concentration of cationic groups. The increased cation availability, in turn, improves ion mobility across ion-carrying channels. Additionally, it is noted that in the low IEC region, the hydrogen bond network plays a pivotal role in ion transport, with the hydrated ion channels becoming increasingly effective as ionic content rises.

Surface-site hopping is another transport mechanism, whereby hydroxide ions transport by jumping from one quaternary ammonium (QA) head group to another (Karibayev et al., 2022). The efficiency of this mechanism is governed by the electrostatic interaction between hydroxide ions, QA groups, and polymer structure (W. Zheng et al., 2024). Unlike other transport mechanisms, surface-site hopping becomes dominant at low hydration levels (Karibayev et al., 2022). The double cross-linking method, which is implemented to improve membrane morphology and conductivity, enables favorable results in this regard, even at a relatively low water

content. The method achieves this advance by simultaneously enhancing the Grotthuss mechanism and the surface site hopping process (C. Wang et al., 2024).

The effective hydroxide transport is closely linked to water transport dynamics within the membrane structure, as water content directly impacts ion mobility and diffusion pathways (Z. Yu et al., 2023). Furthermore, for applications like dry cathodes, evaluating water dynamics and managing hydration and ion exchange properties is key to avoiding excessive swelling at the water-fed anode and dehydration at the cathode (H. Park & Kohl, 2023). In these scenarios, the water supplied to the anode diffuses through the AEM to the cathode electrode, where the HER occurs. The motivation here is to avoid hydrogen contamination and produce relatively dry hydrogen, reducing operational costs by streamlining the hydrogen drying process (Ito et al., 2023; Koch et al., 2022; R. Wang et al., 2022). In these applications, water crosses over to the cathode by diffusion. However, the continuous water consumption at the cathode (triggered by the HER and water migration) could cause an imbalance in water availability and membrane dehydration (Hyun & Kim, 2020). Increasing the IEC in the cathode catalyst binder avoids dehydration by increasing the water content (Koch et al., 2022).

The water transport in AEMs occurs via various mechanisms, such as electro-osmotic drag, convection, and diffusion (León et al., 2022; Lv et al., 2023; B. Zhang et al., 2022). Figure 2.7 schematically illustrates the water transport mechanisms in AEMs.

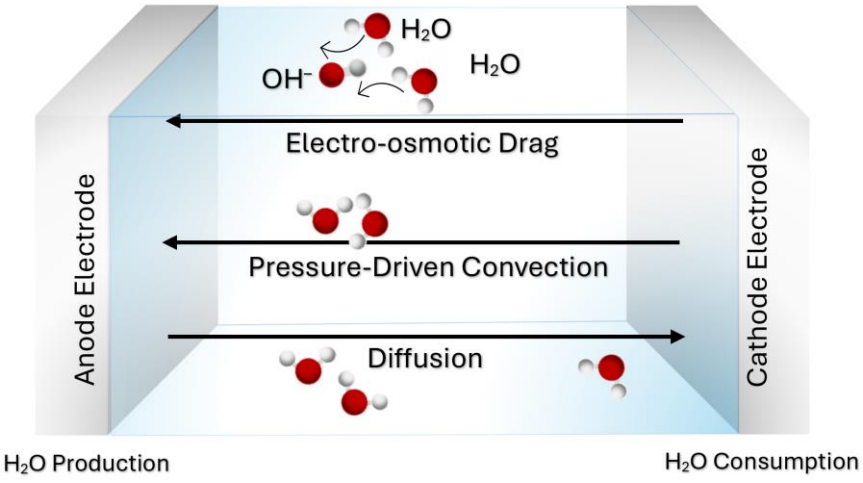

Figure 2.7 Water transport mechanisms in AEMWEs.

The electro-osmotic drag occurs through the transport of hydroxide ions across the AEM under the influence of an electric field (J. Li et al., 2023). The electro-osmotic drag coefficient (n_d) quantifies the number of water molecules carried alongside hydroxide ions, as they move through the AEM under the effect of an electric field (Gomez Vidales et al., 2023). This coefficient controls the amount of water carried with ions (D. Lee et al., 2024; Moradi Nafchi et al., 2024). It is thus closely correlated with membrane hydration. Y. S. Li et al. (2010) investigated water transport in a commercial AEM, with particular focus on diffusivity and electro-osmotic drag. Results show that the electro-osmotic drag coefficient increases with water uptake and temperature. The deviation of the findings from the literature was explained by the differences in experimental methodology. Additionally, it was noted that the methodological differences in ex- and in-situ measurements would be the source of discrepancy between the observed trends, consistent with the prior reports on the role of confined environments within water channels of AEMs (Dong, Zhang, et al., 2018).

Besides the diffusion and electro-osmotic transport, convection-driven transport also occurs due to pressure differentials (Qi et al., 2021). In AEMWEs, the anode is typically maintained at atmospheric pressure, while the cathode is typically pressurized (Ostwald, 1890), facilitating water transport from the high-pressure cathode to the low-pressure anode. In addition to the passage of water, cathode pressurization may also cause cross-permeation of hydrogen through the AEM (Fahr et al., 2024). While differential pressure has a negligible impact on cell performance, it can affect gas and water permeability under certain conditions (D. Li et al., 2021). Particularly, at high-pressure differentials, the pressure gradient – by tuning the permeability coefficient – would affect water transport (Fahr et al., 2024). Thinner membranes are more prone to hydrogen migration and mechanical failures under differential pressure, while thicker membranes offer greater mechanical robustness and lower gas permeability, making them less sensitive to pressure variations (Kang et al., 2021). Transport mechanisms should be optimized by establishing a good balance between ionic conductivity and stability. The AEM's structure and morphology play a significant role in achieving this, as these characteristics directly influence water management and hydroxide transport. While increased water uptake enhances ionic conductivity, it must be well-optimized to achieve simultaneous

performance and stability improvements. Understanding the transport behavior of water and permeating gases (i.e., H_2 and O_2) for various membrane structures is also vital, as gas crossover can pose safety risks, and imbalanced water transport can either reduce conductivity or cause mechanical failure. A comprehensive approach that captures these factors is essential to improve hydroxide conductivity and membrane performance.

2.2.2 Performance Assessment of Water Electrolyzer

The performance of water electrolyzers is evaluated using various metrics that indicate the system's effectiveness and reliability in hydrogen production relative to the electrical energy it receives. Cell voltage (V_{cell}) is the most fundamental measure, representing the necessary electrical potential to sustain hydrogen production at a specific current. The reversible voltage (V_{rev}) represents the minimum electrical potential required to initiate the electrolysis reaction. However, in practice, the actual cell voltage exceeds V_{rev} due to unavoidable voltage losses within the electrolysis cell, primarily arising from activation, ohmic, and concentration overpotentials. The voltage-current (V-I) curve, commonly referred to as the polarization curve, is crucial for understanding these losses. Each type of loss is associated with specific components of the cell or results from their combined effects, making it important to examine them in greater detail. This framework enables the investigation of how operating conditions, electrode materials, and membrane properties influence reaction kinetics and internal resistance within the cell.

Efficiency is commonly used as a key indicator of electrolyzer performance. In the literature, various efficiency metrics have been proposed considering different aspects, including energy, thermal, electrolyte, Faradaic, and voltage efficiencies (S. Ding et al., 2022; Y. Xia et al., 2024). Most of the time, a water electrolyzer's efficiency can be characterized by its higher heating value (HHV) and lower heating value (LHV), which represents the total heating energy of the generated hydrogen (Kim et al., 2024). It can also be defined in terms of voltage efficiency, which is calculated by dividing the reversible voltage by the cell voltage (Scheepers et al., 2021). Faradaic efficiency, on the other hand, quantifies how effectively electrons contribute to the

electrochemical reaction by comparing the actual hydrogen output with the theoretical amount expected from the applied current (Rasal et al., 2024).

Long-term performance is typically assessed through indicators of durability and stability, often by monitoring voltage fluctuations during extended testing periods. To ensure adaptability, systems built for this purpose should exhibit chemical and thermal stability, minimal performance degradation over time, and a long operational lifespan. At a system level, comprehensive indicators such as specific energy consumption and overall system efficiency offer a more insightful perspective by linking the cell's behavior with the plant's consumption. These metrics provide a clear understanding of how material properties, operating parameters, and effective management strategies influence the overall performance and reliability of AEMWE systems.

Factors such as electrolyte composition and molarity, temperature, pressure, and electrode design crucially affect ionic conductivity, reaction rates, and overall efficiency. In addition, the selection of membrane and electrode materials, as well as any surface or structural treatment applied to them, plays a crucial role in determining long-term stability and electrochemical performance (F. Li et al., 2024; Nara et al., 2024; Palmas et al., 2023; J. E. Park et al., 2019; L. Xia et al., 2024). The solution employed in AEMWEs has a strong influence on the overall performance of the electrolyzer, particularly through its impact on the membrane's ohmic resistance and the electrode's activation overpotential. Studies using potassium hydroxide (KOH) (Fortin et al., 2020; Gatto et al., 2023) and sodium hydroxide (NaOH) (X. Hu et al., 2021; D. Li et al., 2020; Nara et al., 2024) solutions demonstrate that the molarity of the electrolyte is a decisive factor. An increase in molarity generally correlates with enhanced cell efficiency, whereas deionized (DI) water typically results in the poorest performance (Ahmed et al., 2022; Campagna Zignani et al., 2022; B. Chen et al., 2022; Faid et al., 2022; Fortin et al., 2020; Gatto et al., 2023; C. Li & Baek, 2021; D. Li et al., 2020; J. E. Park et al., 2019; Vincent et al., 2021). According to Razmjooei et al. (2020), the most pronounced performance improvement in AEMWE was observed as the KOH concentration increased from 0.1 to 0.3 M, beyond which further increases were restricted by the rising viscosity that caused gas bubble surface coverage and partial blockage of active catalyst sites. The study further indicated that membrane

ohmic resistance was the dominant loss at low KOH concentrations, suggesting that optimized membranes and plasma-sprayed electrodes can deliver stable performance even under mild alkaline conditions. Most AEMWE systems operate in highly alkaline environments (around 1 M KOH) to maintain high performance. However, durability remains a major challenge to large-scale implementation, as operating at lower alkalinity or with pure water may alleviate degradation effects. While alkaline-fed AEMWE systems exhibit higher ionic conductivity and current densities, they also encounter issues such as carbonate formation, toxicity, and higher cost. Conversely, pure-water operation eliminates carbonate formation and corrosion risks but suffers from low ionic conductivity (Shaik et al., 2024). Therefore, ongoing research efforts focus on maintaining high efficiency while reducing the alkalinity of the operating environment (Shen et al., 2025).

Among the key operating parameters, temperature plays a crucial role in determining electrolyzer performance. As temperature rises, membrane conductivity improves and electrode kinetics are enhanced, reducing both ohmic and activation overpotentials, with the effect being particularly pronounced at lower temperature ranges (Fortin et al., 2020; Gatto et al., 2023; J. E. Park et al., 2019; Vincent et al., 2021). Higher operating temperatures are therefore generally desirable due to these performance gains; however, excessive temperatures can lead to membrane dehydration, mechanical stress, and component degradation, ultimately reducing long-term stability. Hence, continuous operation at temperatures exceeding approximately 70 °C is uncommon, as most currently available membrane materials lack sufficient thermal stability (Q. Xu et al., 2022).

To achieve effective hydrogen production, it is crucial to optimize both the electrode design and operating conditions. These include factors such as catalyst layer porosity, the amount and distribution of polymer binder, and the exposed active surface area of the catalyst. The selection of electrode material directly influences the performance of OER at the anode and HER at the cathode. Adding ionomer content to the catalyst layer is vital for establishing ionic contact between the catalyst and the membrane in AEMWEs. This incorporation plays a key role in improving cell performance by enhancing ion transport and functioning as a catalyst binder. It also

significantly affects ohmic overpotential values and mass transport (Fortin et al., 2020). However, identifying an optimal ionomer content is critical, as excessive amounts can lead to a notable decline in cell performance (B. Chen et al., 2022; Y. S. Park et al., 2023).

2.2.3 Materials for AEMWE

The performance and longevity of AEMWEs are closely linked to the characteristics of their electrode and membrane materials. Therefore, ongoing studies are focusing on fabricating electrodes that offer both chemical and physical robustness, as well as cost-effectiveness and efficiency (Faid et al., 2021; Y. S. Park et al., 2020).

The electrode materials directly influence the reaction rates, thus efficient electrocatalysts are essential to advance the process (Hota et al., 2023). For alkaline-media OER, especially NiFe-based materials exhibit robustness, offering good performance and stability (G. Ding et al., 2023; Jin et al., 2021; Thangavel et al., 2023). For instance, Ni_2Fe_8-Ni_3S_2/NF catalyst, developed by G. Ding et al. (2023), exhibited superior performance compared to commercial RuO_2/NF and IrO_2/NF catalysts. It achieved a current density of 1 A cm^{-2} at an overpotential (η) of 302 mV in 1 M KOH. Furthermore, it provided a Tafel slope of 55.3 mV dec^{-1}, enabling accelerated catalytic kinetics compared to RuO_2/NF (84.4 mV dec^{-1}) and IrO_2/NF (89.6 mV dec^{-1}). Moreover, when combined with the HER catalyst (Ni_4Mo/MoO_2/NF) in a single-cell AEMWE, it exhibited notable durability, maintaining stable performance for over 100 hours at a current density of 1 A cm^{-2}. Similarly, Thangavel et al. (2023), observed that a V-NiFeOOH/Ni_3N/NF electrode achieves superior performance compared to commercial IrO_2-based electrodes. The electrode demonstrated a current density of 587 mA cm^{-2} at 1.8 V in an AEMWE operated with pure water at 70 °C. The electrode also demonstrated remarkable durability, maintaining its performance for over 1000 hours. Motealleh et al. (2021), utilized $NiFe_2O_4$ (2 mg cm^{-2}) as the anode, modified Raney nickel (3 mg cm^{-2}) as the cathode, and Sustainion® X37-50 as the membrane in their electrolyzer. The system demonstrated stable performance for over 10,000 hours with a degradation rate of approximately 1 $\mu V\ h^{-1}$, indicating a projected lifetime exceeding 20 years. On the other hand, for the HER, platinum-group catalysts remain the benchmark owing to their excellent catalytic activity and stability under alkaline

conditions (C. Li & Baek, 2021). However, these materials encounter scalability challenges due to their limited availability and high cost.

The performance of membrane materials is evaluated based on various properties such as water uptake, permeability, ionic conductivity, ion exchange capacity, and mechanical strength. Among these, ion exchange capacity (IEC) is typically the first metric of interest as it provides an initial indication of a membrane's performance and suitability for further testing and development. Increasing the IEC is the most immediate approach to improving the conductivity of AEMs. However, excessively high IEC can result in severe water swelling and a significant decrease in mechanical strength. Therefore, achieving high conductivity while maintaining low water uptake (WU) and minimal swelling is a key challenge in the development of AEMs (Karas et al., 2014; W. Lu et al., 2020). To attain optimal performance, a thorough examination of the MEA parameters is critical, as well as the system parameters.

2.2.4 Selection of Membrane for AEMWE

AEMs can be examined based on both their polymer backbone and functional groups. The polymer backbone governs chemical stability and influences key properties such as mechanical strength, solubility, and thermal resistance (S. A. Lee et al., 2022). The most common and technologically relevant backbones include poly(arylene ethers) of various chemistries, as well as polyphenylenes, perfluorinated, and polybenzimidazole (PBI) types (Varcoe et al., 2014b). Cationic functional groups, primarily nitrogen-based species such as quaternary ammonium (QA), imidazolium (IM), and piperidinium (Pip), play a key role in determining IEC, hydroxide conductivity, and alkaline durability. (S. A. Lee et al., 2022; Varcoe et al., 2014b). QA groups, though widely used for their high ionic conductivity, are strongly electrophilic and therefore highly susceptible to hydroxide ion attack in alkaline media. They degrade mainly through nucleophilic substitution at the α-carbon and β-hydrogen abstraction via Hofmann elimination, along with other complex degradation pathways (Wijaya et al., 2024; Xue et al., 2022). Furthermore, in contrast to earlier studies that treated the backbone and functional groups independently, recent research highlights the importance of evaluating them together, as the overall polymer architecture governs both the degradation mechanisms and rates (N. Du et al., 2022).

While AEMs with ether-containing backbones, such as poly(arylene ether) polymers, have been widely used for their cost-effectiveness and ease of fabrication, the ether bonds within their structures are highly susceptible to OH^- attack in alkaline environments, leading to backbone degradation (Q. Lu et al., 2025). Thus, AEMs containing ether linkages generally exhibit poor chemical resistance and limited alkaline stability, and consequently reduced durability (Wijaya et al., 2024). To overcome these drawbacks, recent research has focused on developing ether-free backbones, which offer significantly improved chemical robustness and long-term stability under alkaline conditions (Vinodh et al., 2023; Xue et al., 2022). Nevertheless, ether-containing AEMs with a stable aromatic backbone and an optimized side-chain architecture can also achieve desirable alkaline stability and ionic conductivity (J. Chen, Shen, et al., 2025).

Polybenzimidazole (PBI)-based aromatic heterocyclic polymer AEMs stand out for their ether-free structure and exceptional chemical and thermal stabilities (Chiu et al., 2025). They are known for their outstanding thermomechanical strength arising from the unique benzimidazole repeating units (N. Du et al., 2022; Guo et al., 2022). However, in their undoped or unfunctionalized state, PBI membranes exhibit relatively low ionic conductivity compared to other AEM types, and solubility limitations may occur when applied in AEMWEs (Chiu et al., 2025; Guo et al., 2022). Since PBI itself cannot operate effectively in pure water environments (S. A. Lee et al., 2022), it typically requires an alkaline medium to conduct ions and is therefore employed under highly alkaline conditions (Boström et al., 2023). Nevertheless, when doped or functionalized, PBI can achieve sufficient ionic conductivity even in milder alkaline environments. The excellent high-temperature performance and remarkable alkaline stability of PBI make it a promising material for high-temperature AEMWE applications (J. Y. Lee et al., 2025). In addition, recent developments in PBI-based membranes have shown improvements in ionic conductivity while maintaining stability (e.g., chemical and temperature), which are crucial for the long-term efficiency and durability of the electrolyzer (Guo et al., 2023, 2024).

2.3 System Architectures of AEMWE-Based Systems

Examining AEMWEs at both the BoP level and in integrated generation and storage configurations provides critical information about their practical performance and real-world applicability. Placing this assessment in the context of technological maturity helps guide ongoing design and optimization efforts. The Technology Readiness Level (TRL) framework provides a standardized method for assessing the maturity of a process or system, ranging from TRL 1, where only the basic scientific principles have been established, to TRL 9, which represents full commercialization and operation in real-world environments (Shaya & Glöser-Chahoud, 2024). At present, AEMWE technology is estimated to be at TRL 6 (Sebbahi et al., 2024), corresponding to the stage where the technology has been demonstrated in a relevant environment but has not yet reached full commercial maturity. Focusing on optimization at both the cell and stack level and on system-level design is crucial to improving AEMWE performance and advancing technology readiness for commercialization.

2.3.1 Balance of Plant Components

The Balance of Plant (BoP) is the auxiliary system of AEMWEs, incorporating essential components for fluid circulation, temperature regulation, pressure control, and gas handling. Depending on the system configuration, the BoP may consist of a water-electrolyte tank, auxiliary equipment such as a separator, a chiller or a cooler, and pumps and valves. During start-up and heating phases, it encounters additional thermal and flow transients that require precise control to ensure efficient and balanced stack heating. An electrolyte solution, typically between 0.1 and 1 M, is circulated from the electrolyte tank to the anode inlet of the electrolyzer using a pump. The electrolyte and oxygen mixture exiting the stack outlet is directed back to the tank. Here, oxygen is separated and transferred to the gas separator, where pure oxygen is collected, while the electrolyte solution is recirculated back to the anode via a recirculation pump. Hydrogen produced at the cathode is condensed and extracted from the system as purified H_2. The Power Supply Unit (PSU), comprising transformers and rectifiers, converts the grid's alternating current (AC) into DC (Sakas et al., 2025), while the entire system's operation is monitored and regulated, usually by a PID control system that utilizes various sensors for dynamic control.

A schematic representation of a typical AEMWE system and BoP components is shown in Figure 2.8.

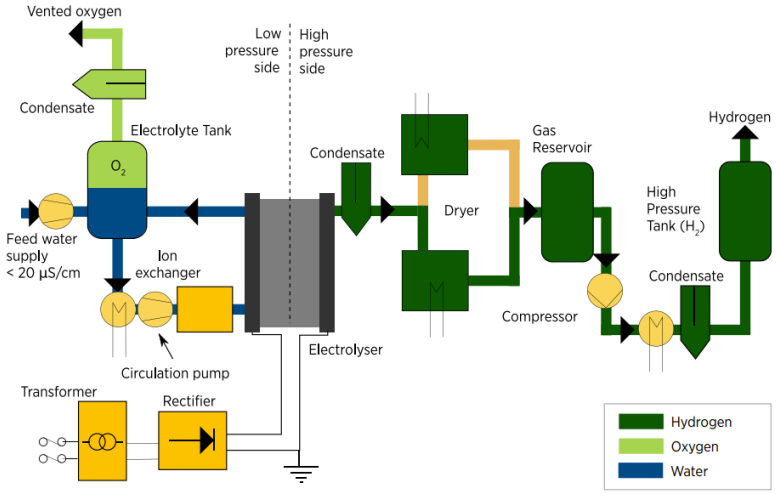

Figure 2.8 Typical system design and Balance of Plant (BoP) for an anion exchange membrane (AEM) electrolyzer. Source: International Renewable Energy Agency (IRENA), 2020

For product gas handling, the crude hydrogen from the cathode passes through condensation and separation steps. To achieve a high final purity (>99.999%), additional conditioning is needed, often involving a Pressure Swing Adsorption (PSA) dryer to remove moisture and trace oxygen (Crespi et al., 2023). However, this PSA regeneration process, which vents a small stream of product gas, is a major parasitic loss and the primary contributor to poor performance, especially at low to part-load operation.

In addition to these core components, supplementary devices such as filters and compressors may be employed depending on the specific system requirements. Hydrogen released at the cathode is then directed to a compressor, depending on the pressure requirements. Current AEMWE stacks can produce hydrogen at pressures of up to 30 bar without requiring external compression; however, higher storage pressures necessitate an additional compressor.

Under normal operating conditions, electrolyte circulation plays a crucial role in maintaining membrane hydration and minimizing ohmic losses. Another distinctive feature of AEMWE systems is their ability to operate with either pure water or dilute alkaline solutions. Adequate solution flow ensures stable ionic conductivity and

uniform current distribution across the active area. Insufficient flow or temporary interruptions in electrolyte supply can lead to local membrane dehydration, resulting in increased resistance and performance degradation. If the membrane remains unhydrated for an extended period, irreversible structural damage may occur, resulting in reduced efficiency and durability. Therefore, proper management of electrolyte flow and operating conditions is essential to sustain stable AEMWE performance. Furthermore, since the sudden application of voltage during start-up accelerates stack degradation, a gradual voltage increase should be implemented for stable operation.

A KOH feed is required to maintain the electrolyte concentration within the desired range in the tank. In commercial applications such as the ENAPTER EL 4.1 electrolyzer, the KOH solution is provided as a separate kit. This kit allows the preparation of the electrolyte by mixing KOH pellets with demineralized water in specified proportions (ENAPTER Owner's Manual Electrolyzer 4.1, 2025). To compensate for water consumption during electrolysis, the water level in the tank must be monitored, either continuously or by using a level sensor. The feed water must meet specific purity requirements; suitable water may be supplied directly or filtered to reduce conductivity below 20 μS/cm (International Renewable Energy Agency (IRENA), 2020). For the ENAPTER EL 4.1 system, the manufacturer specifies a water acidity of <0.1 meq/L and a minimum conductivity of <2 μS/cm (ENAPTER Owner's Manual Electrolyzer 4.1, 2025).

Thermal management plays a crucial role in maintaining stable operation, as the overpotentials in the stack lead to heat generation through electrochemical and resistive losses. Waste heat is mainly dissipated through water circulation in heat exchangers and a dedicated cooling loop. When defining the heating strategy, configurations that are compatible with the electrolyzer's operating principles and require minimal energy consumption are preferred. The most viable and stable method involves preheating the electrolyte tank and circulating the electrolyte to warm up the stack. This way, both external heating and internally generated heat can be utilized (Gladik et al., 2025).

2.3.2 System-Level Modeling Studies

Water electrolysis can be integrated with both grid-connected and off-grid renewable sources. This flexibility is especially beneficial in systems with variable generation, such as solar and wind, enabling energy storage as hydrogen during periods of high power supply (Titheridge & Marshall, 2024).

With the growing prevalence of PV technologies, the installation of PV-electrolyzer systems has attracted significant attention in recent years (Ghosh, 2025). In directly coupled hydrogen production systems, the ability of electrolyzers to integrate with intermittent energy sources is therefore crucial. For example, a PV panel must quickly respond to fluctuations in electrical power output, such as those caused by passing clouds, and these dynamic variations can potentially affect the purity of the produced hydrogen (Endrődi et al., 2025). Although AWEs are the most mature technology in terms of development and commercialization, their compatibility with renewable energy integration remains limited due to their poor performance at low current densities (Y. Xia et al., 2023). PEMWE, on the other hand, while capable of dynamic operation, requires expensive materials that increase system costs (Sebbahi et al., 2024). AEMWEs offer a promising alternative by combining the advantages of both technologies: low-cost materials, high efficiency, and compatibility with intermittent power sources (Younus et al., 2025). Nevertheless, the current limited durability of AEMWE stacks remains a key challenge. Achieving the desired performance and lifetime targets will enable AEMWE technology to become viable for large-scale hydrogen production.

Moreover, the economic and technical challenges associated with storing the produced hydrogen are one of the problems preventing the widespread use of these systems. Most storage technologies, particularly for portable and mobile applications, face limitations in terms of safety, efficiency, and feasibility. To address these challenges, hydrogen can also be converted into liquid energy carriers under environmentally friendly conditions, such as ammonia and methanol, in a process collectively known as Power-to-X (PtX) (Endo et al., 2021).

The choice of an appropriate storage method has a significant impact on the overall system configuration and energy management strategy. Hydrogen can be stored in different forms, such as compressed gas, cryogenic liquids, and solid-state materials. (Cheng et al., 2024). Conventional compressed and liquid hydrogen storage methods have several disadvantages, such as high energy consumption, low storage density, and safety risks. Alternatively, metal hydride systems, where hydrogen is stored in solid form by forming chemical bonds with metal atoms, are gaining prominence. These systems offer high storage capacity at low pressures, enabling the safe transport of hydrogen (N. Kumar et al., 2024). In metal hydride storage systems, depending on the material, a significant amount of heat may be released during hydrogen absorption, while an effective heat supply is required during desorption. Without an effective thermal management strategy, metal hydride tanks might not fully reach their storage capacity, which reduces the storage performance and limits overall efficiency. Therefore, solutions such as metal foams, copper matrices, and finned-tube heat exchangers are considered effective approaches that enhance heat transfer and contribute to more efficient system operation (Nyamsi & Tolj, 2024). Table 2.2 presents a summary of studies on hybrid metal hydride coupled electrolyzer systems, encompassing different scales and application purposes.

Table 2.2 Summary of studies involving electrolyzer-metal hydride storage systems

Study	System Configuration	Approach / Methodology	Outcomes
Cogeneration system combining reversible PEM fuel cell, and metal hydride hydrogen storage enabling renewable energy storage: Thermodynamic performance assessment (Bhogilla et al., 2024)	Reversible PEM (EC + FC) + AB_5 MH + Vapour Absorption Refrigeration System	Thermodynamic energy and exergy modeling involves system-level analysis to investigate performance and heating coupling. Heat transfer and kinetics are simplified, and no detailed metal hydride model is included.	The energy and exergy efficiencies were calculated as 73.3% and 59.5%, respectively. EC efficiency was 85.6% and the implementation of heat recovery from MH notably enhanced overall performance, achieving an efficiency of 94%.

Table 2.2 (Continued)

Study	System Configuration	Approach / Methodology	Outcomes
Experimental analysis on a Power-to-Hydrogen system based on PEM electrolysis and metal hydrides: Empirical correlations for optimal system design and performance improvement (Alleori et al., 2025)	Grid electricity + 2.5 kW PEM electrolyzer + AB_2 MH canisters (190-800 NL) + water-cooling circuit	Experimental tests were conducted using a floating load/pressure-based control, with varying canister sizes, thermal conditioning, and cooling fluids, to analyze electrical/thermodynamic parameters, efficiency, hydrogen venting, and current ripple.	The larger, thermally conditioned MH tanks ensure optimal coupling, maximizing stored hydrogen and renewable energy recovery with a mean stack efficiency of 61.4%. The hydrogen vent logic at low loads and current ripple frequency also heavily impacts system performance.
Pilot-scale hydrogen energy utilization system demonstration: A case study of a commercial building with supply and utilization of off-site green hydrogen (Segawa et al., 2024)	On-Site: PV + PEMWE (5 $Nm^3\ h^{-1}$ 26 kW) + Battery + TiFe-based MH tanks (40 + 100 Nm^3) + PEMFC (3.5 kW × 4) Off-site: High-pressure H_2 cylinders (19.6 MPaG) delivered to on-site and absorbed into MH tanks (< 1 MPaG)	Demonstration-scale hybrid system; dynamic energy management via BEMS; water-cooled MH tanks for heat removal during rapid charging; integrated thermal-electrical control between PV, EC, FC, and MH subsystems	Verified stable H_2 production-storage-useage; smooth power balance among components; safe MH absorption/desorption under low pressure; maintained continuous FC supply and efficient waste-heat utilization. CO_2 emissions reduced to zero with 300 Nm^3 green H_2 validated rapid-fill MH tank design.
Construction and operation of hydrogen energy utilization system for a zero emission building (Endo et al., 2019)	20 kW PV + 26 kW PEMWE + TiFe MH (80 Nm^3) + 3.5 kW PEMFC + Li-ion battery	The experimental field operation was conducted under real building conditions, where fluctuations in PV power and building load were the main external variables. A passive cooling strategy was used to dissipate the heat generated by the MH tanks during absorption.	Stable 24-h operation with nearly zero grid power consumption was achieved. EC-MH coupling enabled efficient H_2 storage, while FC-MH thermal integration allowed heat reuse during desorption, enabling full desorption through partial use of the FC heat output.

Table 2.2 (Continued)

Study	System Configuration	Approach / Methodology	Outcomes
Definition, analysis and experimental investigation of operation modes in hydrogen-renewable-based power plants incorporating hybrid energy storage (Valverde et al., 2016)	Hybrid renewable (PV + wind) powered micro plant with 1 kW PEMWE + 7 Nm^3 MH + 1.5 kW PEMFC + 367-Ah lead-acid battery bank	Dynamic simulations and experimental validation of six operation modes with different power flow strategies. The MH tank was modeled under isothermal conditions without thermal coupling or temperature effects.	No single mode was universally optimal; performance varied with weather conditions and operational strategy, based on efficiency and cost balance. Overall efficiency ranged from 65% to 87%; Partial Load and EC-rated modes enhanced H_2 utilization.
Design, testing, and evaluation of a community hydrogen storage system for end user applications (Parra et al., 2016)	A community-scale PV + grid hybrid energy system integrating a PEMWE + MgH_2 MH + PCM thermal management + PEMFC	A community-scale hydrogen storage loop was experimentally validated under tariff- and irradiance-based operation. MH tanks were thermally controlled by PID heaters with buffer-regulated hydrogen flow.	PV fluctuations impacted the balance between hydrogen production and storage. Surplus PV power was charged into the MH tank via the electrolyzer, ensuring continuous demand and supply with a 52% round-trip efficiency and 65% electrolyzer efficiency.
Techno-economic analysis of metal hydride-based energy storage system in microgrid (K. Kumar et al., 2019)	5 kWp PV + 0.6 kW AWE + $LaNi_5$ MH tank (5000 L) + 1 kW PEMFC + optional battery	HOMER simulation for techno-economic assessment of different microgrid configurations (PV-grid / PV-battery / PV-EC-MH-FC / hybrid); experimental setup described but not validated; no specific model implemented for MH tanks.	The study evaluated LCOE, system sizing, and emissions for different microgrid configurations using HOMER simulation. The PV-EC-MH-FC system achieved autonomous (off-grid) operation but exhibited a higher LCOE (0.383 $/kWh) than the PV-battery configuration (0.129 $/kWh).

Table 2.2 (Continued)

Study	System Configuration	Approach / Methodology	Outcomes
Charging dynamics of metal hydride hydrogen storage bed for small wind hybrid systems (Raju & Khaitan, 2011)	Small-scale wind + AWE + $LaNi_5$ MH bed for off-grid supply	The numerical model developed in MATLAB/Simulink incorporates the effects of turbulent wind velocity and provides analyses of the cooling management employed. The MH model represented is a zero-dimensional lumped model.	Examined transient H_2 absorption dynamics under variable wind power, highlighting the importance of effective thermal management for the overall system performance.

Recent industrial projects are demonstrating the transition of metal hydride storage technologies from laboratory scale to commercial applications. NREL's HEVHY METAL project, developed in collaboration with GKN Hydrogen, represents a significant step toward the commercial deployment of metal hydride hydrogen storage technology (*Heavy Metal Debut: A World-Class Metal Hydride System | NREL*, n.d.). The system integrates 1.25 MW PEMWE, 500 kg of metal hydride storage, and 1 MW PEM fuel cell. The aim is to validate performance under real operating conditions, including waste heat recovery systems and load responses. A successful implementation will provide a safe and efficient alternative to traditional compressed or cryogenic hydrogen storage systems, paving the way for large-scale commercial adoption of MH applications.

Meanwhile, several Hydor metal hydride systems are already in operation, with storage capacities ranging from 0.15 kg H_2 in small mobile units to 14.4 kg H_2 in large stationary plants (*Methydor – Friendly Hydrogen Storage*, n.d.). Current efforts demonstrate the enhancement of commercial viability and adaptability of metal hydride storage technologies, highlighting their potential for further advancements and applications in the industry.

CHAPTER THREE
METHODOLOGY

3.1 AEMWE Modeling

This section focuses on the modeling of the Anion Exchange Membrane Water Electrolyzer (AEMWE). The modeling framework is divided into two subsections.

At first, the cell-level model represents electrochemical behavior within a single cell and establishes the relationship between current density, cell voltage, and operation conditions.

3.1.1 Cell-Level Modeling of AEMWE

An AEMWE involves complex transport phenomena and electrochemical reactions. In this study, a zero-dimensional (0D) model was developed to establish the relationship between cell voltage and current density. The 0D approach assumes uniform temperature, pressure, and reactant distribution across the cell, allowing for a simplified yet insightful analysis that focuses on key parameters such as membrane conductivity and electrode kinetics.

Two different approaches for calculating the reversible voltage were compared to improve the accuracy and ensure a more reliable prediction of the thermodynamic cell potential. Although mass transport effects are not explicitly modeled, the influence of gas bubble formation, which affects the active surface area, is included to capture its impact on performance better.

The parameters used in the study were carefully selected to be material-specific, taking into account varying effects. The primary objective of the model is to identify the factors that cause deviations between the actual and ideal cell voltages and to observe their effects. The equations were solved in MATLAB. The fsolve solver was used to solve the nonlinear algebraic equations because it provides more consistent results compared to other numerical methods, such as the Newton-Raphson and Bisection methods.

Several factors, including the reversible cell voltage, ohmic losses, kinetic losses, and losses related to mass transport, influence the cell voltage (V_{cell}). An understanding of these factors is essential to determine the cell voltage accurately, which is represented in Eq. 3.1.

$$V_{cell} = V_{Rev} + \eta_{act,a} + \eta_{act,c} + \eta_{ohm} + \eta_{KOH} + \eta_{Bub} \quad (3.1)$$

3.1.1.1 Thermodynamic Cell Voltage

Thermodynamic (also known as reversible) cell voltage refers to the theoretical minimum voltage necessary to initiate electrolysis within a cell under ideal conditions. This voltage is calculated based on the Nernst equation, as described in Eq. 3.2 (S. Ding et al., 2022).

$$V_{Rev} = -\frac{\Delta G}{nF} + \frac{RT}{nF}\log\frac{(P-p_{H_2O})^{1.5}}{a} \quad (3.2)$$

R, n, and F represent the universal gas constant ($J/mol \cdot K$), the number of electrons transferred in the reaction, and Faraday's constant (96485.3 C/mol), respectively. ΔG, the standard Gibbs free energy change, was calculated using Eq. 3.3.

$$\Delta G = \Delta H - T\Delta S \quad (3.3)$$

Enthalpy (H) and entropy (S) values in the equation were obtained using the variable specific heat (c_p) approach as described in Eqs. 3.4-3.8 for each species (Mench, 2008).

$$\bar{h} = \int_{T_{ref}}^{T_2} \bar{c}_p dT \quad (3.4)$$

$$\bar{s} = \int_{T_{ref}}^{T_2} \frac{\bar{c}_p}{T} dT \quad (3.5)$$

$$\Delta H = (\bar{h}_{f,H_2O} + \bar{h}_{H_2O}) - (\bar{h}_{H_2}) - 0.5 \cdot (\bar{h}_{O_2}) \quad (3.6)$$

$$\Delta S = (\bar{s}_{0,H_2O} + \bar{s}_{H_2O}) - (\bar{s}_{0,H_2} + \bar{s}_{H_2}) - 0.5 \cdot (\bar{s}_{0,O_2} + \bar{s}_{O_2}) \quad (3.7)$$

$$\frac{\bar{c}_p(T)}{R_u} = A + B \cdot 10^{-3} \cdot T + C \cdot 10^{-6} \cdot T^2 + D \cdot 10^{-9} \cdot T^3 + E \cdot 10^{-12} \cdot T^4 \quad (3.8)$$

The coefficients $A - E$ used for each species in Eq. (3.8) are listed in Table 3.1.

Table 3.1 Coefficients for specific heat calculations of each gas species (Mench, 2008).

	A	B	C	D	E
H_2O	3.057	2.677	-5.810	5.521	-1.812
O_2	3.626	-1.878	7.055	-6.764	2.156
H_2	4.070	-1.108	4.152	-2.964	0.807

p_{H_2O} and a refer to partial pressure of water vapor in the electrolyzer and the activity of water, which are calculated in terms of molarity (M) and temperature (T) using Eqs. 3.9 and 3.10, respectively (S. Ding et al., 2022).

$$\begin{aligned}\log p_{H_2O} = {} & -0.01508M - 0.0016788M^2 + 2.25887 \times 10^{-5}M^3 \\ & + (1 - 0.0012062M + 5.6024 \times 10^{-4}M^2 - 7.8228 \times 10^{-6}M^3) \\ & \times (35.4462 - \frac{3343.93}{T} - 10.9 \log T + 0.004165T)\end{aligned} \quad (3.9)$$

$$\log a = -0.0225M + 0.001434M^2 + (\frac{1.38M - 0.9254M^2}{T}) \quad (3.10)$$

As an alternative method for calculating the reversible cell voltage, Eq. 3.11, a linearized approach commonly used in the literature, can be employed instead (Awasthi et al., 2011).

$$V_{Rev} = 1.229 - 0.9 \cdot 10^{-3} \cdot (T - 298) \quad (3.11)$$

3.1.1.2 Overpotentials in AEMWE

The deviation of the actual cell voltage from the reversible voltage primarily arises from various overpotentials associated with charge-transfer kinetics, ionic resistance, and mass transport limitations. In the developed AEMWE model, overpotentials arising from activation, ohmic resistance, and losses induced by gas bubbles and the KOH electrolyte are considered.

Activation overpotential refers to the additional voltage required to drive the electrochemical reactions at the electrodes by overcoming the kinetic energy barriers. It is calculated as shown in Eqs. 3.12 and 3.13 for the anode and cathode electrodes, respectively, combining the traditional Butler-Volmer equation with bubble formation (S. Ding et al., 2022).

$$i_a = i_{0,a}\,(1-\Theta)\,\{\exp(\frac{\alpha_a\, n\, F}{RT}\eta_{act,a}) - \exp(\frac{-(1-\alpha_a)\, n\, F}{RT}\eta_{act,a})\} \quad (3.12)$$

$$i_c = i_{0,c}\,(1-\Theta)\,\{\exp(\frac{\alpha_c\, n\, F}{RT}\eta_{act,c}) - \exp(\frac{-(1-\alpha_c)\, n\, F}{RT}\eta_{act,c})\} \quad (3.13)$$

i_0 is the exchange current density (A/m^2) and η_{act} is the activation overpotential (V), and α stands for charge transfer coefficient, which is determined from the Tafel slope (b) using Eq. 3.14 (H. Wang et al., 2022).

$$b = \frac{2.303RT}{\alpha nF} \quad (3.14)$$

n is the number of electrons transferred per mole of the species of interest. At the cathode, 2 mole-eq of electrons are required to produce 1 mole of H_2, while at the anode, 4 mole-eq of electrons are involved in generating 1 mole of O_2, as can be seen in Eqs. 2.7 and 2.8. In the charge transfer coefficient calculation (Eq. 3.14), the n values were set to 4 and 2 for the anode and cathode, respectively. However, for the activation overpotential calculations (Eqs. 3.12 and 3.13), n was assumed to be 2 for both electrodes.

The formation of bubbles at the electrode can block the electrocatalyst surface and ion-conducting pathways in the electrolyte. This may result in energy loss, reducing overall system performance (Vogt & Balzer, 2005). Eq. 3.15 (Jang et al., 2021) describes the bubble coverage, which relates the bubble effect to the applied current. This has been integrated into activation and ohmic losses, also calculated as an overpotential value using Eqs. 3.16 and 3.17 (Henao et al., 2014). In the calculations, T_{ref} was set to 273.15 K and P_{ref} to 1 atm. The current is defined as the product of the current density and the active cell area.

$$\Theta = 0.023j^{\,0.3\left(\frac{P_{ref}}{P}\times\frac{T}{T_{ref}}\right)^{1.5}} \quad (3.15)$$

$$R_{bub} = \frac{1}{(1-\frac{2}{3}\Theta)^{\frac{3}{2}}} - 1 \quad (3.16)$$

$$\eta_{bub} = R_{bub}\cdot I \quad (3.17)$$

Ohmic overpotential is caused by ionic resistance and increases almost linearly with the applied current. This voltage was calculated as shown in Eq. 3.18, where i (A/m^2)

signifies the current density and the values of ohmic resistance, R_{mem} (Ωm^2), extracted from the literature.

$$\eta_{ohmic} = R_{mem} \cdot i \tag{3.18}$$

The resistance of the KOH solution and its effects on overpotential were calculated depending on its molarity and temperature using Eqs. 3.19-3.21 (S. Ding et al., 2022).

$$\sigma_{KOH} = -2.041M - 0.0028M^2 + 0.005332M.T + 207.2\left(\frac{M}{T}\right) + 0.001043M^3 - 0.0000003(M^2.T^2) \tag{3.19}$$

Where σ_{KOH} presents the conductivity in S/cm, M represents the molarity in mol/L, and T represents the temperature (K).

$$R_{KOH} = \frac{1}{\sigma_{KOH}\left(1-\left(\frac{2}{3}\Theta\right)\right)^{1.5}}\left(\frac{d_{am}}{S_a} + \frac{d_{cm}}{S_c}\right) \tag{3.20}$$

$$\eta_{KOH} = R_{KOH} \cdot I \tag{3.21}$$

Here, d_{am}, d_{cm}, and S_a, S_c values represent the distance between the anode or cathode and the membrane and the anode and cathode cross-sectional surface areas, respectively, in m and m^2. One of the key parameters that significantly impacts AWE performance is the distance between the electrodes (Amores et al., 2014). As this distance increases, the efficiency of electrolysis decreases due to the electrolyte resistance and also the formation of bubbles caused by the HER and OER reactions. To mitigate this issue, AEMWEs are designed with a zero-gap approach similar to PEMWEs (Loh et al., 2023). However, it is considered likely that the d_{am} and d_{cm} parameters defined in Eq. 3.20 may differ depending on the experimental conditions. Given the "zero-gap" design approach, it is assumed that the value of these parameters will be significantly lower than that observed in AWE electrolyzers. Even so, it is not expected to reach zero. Instead, it is expected to remain small but not negligible. For calculations, the default values for d_{am} and d_{cm} have been set at 7.5 μm, reflecting this reduced gap while still accounting for a minimal separation distance. In the literature, these values are often included in zero-gap AWE modeling where traditional separators are used. The study by Lira Garcia Barros et al. (2024), which examined the electrode-diaphragm gap in zero-gap AWE configurations, highlights that de Groot &

Vreman (2021), and Brauns et al. (2021), considered distances of 50 μm and 250 μm, respectively. Similarly, S. Ding et al. (2022), who modeled a zero-gap AWE, assumed a value of 1200 μm to fit their experimental model. For zero-gap configurations in AEMWE systems using membranes, a gap of 7.5 μm, significantly smaller than these values, appears to be appropriate, aligning well with experimental data and reflecting the zero-gap AEMWE designs.

The combined effect of these overpotentials results in energy losses that cause the actual cell voltage to exceed the reversible value, thus reducing the overall efficiency. The theoretical efficiency that can be achieved by an electrolyzer system depends on the amount of thermal energy released by the combustion of the fuel, expressed as the Heating Value (Aghbashlo et al., 2021). For electrolyzer systems, the energy content of the fuel is referred to as either the HHV or the LHV, depending on whether the water produced in the system is in liquid or gaseous form. In commercial AWEs and PEMWEs, where liquid water is commonly used, efficiency calculations are typically based on the HHV (Siracusano et al., 2012). For the AEMWE operating at similar temperatures, efficiency is determined using HHV efficiency, as defined by Eq. 3. 22.

$$\eta_{el} = \frac{\dot{m}_{H_2,produced} \cdot HHV}{P_{cell}} \tag{3.22}$$

The power used by the electrolyzer, which is calculated by multiplying the cell voltage (V_{cell}) and current (I) as shown in Eq. 3.23, represents the power input for the electrolyzer in units of W.

$$P_{cell} = V_{cell} \cdot I \tag{3.23}$$

The hydrogen flow (mol/s) generated at the cathode as a result of electrolysis is derived from Faraday's law and can be calculated in units of kg/s by multiplying it by the molar mass of hydrogen, as shown in Eq. 3.24.

$$\dot{m}_{H_2,produced} = \frac{I}{2F} \cdot \bar{M}_{H_2} \tag{3.24}$$

3.1.2 System-Level Modeling of AEMWE

At the system level, a model covering both the BoP components, focusing on electrolyte circulation and thermal management of the stack, is deployed. Followed by

the integrated PV-AEMWE-MH configuration, which allows the evaluation of power generation, hydrogen production, and storage performance under varying solar irradiation and load conditions.

3.1.2.1 Modeling of Balance of Plant

This subsection focuses on the thermodynamic modeling of the electrolyzer stack and electrolyte tank. The model considers the energy balance between electrical input, heat generation, and thermal losses, as well as the mass flow of reactants and products. Figure 3.1 illustrates the recirculation and cooling concept of the electrolyzer system.

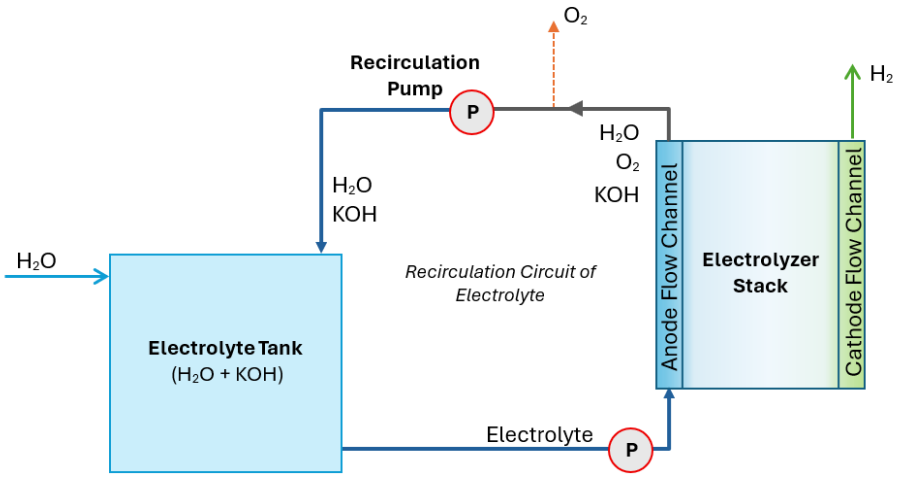

Figure 3.1 Recirculation and cooling concept of the electrolyzer system

When the electrolyte level falls below a predefined threshold, the electrolyte tank is supplied with make-up water to maintain a steady concentration, compensating for the water consumed during electrolysis. The electrolyte exiting the tank is pumped into the stack by the recirculation pump, and after electrolysis, the gas-liquid mixture leaving the anode is separated, enabling oxygen removal and water to return through the recirculation loop. Figure 3.2 describes the thermal behavior of this flow.

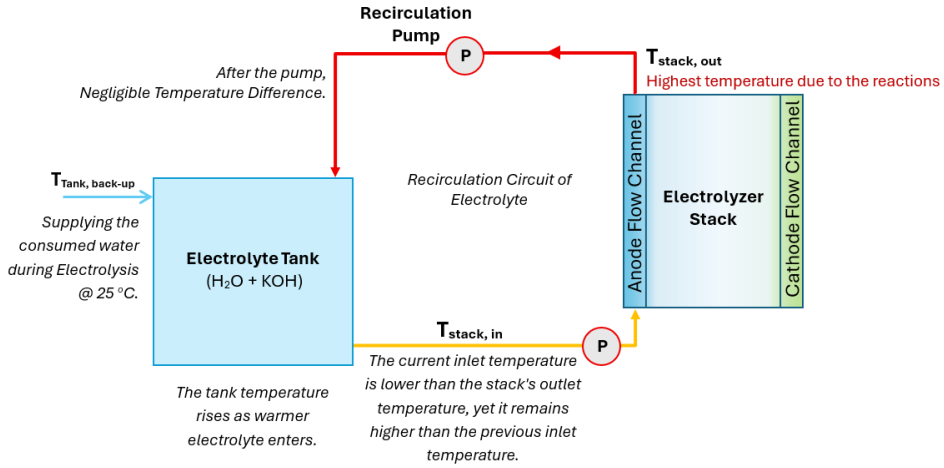

Figure 3.2 Circulation of the electrolyte between the tank and the stack.

The electrolyte, initially at room temperature in the tank, enters the electrolyzer stack at the same temperature and is heated by the electrochemical reactions taking place within the stack. The heated stream then returns to the tank, gradually raising the tank temperature. As a result, the electrolyte leaving the tank is cooler than the stream at the stack outlet but warmer than in the previous cycle. Consequently, the inlet stream to the stack becomes progressively warmer than its initial level but remains cooler than the stack itself, ensuring that the stack heats up until it reaches the desired operating temperature.

A dynamic energy and mass balance approach is applied to evaluate the temperature changes of both the electrolyzer stack and the electrolyte tank. Figure 3.3 illustrates the control volume of the electrolyzer stack, along with the inlet and outlet energy flows that form the basis of the energy balance equation. In the following equations, the electrolyte is assumed to be pure water, corresponding to a molarity of zero.

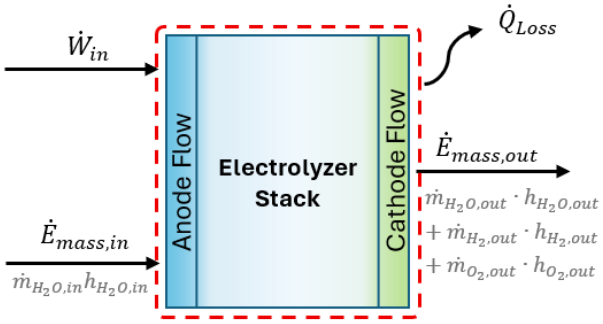

Figure 3.3 Energy balance of electrolyzer stack

In Eq. 3.25, the change in stack temperature over time is governed by the overall thermal capacity (C) and is driven by the electrical power input to the electrolyzer ($\dot{W}_{in}$), the inlet and outlet entalphy flows ($\dot{E}$), and the heat losses to the environment ($\dot{Q}_{Loss}$).

$$C\frac{T_{stack(i)}-T_{stack(i-1)}}{dt} = \dot{W}_{in} + \dot{E}_{Mass,in\ @T_{stack,in}} - \dot{E}_{Mass,out\ @T_{stack}} - \dot{Q}_{Loss\ @T_{stack}} \quad (3.25)$$

Eq. 3.26 calculates the electrical power supplied to the electrolyzer stack ($\dot{W}_{in}$), in watts. It is defined as the product of the stack current (I_{Stack}) and the stack voltage (V_{Stack}), in the units A and V, respectively.

$$\dot{W}_{in} = V_{Stack} I_{Stack} \quad (3.26)$$

The heat loss, represented by $\dot{Q}_{Loss}$ (W), describes the energy dissipated from the stack surface to the ambient environment and calculated as shown in Eq. 3.27.

$$\dot{Q}_{Loss} = h_c A_{Stack,ext}(T_{stack} - T_{amb}) \quad (3.27)$$

where h_c (W/m^2K) is the convective heat transfer coefficient, $A_{Stack,ext}$ (m^2) is the external surface area of the stack, T_{stack} (K) is the stack temperature, and T_{amb} (K) is the ambient temperature.

The energy flows associated with the inlet and outlet mass streams are denoted as $\dot{E}$ and calculated as described in Eqs. 3.28 and 3.29. The inlet stream is defined by the inlet mass flow rate and its enthalpy at the inlet temperature, which corresponds to the temperature of the fluid leaving the electrolyte tank.

$$\dot{E}_{Mass,in} = \dot{m}_{H_2O,in} h_{H_2O,in} \quad (3.28)$$

The outlet streams consist of the produced hydrogen, oxygen, and unconsumed water, all of which leave at the stack temperature.

$$\dot{E}_{Mass,out} = \dot{m}_{H_2O,out} h_{H_2O,out} + \dot{m}_{H_2,out} h_{H_2,out} + \dot{m}_{O_2,out} h_{O_2,out} \quad (3.29)$$

The mass flow rate in Eqs. 3.30 and 3.31 are measured in (kg/s), denoted as $\dot{m}$. The variable h indicates the enthalpy value, which is expressed in (J/kg). These parameters specifically pertain to the substance's H_2O, H_2, and O_2, respectively. It is

assumed that these outlet streams are in thermal equilibrium with the stack, resulting in their temperature being equal to that of the stack. The mass flow rates of the outlet species are calculated based on Faraday's law of electrolysis. The corresponding expressions for water consumption, hydrogen production, and oxygen production are given in Eqs. (3.30-3.32), respectively. Here, $\bar{M}$ represents the molar mass values for each species (kg/mol) and n_f is the Faradaic efficiency, taken as 0.99.

$$\dot{m}_{H_2O,cons} = \frac{I_{Stack}}{2F} \bar{M}_{H_2O} \tag{3.30}$$

$$\dot{m}_{H_2,prod} = \frac{n_f \cdot I_{Stack}}{2F} \bar{M}_{H_2} \tag{3.31}$$

$$\dot{m}_{O_2,prod} = \frac{n_f \cdot I_{Stack}}{4F} \bar{M}_{O_2} \tag{3.32}$$

The inlet water mass flow rate to the stack, $\dot{m}_{H_2O,in}$, is assumed to be constant and 0.05 (kg/s). The water flow rate at the electrolyzer outlet is calculated according to Eq. 3.33 as the difference between the inlet flow and the amount consumed in electrolysis.

$$\dot{m}_{H_2O,out} = \dot{m}_{H_2O,in} - \dot{m}_{H_2O,cons} \tag{3.33}$$

Figure 3.4 illustrates the control volume of the electrolyte tank. The inlet streams consist of make-up water at ambient temperature and the electrolyte recycled from the stack at stack temperature. The outlet stream is assumed to be at the uniform tank temperature, which is then supplied to the electrolyzer.

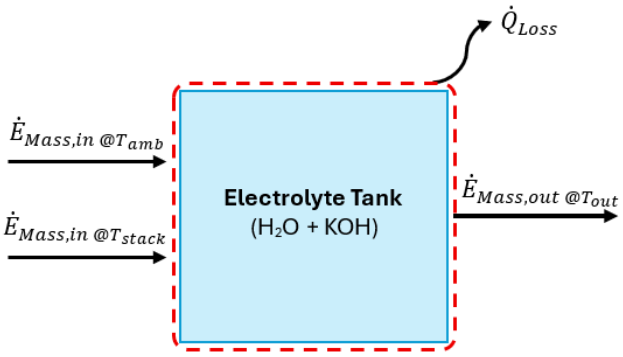

Figure 3.4 Energy balance of electrolyte tank

The inlet energy flows consist of the make-up water supplied at ambient temperature (T_{amb}) and the recirculated electrolyte returning from the stack at stack temperature (T_{stack}). The outlet energy flow is represented by the electrolyte stream leaving the tank at outlet temperature ($T_{tank} = T_{tank,out} = T_{stack,in}$). In addition, thermal losses from the tank to the environment are calculated similarly as shown in Eq. 3.27. The resulting mass and energy balance equations, solved as Eq. 3.34. Here, capacity is determined using the specific heat of the electrolyte tank and the associated tank mass.

$$C\frac{T_{stack(i)}-T_{stack(i-1)}}{dt} = \dot{E}_{Mass,in\ @T_{tank,in}} - \dot{E}_{Mass,out\ @T_{tank,out}} - \dot{Q}_{Loss\ @T_{tank}} \quad (3.34)$$

Here, $\dot{E}_{Mass,in}$ and $\dot{E}_{Mass,out}$ are calculated using Eqs. 3.35 and 3.36, respectively, considering H_2O only.

$$\dot{E}_{Mass,in} = \dot{m}_{H_2O,in} h_{H_2O,in} \quad (3.35)$$

$$\dot{E}_{Mass,out} = \dot{m}_{H_2O,out} h_{H_2O,out} \quad (3.36)$$

This section is followed by the dynamic simulation of the electrolyzer's thermal behavior, and its associated BoP components were developed within the MATLAB/Simulink Simscape environment. The Simulink schematic (Figure 3.5) represents the system architecture, primarily focusing on electrolyte recirculation and thermal interactions between the stack and the tank.

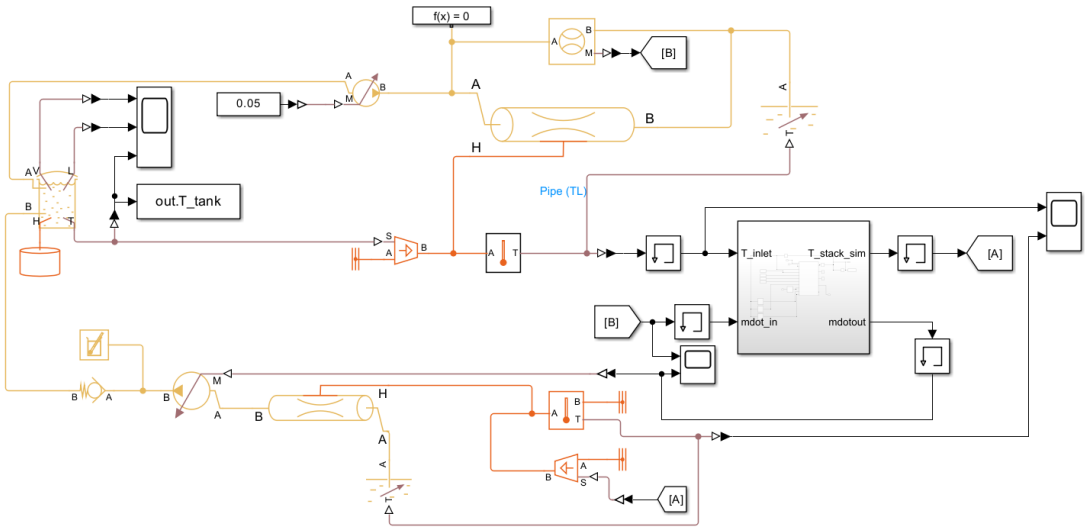

Figure 3.5 Balance of Plant of AEMWE stack in Simulink

Located on the left side of the fluid network, the Thermal Liquid Tank block represents the electrolyte reservoir. The component includes inlet and outlet ports, along with a thermal liquid connection for heat transfer. It functions as a combined thermal and mass storage unit, where the liquid level dynamically varies with the net inflow and outflow. The recirculation loop, established using Thermal Liquid Pipe blocks and control valves, governs the flow of electrolyte between the tank and the stack model. A constant flow rate of mass flow rate is maintained by a valve, and the model includes the necessary piping elements along the flow path. The complex electrochemical and thermal calculations for the electrolyzer stack are calculated within a Subsystem Block. This block receives the electrolyte inlet temperature (T_{inlet}) and mass flow rate ($\dot{m}_{in}$) from the Simscape network and computes the outlet temperature (T_{outlet}) and mass flow rate ($\dot{m}_{out}$) at the stack outlet. Furthermore, MATLAB Function blocks are employed to access accurate, temperature-dependent thermodynamic properties (enthalpies, h, and specific heats, c_p) required for the energy balance calculations, performing linear interpolation over embedded tabulated data.

This integrated Simulink architecture provides a robust platform that simultaneously solves the coupled mass and energy differential equations for both the stack and the electrolyte tank, enabling a comprehensive assessment of dynamic performance. Therefore, the values used in MATLAB and Simulink modeling, given in Table 3.2.

Table 3.2 Parameters for stack and electrolyte tank modeling

Parameter		Value
N_{cell} (—)	Number of Cells	19 (Gladik et al., 2025)
A_{cell} (cm^2)	Cell Area	60 (Gladik et al., 2025)
$\dot{m}_{inlet}$ (kg/s)	Inlet Electrolyte Flow Rate	0.05 (Gladik et al., 2025)
C_{stack} (J/K)	Stack Heat Capacity	100,000
h_c ($W/m^2 \cdot K$)	Heat Transfer Coefficient	10
$A_{ext,\ stack}$ (m^2)	Stack External Dimensions	0.2 x 0.2 x 0.1
$A_{ext,\ tank}$ (m^2)	Tank External Dimensions	0.2 x 0.2 x 0.25
V_{tank} (L)	Tank Volume	10 L
M (—)	KOH Molarity	0

It should be noted that some parameters were taken from the literature (Gladik et al., 2025), whereas others were estimated according to the system's operating conditions. Specifically, the stack thermal capacity (C_{stack}), was assigned a value within the reasonable range of 10-200 kJ/K, consistent with values reported for similar systems. In their study, Espinosa-López et al. (2018) estimated this value as 162 kJ/K in their setup. On the other hand, García-Valverde et al. (2012) obtained a value of 42 kJ/K for their consideration. Agbli et al. (2011), used a value of 21.06 kJ/K for their modeling studies. This value can vary significantly depending on the system configuration, such as the number of cells and the materials used in the stack.

The stack dimensions were assumed based on typical commercial component sizes (*LBE-20C (Alkaline Water Electrolyzer Large Stack - 20 Cell)*, n.d.). The selected constant inlet electrolyte flow rate of 0.05 kg/s was derived from the given volumetric flow density value of 2.5 ml cm^{-2} min^{-1} (Gladik et al., 2025), converted based on the stack's active area. Furthermore, the electrolyte molarity employed in the system was 0.2 M; however, in the modeling, it was simplified to pure water (0 KOH Molarity) under the assumption that the low concentration of KOH would not significantly alter the required thermodynamic properties within the simulated temperature range

3.1.2.2 Integration with Renewable Power and Storage Technologies

The integration of renewable power technologies with water electrolysis systems enables sustainable hydrogen production by directly utilizing intermittent energy sources. This section presents the comprehensive modeling of a PV-AEMWE-MH configuration, specifically designed to investigate the dynamic coupling between fluctuating power generation, instantaneous electrolysis, and controlled hydrogen storage. The model aims to capture the effects of solar power fluctuations on the electrolyzer performance, hydrogen production rate, and the thermal behavior of the MH storage unit.

The system comprises a PV panel that powers a PBI-based AEM electrolyzer, enhanced by a maximum power point tracking (MPPT) unit for improved efficiency. Hydrogen flow is managed through a dual-control strategy, employing a PID controller to regulate flow based on system pressure and an on/off controller to maintain

temperature within operational limits. The system fills switches to the next tank when one reaches its maximum temperature, resuming only after it cools to a safe level, ensuring efficient and safe hydrogen storage. A schematic of the system is shown in Figure 3.6.

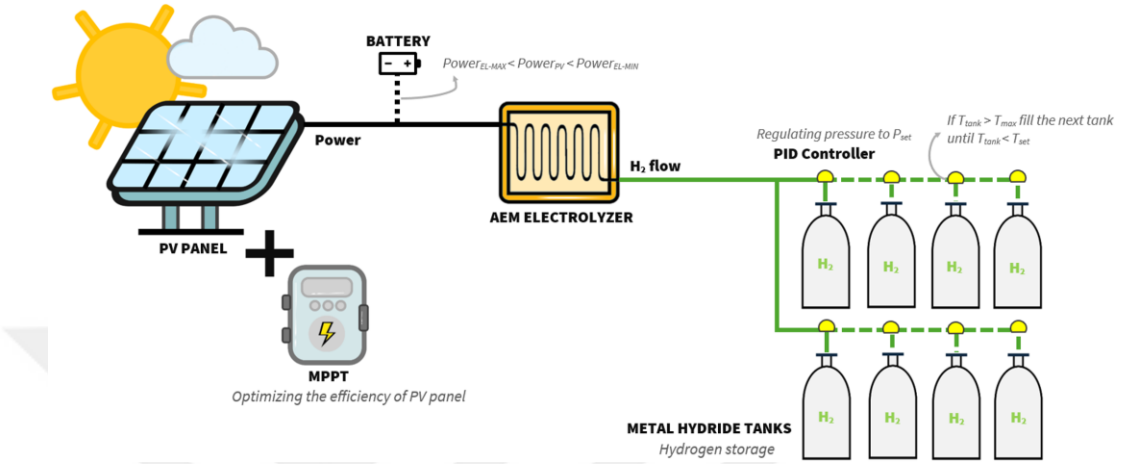

Figure 3.6 System schematic of PV-AEMWE-MH integration

In the proposed system, the solar irradiance and ambient temperature vary continuously, influencing the power output of the PV panel. To ensure optimal operation, an MPPT system is implemented to maintain the PV module at its maximum efficiency. The generated electrical power is directly supplied to the AEM electrolyzer. It is essential to maintain the electrolyzer operation within its minimum and maximum power limits. When the PV output exceeds the maximum allowable input of the electrolyzer, corresponding to a current density of 3.5 A/cm^2, the battery stores the excess energy.

The hydrogen produced in the electrolyzer is directly fed to the MH storage tanks. The hydrogen flow rate varies dynamically with the production rate of the electrolyzer, as determined by the AEMWE model. Both pressure and temperature controllers are implemented for each MH tank. When the temperature of a tank exceeds a defined limit, the hydrogen flow is redirected to the next available tank. Once the tank temperature decreases below the threshold, the filling process resumes. Multiple tanks can also be filled simultaneously, depending on the system conditions.

A PID and on-off control strategy regulates the pressure and temperature within each tank to ensure they do not exceed maximum allowable limits. The hydrogen flow rate and thermal state are continuously adjusted according to the controller outputs, maintaining stable operation, safe pressure levels, and effective thermal management within the storage system.

The PV subsystem was modeled in MATLAB/Simulink-Simscape using the Solar Cell block from the Simscape Electrical library (MathWorks, 2025). The selected module was TrinaSolar Duomax TSM-DEG5-60C-280W, whose electrical characteristics (open-circuit voltage, short-circuit current, series and shunt resistances, and temperature coefficients) were automatically imported from the MATLAB database. The PV block receives solar irradiance and ambient temperature (T_{amb}) as time-dependent inputs, dynamically linked to the environmental data source in the simulation. These inputs determine the I-V and P-V characteristics of the module at each time step. The resulting output current and voltage define the instantaneous electrical power, which is continuously monitored to ensure that the PV operates at its maximum power point (MPP).

To track the MPP under varying irradiance and temperature, an MPPT subsystem was implemented (Figure 3.7).

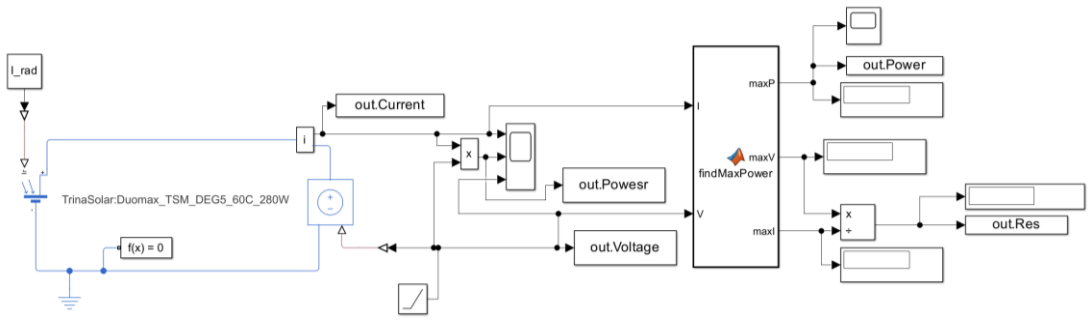

Figure 3.7 MPPT system configuration for PV

The current (I) and voltage (V) signals from the PV module are multiplied to obtain instantaneous power. The findMaxPower MATLAB Function block stores and updates the maximum power, voltage, and current during the simulation using the logic illustrated in the flow diagram (Figure 3.8).

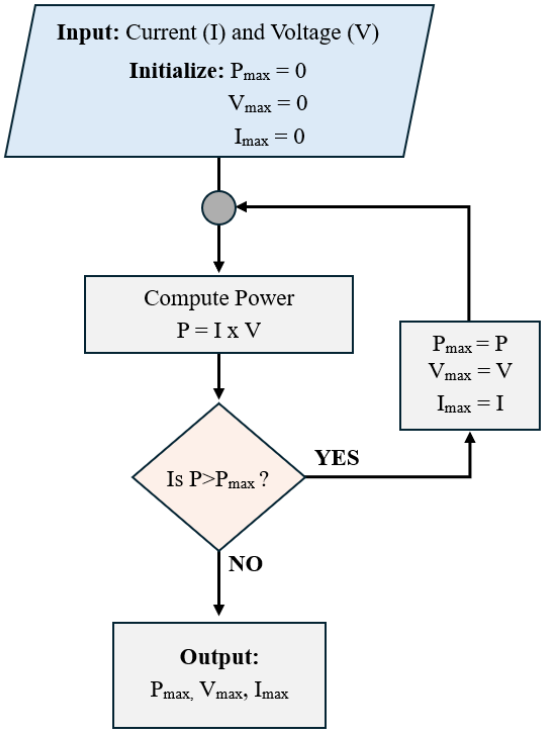

Figure 3.8 Logic of MPPT

The instantaneous equivalent resistance at the maximum power point is calculated according to Ohm's law, as shown in Eq. 3.37.

$$R_{MPP} = \frac{V_{max}}{I_{max}} \tag{3.37}$$

This resistance represents the effective electrical load at which the PV array delivers its maximum output power. In the AEMWE-PV configuration, the calculated resistance (out.Res) is used, ensuring that the electrolyzer operates close to the PV module's MPP under all solar and temperature conditions. Panels are arranged as 3 parallel strings of 4 series-connected modules, using the same TrinaSolar Duomax TSM-DEG5-60C-280W module.

Irradiance and ambient temperature T_{amb} are fed as time-varying inputs (clock-driven profiles). The MPPT routine monitors the PV's current and voltage and computes the corresponding power. The aforementioned PV-load implementation was inspired by the MathWorks Photovoltaic-Thermal (PV-T) Hybrid Solar Panel example (MathWorks, 2025). The optical modeling approach adopted in the reference example

is also included, accounting for reflection, transmission, and absorption losses in the front glass, and the resulting transmitted irradiance is used in the PV power calculations.

The configuration of the PV system integrated with the AEMWE model is illustrated in Figure 3.9.

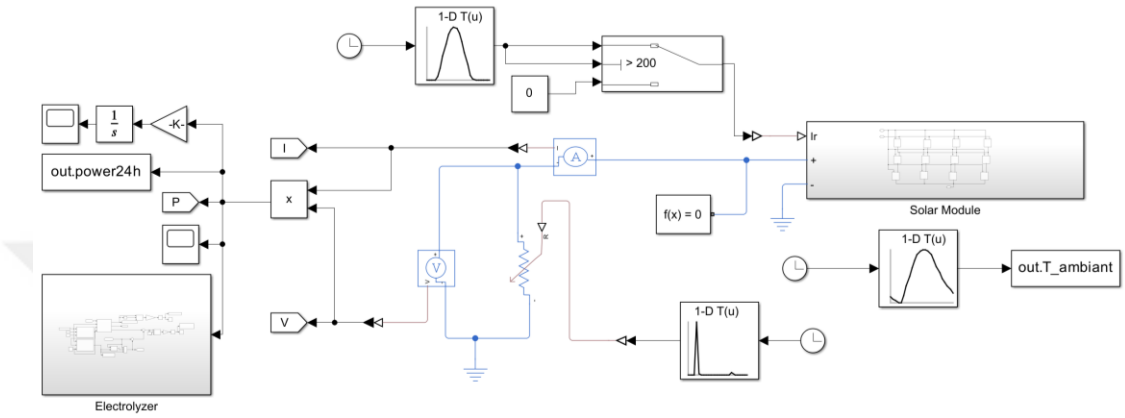

Figure 3.9 AEMWE-PV integration in Simulink

In the PV subsystem, a total of 12 identical photovoltaic modules (TrinaSolar Duomax TSM-DEG5-60C-280W) were used to form the solar power generation unit. The electrolyzer subsystem, as illustrated in Figure 3.10, consists of MATLAB Function blocks developed for the calculation of Nernst Voltage and the electrolyzer polarization curves, both based on the electrochemical model described previously.

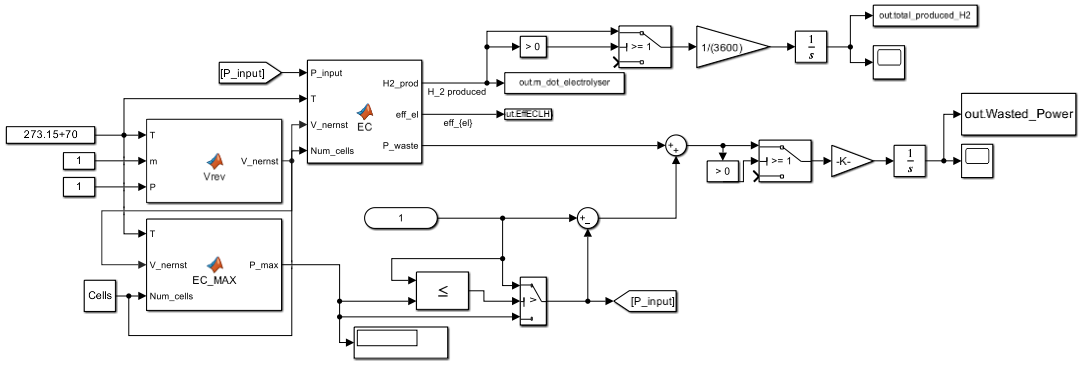

Figure 3.10 Electrolyzer Power Management Subsystem

The activation overpotential is calculated using the Newton-Raphson method, since the fsolve is not supported within the MATLAB Function environment. To enable moderate scaling of the electrolyzer model, the cell active area is set to 25 cm^2, and the stack consists of 10 identical cells. The control strategy ensures that the electrolyzer operates within specified power limits, redirecting any excess power according to the system configuration, thereby enabling safe operation under changing power input conditions.

The generated power from the PV is first checked to see if it remains within the operating range of the electrolyzer. If the value is below the minimum threshold, which is set t 1.5 V, the power is directed to the battery; if it is above the threshold, the maximum power that can be supplied to the electrolyzer is allocated, and the remaining power is sent to the batteries. The battery system is not explicitly modeled, and surplus power is assumed to be stored without limitations. The power supplied to the electrolyzer will be expressed in terms of E_{cell} and I_{cell}, as shown in Eq. 3.38.

$$P(I) = N_{cell} \cdot E_{cell}(I) \cdot I_{cell} \tag{3.38}$$

In the proposed system, the number of cells (N_{cell}) is taken as 10. Due to the limited number of cells in the stack, stack-level performance was assumed to be directly scalable from single-cell results without applying any additional efficiency losses. The E_{cell} value is calculated using the model from the AEMWE model chapter, and $I_{cell}$is found by extracting the corresponding value to E_{cell}. Subsequently, the formula based on Faraday's Law, given in Eq. 3.39, is used to calculate the H_2 in mol/s.

$$\dot{n}_{H_2} = \frac{I_{cell}}{2F} \tag{3.39}$$

The mass flow rate of H_2 in kg/s, produced by the stack, is calculated using Eq. 3.40.

$$\dot{m}_{H_2,electrolyzer} = \dot{n}_{H_2} \cdot M_{H_2} \cdot N_{cell} \tag{3.40}$$

H_2 produced by the electrolyzer stack, is directly sent to the metal hydride storage tanks to absorb hydrogen in its solid form through the exothermic chemical reaction described by Eq. 3.41 (Disli et al., 2024).

$$M + \frac{x}{2} H_2 \leftrightarrow MH_x + Heat \tag{3.41}$$

Before proceeding with the dynamic modeling, the maximum storable hydrogen capacity of a single MH tank (MH_{max}) is calculated, which is then used to determine the total number of required tanks (N_{Tank}) for the system's total production. The maximum hydrogen capacity a single tank can hold (in kg) is calculated based on the difference between the density of the metal hydride in the fully saturated state (ρ_{ss}) and the pure metal state (ρ_s), the volume of the tank (V_{tank}), and the porosity (ε), as shown in Eq. 3.42 (Tong et al., 2019).

$$MH_{max} = (\rho_{ss} - \rho_s) \cdot (V_{tank} \cdot (1 - \varepsilon)) \tag{3.42}$$

The total tank volume (V_{tank}) is determined from the internal geometry of the cylindrical MH tank, with a length of 0.9 m and an inner diameter of 0.02 m. The total number of tanks is then found by dividing the total cumulative produced H_2 in kg, by the maximum capacity of a single tank, calculated using Eq. 3.43.

$$N_{Tank} = \frac{H_{2,total}}{MH_{max}} \tag{3.43}$$

After implementing the required number of tanks in the model, the mass flow rate from the electrolyzer, $\dot{m}_{H_2,electrolyzer}$, is used to dynamically simulate the metal hydride tanks. With the hydrogen gas inside the tanks, the absorption process begins, reducing the gas density in the tank simultaneously. Change in the gas density over time, calculated using H_2 gas coming from the electrolyzer into the free space inside the tank and the rate of absorption process as described by Eq. 3.44 (Tong et al., 2019).

$$\frac{\partial \rho_g}{\partial t} = \frac{\dot{m}_{H_2,electrolyzer}}{V_{tank} \cdot \varepsilon} - \frac{\dot{m}'''_{volume,mh}}{\varepsilon} \tag{3.44}$$

ρ_g represents the gas density, $\dot{m}'''_{volume,mh}$ is the volumetric mass flow rate of the hydrogen during the absorption/desorption process in kg/m^{3}s, and ε is the porosity. $\dot{m}'''$, for the absorption process, calculated using the reaction kinetics (Eq. 3.45) (Tong et al., 2019).

$$\dot{m}''' = C_a \exp\left[-\frac{E_a}{R_{H_2} T}\right] \ln\left(\frac{P_g}{P_{eq}}\right) [\rho_{ss} - \rho_s] \tag{3.45}$$

C_a is the Reaction constant in J/kgK, E_a is the activation energy J/mol and P_{eq} is the equilibrium pressure, for the absorption process. C_a and E_a is dependent on the metal hydride type used in the tank and P_{eq} can be calculated using the Van't Hoff equation as described in Eq. 3.46 (Tong et al., 2019).

$$\ln\left(\frac{P_{eq}}{P_{ref}}\right) = A - \frac{B}{T_{mean}} \tag{3.46}$$

A (–) and B (K^{-1}) are the empirical coefficients depending on the material and P_{ref} represents the reference pressure in bar. Gas pressure in the tank is calculated using Eq. 3.47, according to the Ideal Gas Law.

$$P_g = \rho_g R_{H_2} T_{mean} \tag{3.47}$$

In the equation, the gas constant of hydrogen is in J/kgK and T_{mean} is the mean temperature of the MH bed, in K. The hydrogen absorption process is highly exothermic, meaning it releases significant heat, which directly influences the tank's temperature and pressure dynamics. Eq. 3.48 calculates the effective heat capacity (C_{eff}) and generated heat, $\dot{q}_{gen}$ (W/m^3), is calculated using Eq. 3.49.

$$C_{eff} = \varepsilon\left(\rho_g c_{H_2}\right) + (1-\varepsilon)\cdot(\rho_s c_{metal}) \tag{3.48}$$

$$\dot{q}_{gen} = \dot{m}'''_{volume,mh}\cdot\left[\Delta H + T_{mean}\cdot\left(c_{H_2} - c_{metal}\right)\right] \tag{3.49}$$

The thermal model simplifies the complex coupled transport phenomena by assuming that the hydrogen gas phase within the porous bed is ideally mixed and isothermal in the radial and axial directions. Consequently, the gas density (ρ_g) and pressure (P_g) are treated as lumped parameters, uniform across all nodes (Nasrallah and Jemni, 1997). Therefore, the ρ_g used in the effective heat capacity (C_{eff}) remains uniform, while the solid density (ρ_s) is evaluated locally across the 2D domain to accurately capture the local absorption process driven by local temperature values. Finally, to determine the transient temperature profile T(t), the energy conservation equation is applied. Since the temperature directly affects the equilibrium pressure (P_{eq}) and consequently the reaction kinetics, it's crucial to capture effectively. The

model employs a Finite Difference Method (FDM) in two dimensions to calculate the rate of temperature change, accounting for each direction, as shown in Eq. 3.50.

$$\frac{dT}{dt} = \frac{\sum Q_{tranfer}}{C_{eff} V} + \frac{\dot{q}_{gen}}{C_{eff}} \tag{3.50}$$

Here, $\frac{dT}{dt}$ is the rate of temperature change at a specific node in (K/s), $\sum Q_{tranfer}$ is the net heat transfer rate from the node, considering conduction and convection in Watts, and V is the volume of the node in m^3. The total convective cooling rate from the metal hydride tank was calculated by considering heat transfer from both the cylindrical side surface and the top surface, as given by Eqs. 3.51 and 3.52.

$$\dot{Q}_{side} = h_c \, A_{side} \, (T_{tank} - T_{amb}) \tag{3.51}$$

$$\dot{Q}_{top} = U_{top} \, A_{top} \, (T_{tank} - T_{amb}) \tag{3.52}$$

Where h_c is the convection heat transfer coefficient ($W/m^2 \cdot K$), T_{tank} is the local tank temperature of the node (K), and T_{amb} is the ambient temperature (K). The side surface area, A_{side}, is obtained from the tank circumference and the axial height of each control volume, while the top surface area (A_{top}) is evaluated as the annular area of the corresponding radial element. Side heat transfer is modeled by convection, whereas top heat transfer includes both conduction and convection effects. Therefore, U_{top}, accounts for both conduction through the solid layer and convection to the ambient.

Regarding the boundary conditions, the side and top surfaces are modeled with convection and combined heat transfer, respectively, as defined in Eqs. 3.51 and 3.52. The bottom surface of the metal hydride tank is assumed to be adiabatic, implying that the tank is placed on a well-insulated base and heat loss from the bottom is negligible compared to the other surfaces. Figure 3.11 shows the Simulink model of the metal hydride hydrogen storage tank.

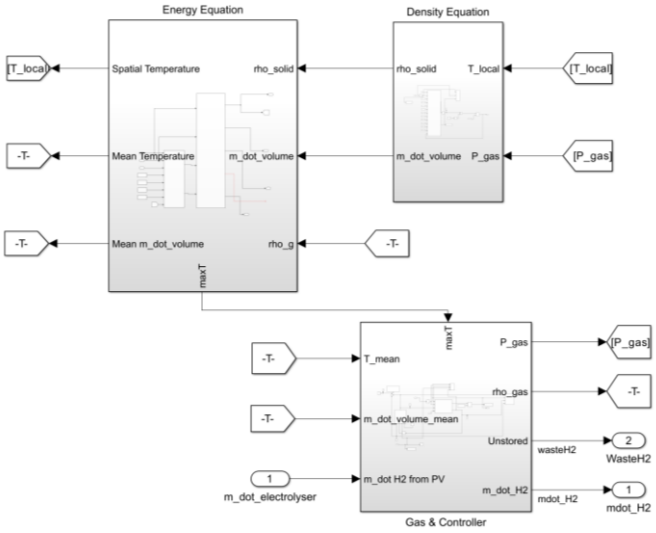

Figure 3.11 Simulink architecture of the integrated metal hydride tank coupled with the electrolyzer hydrogen supply system

The system consists of three main components, based on the previously presented equations: the Energy Equation block for temperature evolution, the Density Equation block representing absorption reaction kinetics, and the Gas & Controller block, which is responsible for integrating hydrogen supplied from the electrolyzer and regulating temperature and pressure. The interconnected structure allows the simulation of the coupled interactions among temperature, pressure, and hydrogen absorption/desorption rates.

All relevant physical and kinetic parameters for $LaNi_5$, the metal hydride material utilized in the dynamic and thermal models of the storage tank, are presented in Table 3.3 (Tong et al., 2019).

Table 3.3 Thermophysical and kinetic properties of $LaNi_5$-based MH (Tong et al., 2019)

Parameter	Values	Parameter	Values
ε [–]	0.5	E_a [J/mol]	21179.6
ρ_s [kg/m^3]	7164	E_d [J/mol]	16473
ρ_{ss} [kg/m^3]	7259	C_a [1/s]	59.187
h_f [W/m^2·K]	1652	C_d [1/s]	9.57
K [m^2]	10^{-8}	c_p [J/kg·K]	14890
T_f [K]	293	c_s [J/g·K]	419
ΔH_a [J/kg]	1.537e7	k_s [W/m·K]	2.4
p_{ref} [bar]	1	k_g [W/m·K]	0.1815
A_a [-]	10.7	R [J/mol·K]	8.314
B_a [1/K]	3704.6	M_{H_2} [kg/mol]	2.0159e–3

Validation of the MH model was based on the parameters reported in Table 3.3. In the present system-level modeling approach, the kinetic parameters were preserved as reported, while system-specific initial and ambient conditions were adjusted according to the selected scenarios. Initially, the system is assumed to be at equilibrium; therefore, the initial gas pressure (P_{gas}) is set equal to the equilibrium pressure (P_{eq}) evaluated at the ambient temperature (T_{amb}). Based on these pressure and temperature conditions, the initial gas density (ρ_{gas}) is calculated. During the simulation, variations in ambient temperature change the P_{eq}, causing it to evolve over time and potentially driving hydrogen absorption in the metal hydride bed when the gas pressure exceeds the equilibrium level.

The MH system was simulated in Simulink using a variable-step Bogacki-Shampine solver (ode23). A maximum step size of 0.1 s and strict error tolerances (relative and absolute tolerances of 10^{-4}) were applied to ensure numerical stability during rapid transients caused by the strongly nonlinear metal hydride absorption behavior.

CHAPTER FOUR
RESULTS AND DISCUSSION

4.1 Performance of AEMWE Based on PBI Membrane

To validate the accuracy of the models, the computed polarization curves were compared against the experimental results reported by Hager et al. (2023). The authors tested a single-cell PBI-based membrane electrolyzer with a 5 cm^2 active area at 70°C and 1 atm, using a 1 M KOH solution with a flow rate of 30 ml/min. At the anode, a NiFe-LDH was used, while a Pt/C was employed at the cathode. The catalyst loadings were 2.0 and 0.5 mg cm^{-2} for the anode and cathode, respectively.

Table 4.1 presents the Tafel slopes and exchange current densities of Pt/C and NiFe-LDH obtained from the literature. In addition, H. Wang et al. (2022) and Dionigi & Strasser (2016) have reported datasets and discussions regarding the performance of NiFe-LDH in their respective studies.The Tafel values for NiFe-LDH typically range between 30-70 mV dec^{-1}, while for Pt/C, they are generally in the range of 20-60 mV dec^{-1}.

Table 4.1 HER and OER characteristics

Catalyst	Solution	Evolution Reaction	Tafel Slope (mV dec^{-1})	Exchange Current Density (mA cm^{-2})
0.8 GO-FeNi-LDH (X. Han et al., 2019)	1 M KOH	OER	33	-
NiFe-LDH (G. Chen et al., 2018)*	1 M KOH	OER	36.2	-
NiFeRu-LDH (G. Chen et al., 2018)*	1 M KOH	OER	32.4	-
NiFeRu-LDH (G. Chen et al., 2018)	1 M KOH	HER	31	0.98
NiFe-LDHs (H. Li et al., 2023)	1 M KOH	OER	65.61	0.901
NiFe-LDHs (H. Li et al., 2019)	1 M KOH	OER	47.76	1.33
NiFeW1-LDHs (H. Li et al., 2023)	1 M KOH	OER	49.55	1.22
Pt/C (T. Wang et al., 2016)	1 M KOH	HER	28	0.82
Pt/C (J. Zhang et al., 2016)	1 M KOH	HER	32	-
Pt/C (M. J. Liu et al., 2023)	1 M KOH**	HER	44	0.97
Pt/C (C. Li & Baek, 2020; Mahmood et al., 2017)	1 M KOH**	HER	43	-

Table 4.1 (Continued)

Catalyst	Solution	Evolution Reaction	Tafel Slope (mV dec^{-1})	Exchange Current Density (mA cm^{-2})
Pt/C (C. Li & Baek, 2020; Y. Liu et al., 2018)	1 M KOH**	HER	37	-
Pt/C (G. Chen et al., 2018)	1 M KOH	HER	32	-
Pt/C (B. Liu et al., 2018)	1 M KOH	HER	45	0.982
Pt/C (Sirisomboonchai, 2020)	1 M KOH	HER	30	-
Pt/C (Wu et al., 2023)	1 M KOH	HER	23	1.31
Pt/C (L. Li et al., 2020)	1 M KOH	HER	38	0.25
Pt/C (B. Lu et al., 2024)	1 M KOH	HER	25.1	-
Pt/C (X. Han et al., 2019)	1 M KOH	HER	32	-
Pt/C (Zhou et al., 2023)	1 M KOH	HER	30	-
Pt/C (Luan et al., 2024)	1 M KOH	HER	38	-
Pt/C (R. Yu et al., 2023)	1 M KOH	HER	38	-
Pt/C (Jiang et al., 2024)	1 M KOH	HER	41	-
Pt/C (Xing et al., 2023)	1 M KOH	HER	45	1.31
Pt/C (R. Tang et al., 2024)	1 M KOH	HER	47	-
Pt/C (Zhan et al., 2024)	1 M KOH	HER	23	-

* Supporting Information, ** (N_2-saturated)

In the experimental setup presented by Hager et al. (2023), the post-treatment Pt loading values of the electrodes were elevated but not considered high enough to surpass the optimal value, supporting the assumption that this increased catalyst activity, consistent with the findings in the literature (Babic et al., 2019; Kriston et al., 2013; X. Liu et al., 2023; Tan et al., 2024). Additionally, the majority of the commercial Pt/C data available in the literature are usually presented for 20 wt% and 40 wt% compositions, which have lower activity compared to commercial 60 wt% Pt/C (X. Liu et al., 2023). Based on the aforementioned, the low Tafel and high current density values, which demonstrate high activity, were considered for evaluating the Pt/C and NiFe-LDH materials. Consequently, 1.31 and 1.22 mA/cm^2 values were selected for the anode and cathode, respectively.

To validate the model, all calculations were performed using the values provided in Table 4.2. In addition to these parameters, the resistance value used for validation was

derived from the high-frequency resistance (HFR)-current density graph of the membrane reported by the authors Hager et al. (2023), with an average value of approximately 84.4 $m\Omega \cdot cm^2$.

Table 4.2 Parameters used in the modeling

Parameter		**Values**
P (bar)	Operating Pressure	1.01325 (Hager et al., 2023)
T (K)	Operating Temperature	343.15 (Hager et al., 2023)
M (-)	Solution (KOH) Molarity	1 (Hager et al., 2023)
b_a (mV/dec)	Tafel slope for anode	49.55 (H. Li et al., 2023)
b_c (mV/dec)	Tafel slope for cathode	23 (Wu et al., 2023)
$i_{0,a}$ (mA/cm^2)	Exchange current density for the anode	1.22 (H. Li et al., 2023)
$i_{0,c}$ (mA/cm^2)	Exchange current density for the cathode	1.31 (Wu et al., 2023)
A (cm^2)	Active cell area	5 (Hager et al., 2023)
d_{am} (m)	Distance between the anode and the membrane	0.0000075
d_{cm} (m)	Distance between the cathode and the membrane	0.0000075
S_a (m^2)	Cross-sectional surface area of the anode	0.0025 (Hager et al., 2023)
S_c (m^2)	Cross-sectional surface areas of the cathode	0.0025 (Hager et al., 2023)

The Nernst voltage is calculated based on temperature, pressure, and molarity, as shown in Figure 4.1. In Figure 4.1a, which presents results at a molarity of 1 M, the influence of pressure and temperature on the Nernst voltage is illustrated. As pressure increases, the overvoltage rises, demonstrating the adverse effect of higher pressure on the system. In contrast, an increase in temperature results in a noticeable decline in overpotential, highlighting the beneficial impact of elevated temperatures on the electrochemical performance. Figure 4.1b illustrates the effects of molarity and temperature on the Nernst voltage at a pressure of 1 bar. Comparable to the effect of pressure, increasing molarity also leads to an increase in the reversible cell voltage.

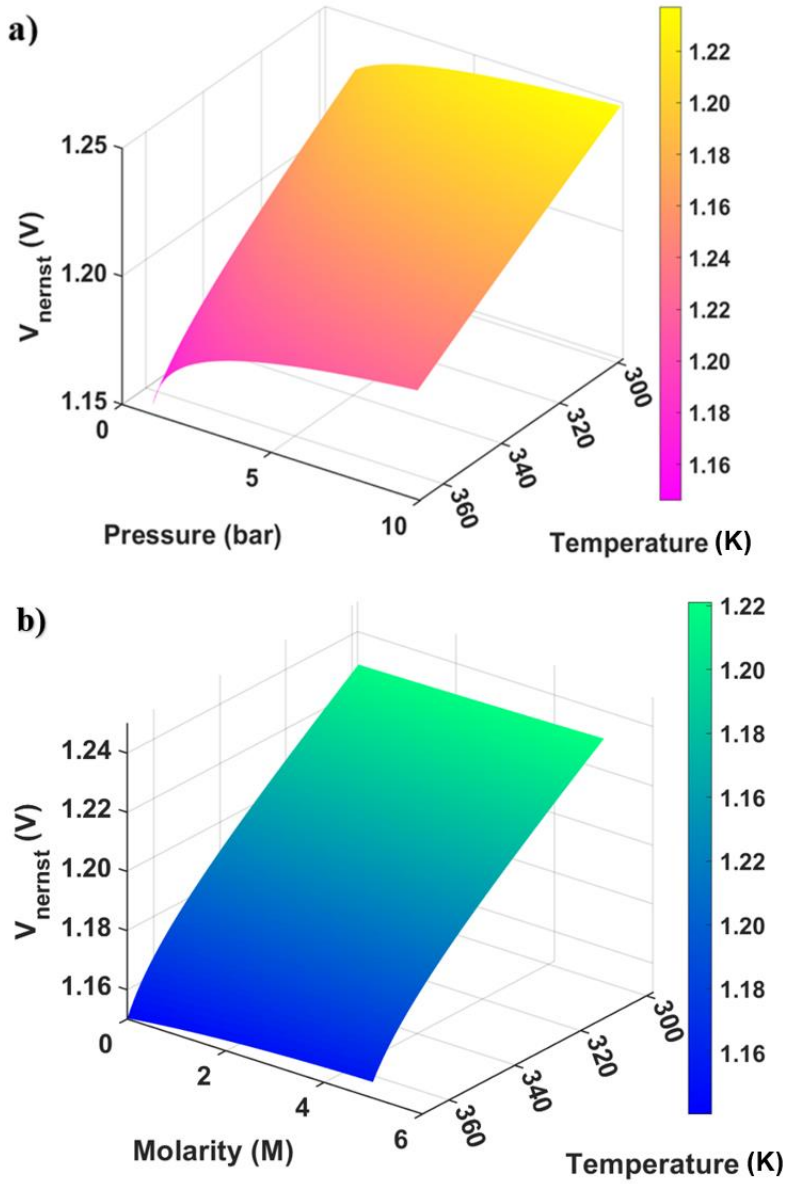

Figure 4.1 Variation of Nernst voltage with temperature and a) pressure and b) molarity, highlighting the combined effects of these parameters

Figure 4.2 illustrates the correlation between cell voltage and current density for both model and experimental data, considering IR-corrected cell voltage. In the model, the IR-corrected cell voltage was determined without considering the impact of membrane resistance. The overpotential observed at low current densities can be attributed to activation loss. As the current density increases, the effects of bubble formation and solution-induced overvoltage become more prominent. The model closely aligns with the experimental trend at lower and higher current densities.

However, between 5,000 and 10,000 A/m², both cell voltage and IR-corrected voltage exhibit higher deviations, with the model yielding higher voltage values than the experimental data. This disparity can be attributed to the selection of electrode values and treatments, such as ionomer usage.

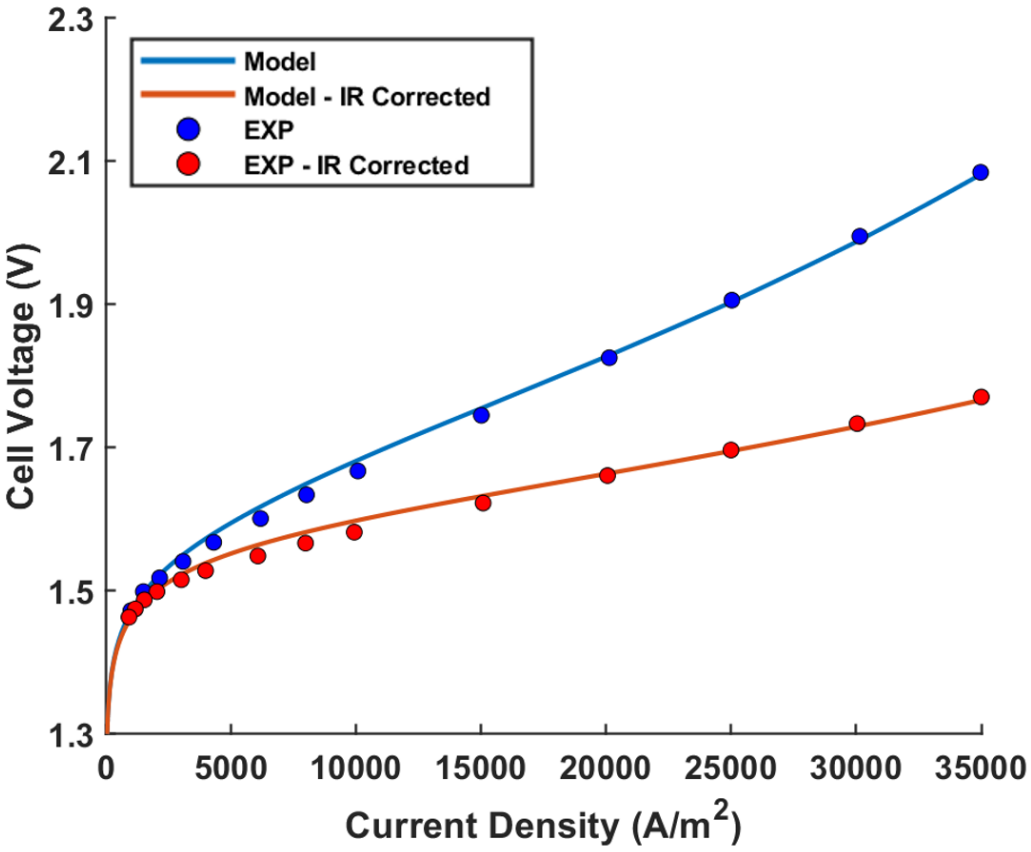

Figure 4.2 Comparison of model results with experimental data (Hager et al., 2023), depicting cell voltage and IR-corrected cell voltage versus current density

In addition to analyzing the voltage-current density curves, absolute and squared error values between the model and experimental data were calculated to measure the accuracy of the model, with results shown in Figure 4.3. These error measurements provide a more objective measure of how well the model agrees with the experimental results. While the absolute error (Figure 4.3a) represents the direct difference between the model and experimental voltage values at each current density, the squared error (Figure 4.3b) emphasizes the error by magnifying the effects of inconsistencies at larger deviations. According to the error analysis result, deviation peaks in the range of 6,000-10,000 A/m^2, as determined from the Cell Voltage curves. The maximum

absolute error was determined in the cell voltage at a current density of approximately 6180 A/m², with a value calculated as 0.016. The squared error is particularly useful for identifying points where the model needs further improvement.

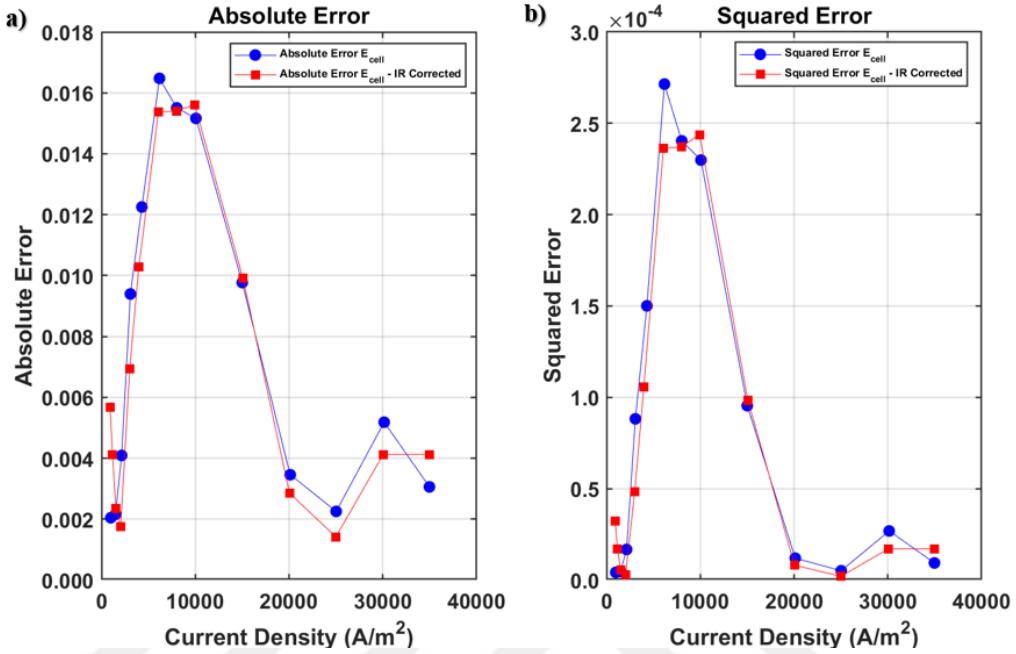

Figure 4.3 a) Absolute and b) Squared error between model results and experimental data (Hager et al., 2023)

Figure 4.4 illustrates the impact of various overpotential values on the cell voltage. The reversible cell voltage is calculated as 1.176 V. As expected, bubble and KOH effects have no observable effects at low current densities. However, these effects become increasingly noticeable with the rising current density. The cell voltage of the electrolyzer is primarily governed by the activation overpotential. This is followed by the ohmic overpotential, which increases as the current density rises. At 20,000 A/m^2 current density, activation overpotential, ohmic overpotential, and overpotentials due to bubble and KOH are calculated as 0.435, 0.154, 0.03, and 0.022 V, respectively.

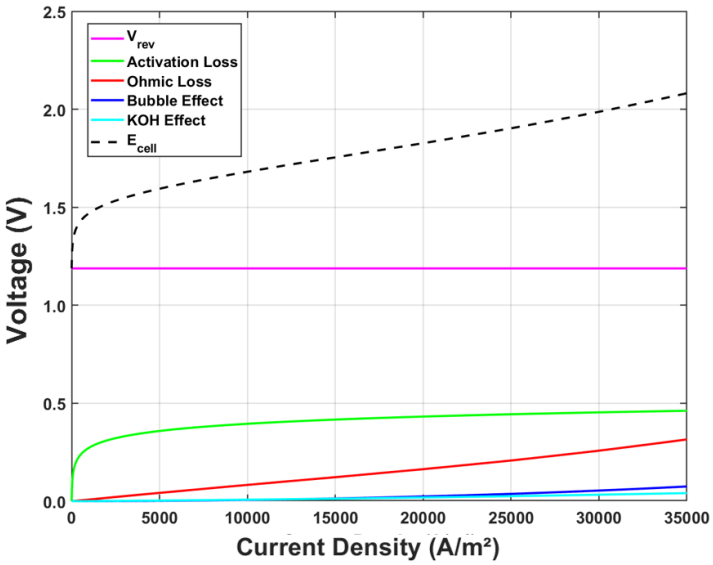

Figure 4.4 Variation of overpotential contributions and resulting cell voltage relative to current density

To provide a clearer understanding of the operating characteristics of PBI-based membranes within an AEM electrolyzer, a comprehensive evaluation was carried out to correlate their material properties with electrochemical performance. The main objective of this section is to investigate how variations in hydroxide conductivity, considering different operating temperatures, influence the overall ohmic overpotential and, consequently, the I-V performance of the cell under alkaline conditions. Table 4.3 presents the OH^- conductivities, IEC values, thickness ranges, resistances, solution types, molarities, and temperatures for various PBI-based membranes reported in the literature.

Table 4.3 Electrochemical and physical properties of PBI-based membranes

Membrane	**OH^- Conductivity (mS cm^{-1})**	**IEC (mmol/g)**	**Thickness (µm)**	**Membrane Ohmic Resistance (Ω cm^2)**	**Solution**	**Temperature (°C)**
PBI (Coppola et al., 2020)	48	1.97	–	–	1 M KOH	50
PBI (S. Li et al., 2018)	110	1.36	10	–	1 M NaOH	80
Sulfonated PBI (Kulkarni et al., 2012)	40.1	4.1	–	–	1 M KOH	80
PMPBI (Sana et al., 2019)	29	1.71	20-30	–	0.5 M KOH	50

Table 4.3 (Continued)

Membrane	OH- Conductivity (mS cm^{-1})	IEC (mmol/g)	Thickness (µm)	Membrane Ohmic Resistance (Ω cm^2)	Solution	Temperature (°C)
PBI Composite Membrane (J. Y. Lee et al., 2016)	6.6	1.06	–	–	1 M KOH	50
Ionic PBI (Abdi et al., 2021)	86	2.55	10-40	–	1 M NaOH	80
PBI Blend Membrane (Morandi et al., 2015)	40	3.7	–	–	1 M KOH	60
Quaternized PBI (Jheng et al., 2014)	27.2	1.49	–	–	1 M KOH	80
PBI/Polystyrene (Hager et al., 2023)	30	2.2	50	–	1 M KOH	40
Nanofiber Reinforced PBI (Najibah et al., 2021)	62	1.7	50	–	1 M KOH	50
PBI (W. Tang et al., 2021)	29.8	1.9	60	0.43	1 M KOH	80

The area-specific resistance for the PBI/Polystyrene membrane with ionomer was digitized from the published graph, while for the remaining membranes, it was calculated using Eq. 4.1 based on conductivity.

$$R_{mem} = \frac{t_{AEM}}{\sigma_{mem}} \tag{4.1}$$

t_{AEM} represents the thickness of the membrane and is taken as 50 µm. With the assumption that all experiments were conducted under identical conditions, including electrode treatments, temperature, and solution, cell voltages were calculated using the conductivity values of different membranes.

Comparative graphs showcasing these results are provided in Figure 4.5. The abbreviations presented in the Figure refer to different AEM formulations, all of which are based on polybenzimidazole (PBI) membranes. These include PBI derivatives such as ABPBI and OPBI, their quaternary forms, chloromethylated poly(vinylbenzyl chloride) (c-PVBC) mixtures prepared at various ratios (e.g., 1:2 or 1:3), and piperazine-styrene copolymers such as P4HexPipSt.

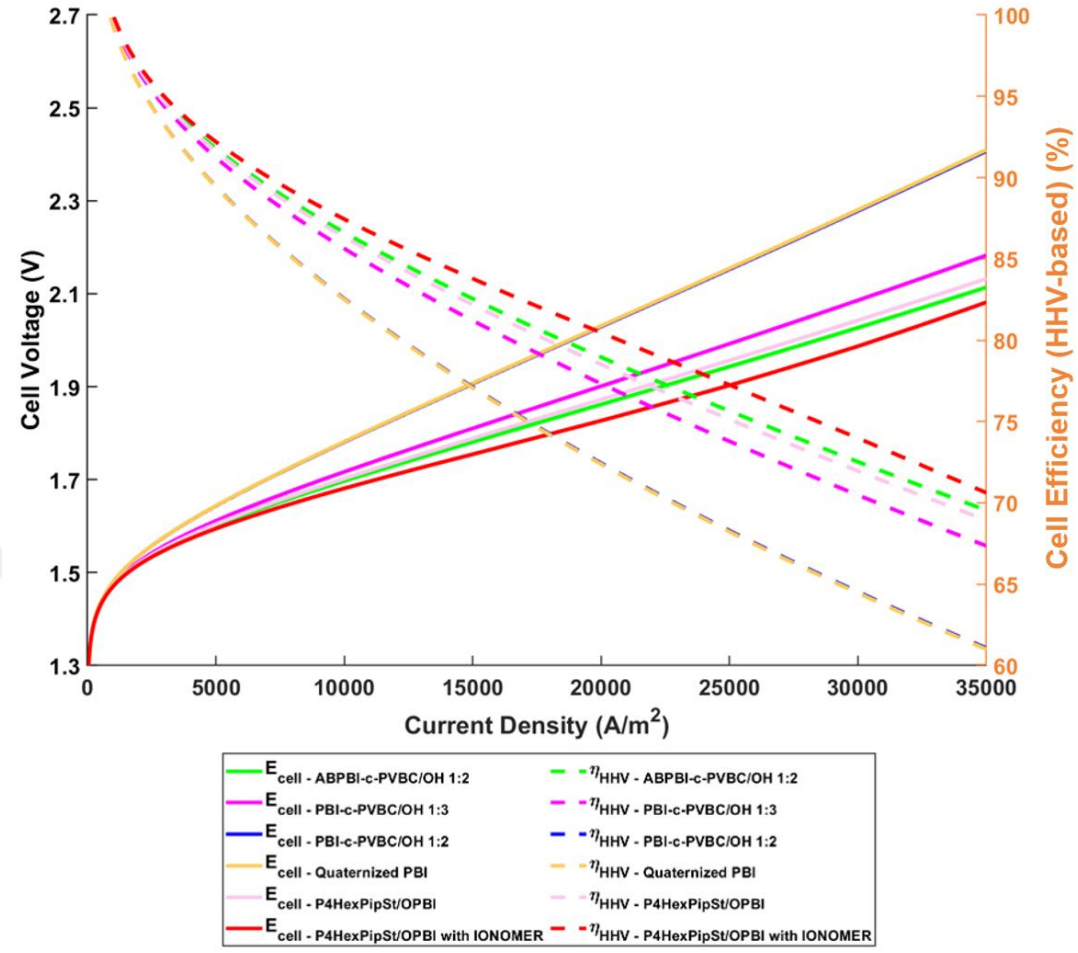

Figure 4.5 Cell voltage and HHV Efficiency for different PBI-based membranes

Among the PBI-based membranes listed in Table 4.3, those with conductivity values reported under similar experimental operating conditions, i.e., 1 M KOH and 70°C, can be found in references (Coppola et al., 2020; Hager et al., 2023; Jheng et al., 2014). The graph illustrates that the PBI/Polystyrene - P4HexPipSt/OPBI membrane with ionomer addition exhibited the most optimal performance, with an HHV efficiency of approximately 80% at a current density of 20,000 A/m^2. This efficiency is notably high, particularly at such elevated current densities. It should be noted that the ionomer significantly affects this membrane's performance; without the ionomer, its conductivity decreases from approximately 60 mS/cm to 47.6 mS/cm. This makes the ABPBI-c-PVBC/OH 1:2 membrane the highest performing among them, with a conductivity value of 50.35 S/m. Without ionomer content, the highest efficiency value was obtained around 78.5% at 20,000 A/m^2, which is still quite high. ABPBI-c-

PVBC/OH 1:2, PBI-c-PVBC/OH 1:3, and PBI-c-PVBC/OH 1:2 membranes showed different performances with conductivity values of 50.35, 42, and 27.3 mS/cm, respectively. ABPBI-c-PVBC/OH 1:2 has the highest performance among all in terms of conductivity, while PBI-c-PVBC/OH 1:2 was the least favorable membrane, along with Quaternized PBI. Quaternized PBI has a 0.1 mS/cm lower conductivity value with 27.2 mS/cm compared to PBI-c-PVBC/OH 1:2, and their performance was quite similar to each other; both performed the same efficiency value of 72% at 20,000 A/m^2. It should be noted that the ionomer effect is assumed to be effective only in the ohmic potential calculation due to increased conductivity; therefore, it is not considered when calculating other overpotentials, such as activation overpotential.

To assess the impact of temperature, the conductivity values of the PBI/Polystyrene membrane without ionomer were adjusted, and the corresponding cell voltage values were calculated as shown in Figure 4.6a. The charge transfer coefficients varied with temperature due to the Tafel slope, while the exchange current density remained constant. As a result, only a minimal temperature-dependent change was observed in the IR-corrected curves. However, in practice, this difference is likely to increase as the exchange current density changes. As the activity increases with rising temperature, the exchange current density also increases. Therefore, it can be concluded that variations in temperature will have a more significant impact on the cell voltage. The temperature varied from 40°C to 80°C; as expected, the best performance was obtained at high temperatures. The impact of temperature on performance is more pronounced at lower operating temperatures. The impact of thickness on cell voltage and efficiency at 80°C is illustrated in Figure 4.6b. An increase in membrane thickness results in higher ohmic overpotential, which has a detrimental impact on efficiency. At a current density of 20,000 A/m^2, the efficiencies obtained were approximately 83.89%, 79.83%, and 76.15% for thicknesses of 25, 50, and 75 µm, respectively. Decreasing the thickness from 50 to 25 µm caused an increase of approximately 4.07% in efficiency, and increasing it to 75 µm caused a decrease of 3.68%. The calculated difference at 35,000 A/m^2 current density is 5.72% and 4.93%, respectively. With the increasing current density, variations in both temperature and membrane thickness have a higher impact on efficiency.

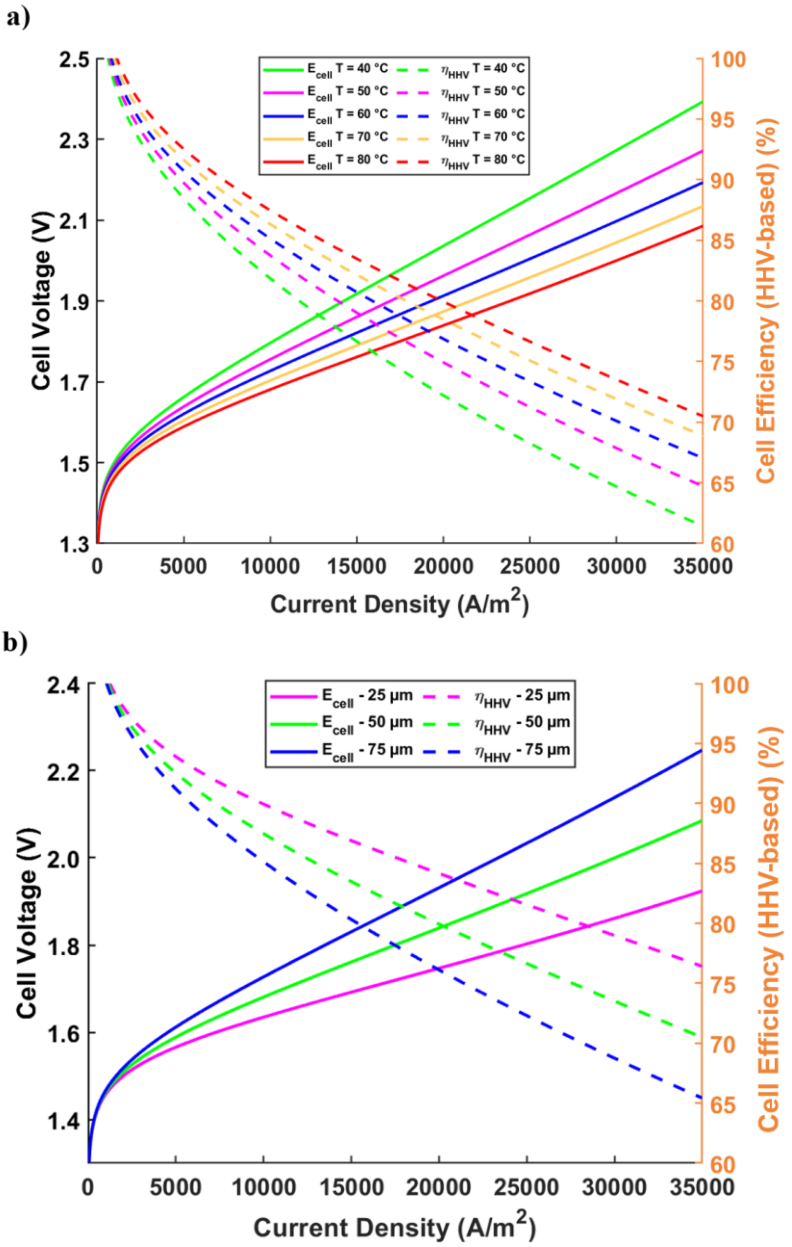

Figure 4.6 Cell voltage and efficiency for varying a) temperatures, b) membrane thicknesses using P4HexPipSt/OPBI membrane

Figure 4.7 presents the model results for ABPBI-c-PVBC/OH 1:2 Membrane, showing the effect of temperature and thickness on the voltage and efficiency. This membrane demonstrated a similar but slightly improved performance compared to the PBI/Polystyrene membrane at 70°C, as seen in

Figure 4.5 previously. The conductivity values are taken from the study by Coppola et al. (2020), where the values were measured from 40°C to 90°C (except 60°C) in

10°C increments. Similarly, Figure 4.7a highlights the efficiency increase observed with rising temperature. The positive impact of decreasing membrane thickness can be seen in Figure 4.7b, where an efficiency of 83.86% is observed for a 25 µm membrane at 90°C and a current density of 20,000 A/m².

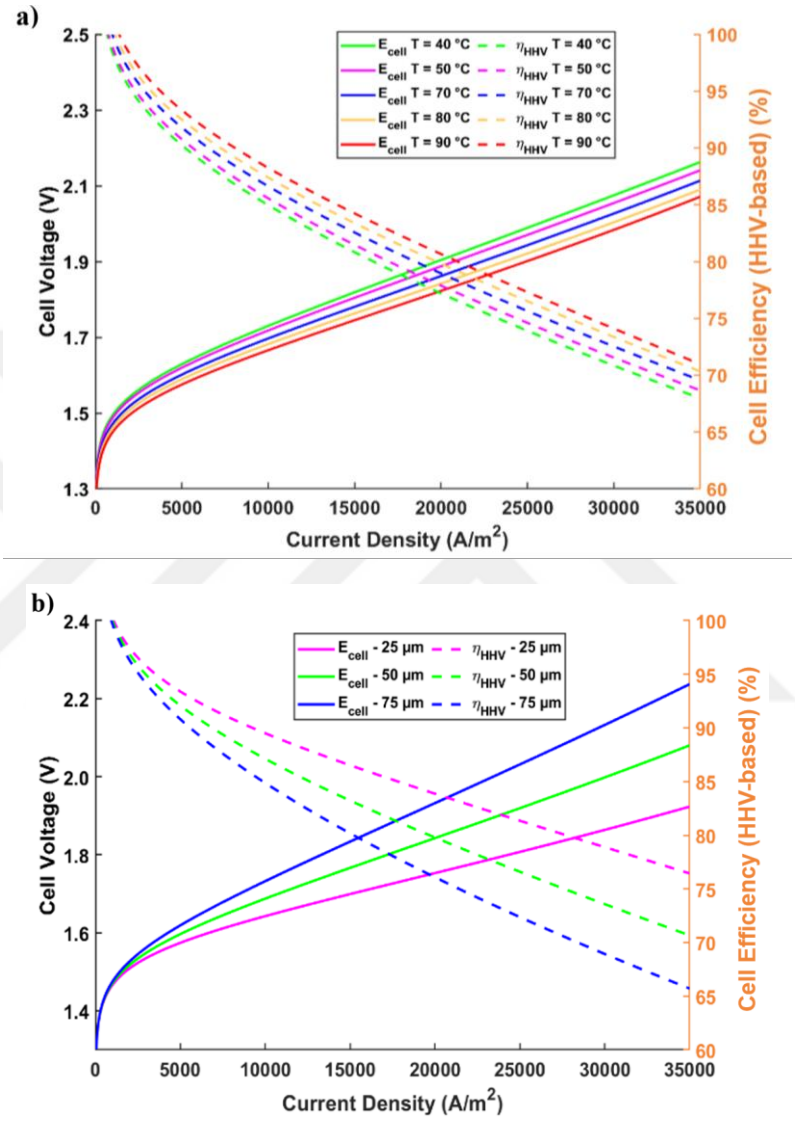

Figure 4.7 Cell voltage and efficiency for varying a) temperatures, b) membrane thicknesses using ABPBI-c-PVBC/OH 1:2 membrane

In the AEMWE system, it is essential to evaluate these values collectively rather than independently, as changes in one parameter can influence others. Comparing Figure 4.6a and Figure 4.7a reveals the varied responses of different membrane structures to temperature variations. The conductivity values of the ABPBI-c-PVBC/OH 1:2 membrane, which exhibited less sensitivity to temperature changes,

showed minimal variation across the measured range. Although the ABPBI-c-PVBC/OH 1:2 membrane provided higher efficiency at 70°C compared to the P4HexPipSt/OPBI membrane, it was surpassed at elevated temperatures. For 50 μm membranes, the P4HexPipSt/OPBI membrane achieved an efficiency of 79.83% at 80°C, whereas the ABPBI-c-PVBC/OH 1:2 membrane showed a slightly lower efficiency of 79.79% at 90°C, despite the 10°C temperature difference. However, when comparing the membranes at 40°C, the P4HexPipSt/OPBI membrane exhibited an efficiency of 72.20%, whereas the ABPBI-c-PVBC/OH 1:2 membrane demonstrated a higher efficiency of 78.56%. Due to the higher conductivity of the ABPBI-c-PVBC/OH 1:2 membrane at lower temperatures, it achieved approximately 6.36% higher efficiency at 40°C than the P4HexPipSt/OPBI membrane. It should be noted that the membrane's mechanical properties were not considered when varying the membrane thicknesses in these analyses. The graphs provided are intended to offer insights into the effects of thickness on performance, serving as an initial evaluation.

This study explores the challenges of modeling AEMWEs and the factors affecting their operating characteristics. A 0-D mathematical model was then developed that incorporates main overpotentials such as ohmic and activation resistances, as well as bubble formation and electrolyte resistance, which affect electrolyzer efficiency. Carefully selected values were utilized in the model based on the material properties. The performance of PBI-based membranes was then compared using the proposed model. A key contribution of this study is the validation using IR-corrected curves, which clearly demonstrate how cell performance is affected by membrane conductivity. This methodology provides a clear understanding of the effect of conductivity on electrolyzer efficiency, enabling reliable evaluation of different membranes. Another aspect of this study is the comparison of membranes with and without ionomer addition, highlighting their critical impact on performance. Error analysis methods were then applied to assess the model's accuracy, highlighting both its strengths and areas for improvement. Through a comparative analysis of PBI membranes and their operational behavior, this study aims to provide a better understanding of their performance in AEMWEs and support the development of PBI-based technologies for sustainable hydrogen production.

However, it should be noted that the model is based on experimental data from the literature, which is limited to specific operating conditions. While PBI membrane conductivity data are available at various temperatures, the AEMWE experimental data used in validation was limited to a single temperature, making it difficult to verify electrode performance under varying conditions. Similarly, the model is based on a single molar concentration, and deviations from this value can significantly alter the results, limiting the model's generalizability. However, the use of IR-corrected validation is a crucial distinction, as it allows for accurate isolation of the effect of membrane resistance on cell performance. This provides confidence in understanding how membrane performance affects AEMWE systems, allowing for a reliable comparison of PBI membranes. Although the 0-D model introduces simplifications by neglecting dimensional effects, such as temperature gradients, it is sufficient due to its computational efficiency and effectiveness in identifying performance trends.

4.2 Performance of AEMWE System

Following the validation of the core cell model, the subsequent subsections present the transient simulation results, first focusing on the thermal dynamics of the AEMWE stack and the electrolyte recirculation system. The analysis then continues with the assessment of the fully integrated system's response to fluctuating solar irradiance and ambient temperature. Crucially, to observe the pivotal role of thermal management in storage performance, varying heat transfer coefficients (h_c) are examined, and their effects on storage dynamics are analyzed in detail.

4.2.1 Simulation of AEMWE including Balance of Plant Components

In this section, the interaction between the stack and the electrolyte tank during startup was examined, along with the influence of both modeling and operational parameters representative of real setups, and the corresponding results were presented. The startup profile was based on Gladik et al. (2025)’s study and accordingly, the current density and voltage values used in the study are presented in Figure 4.8, which illustrates the time-dependent cell voltage and current density (Figure 4.8a) and the corresponding V-I curve (Figure 4.8b). It is noteworthy that, during the analysis, the

temperature of the stack changed drastically; however, at this stage, this change is not reflected in the cell's corresponding V-I values.

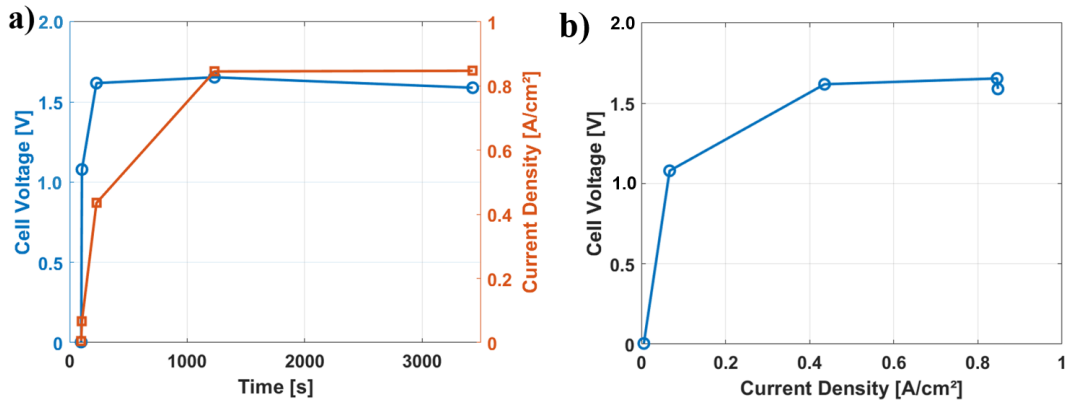

Figure 4.8 a) Time-dependent cell voltage and current density b) V-I curve

The calculated stack and tank temperatures over time using the parameter values listed in Table 3.2 from the methodology section, are shown in Figure 4.9. Due to the nature of electrolysis, the temperature of the stack increases over time, and as expected, both components also experience a temperature rise. For simplicity, the KOH molarity was assumed to be zero. This assumption was made considering that the electrolyte concentration would have a negligible influence on the tank temperature and overall energy balance during the startup period.

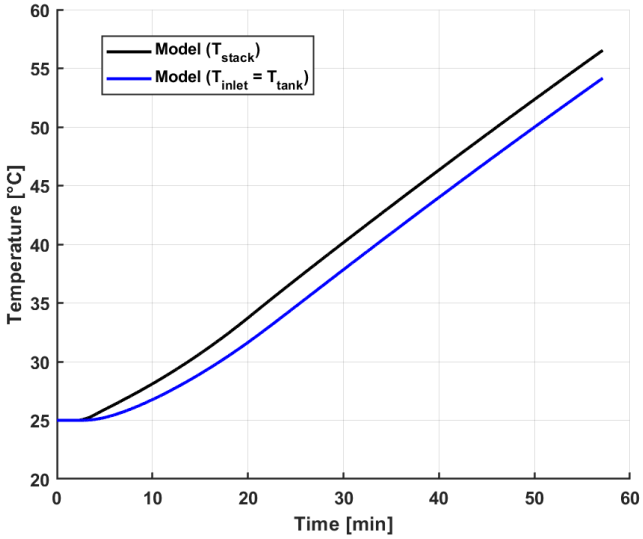

Figure 4.9 The stack and tank temperatures over time

The water leaving the tank heats up in the electrolyzer stack and returns with a higher temperature, gradually increasing the tank temperature. Thus, the water entering the stack may not fully compensate for the stack's heat generation, making the inlet flow rate and tank mass two critical parameters, along with modeling values such as stack heat capacity and fluid-based properties such as heat capacity and enthalpies. Therefore, a sensitivity analysis was conducted to examine the effects on stack and tank temperatures. All other parameters, except the investigated variable, were kept the same as in Table 3.2.

Enthalpy and heat capacity (C) values were incorporated into the model to investigate their influence on system behavior. Data from CoolProp, Mench, and NIST were used, respectively, for enthalpy and c_p values for H_2, O_2, and H_2O in the modeling. Figure 4.10 compares these datasets.

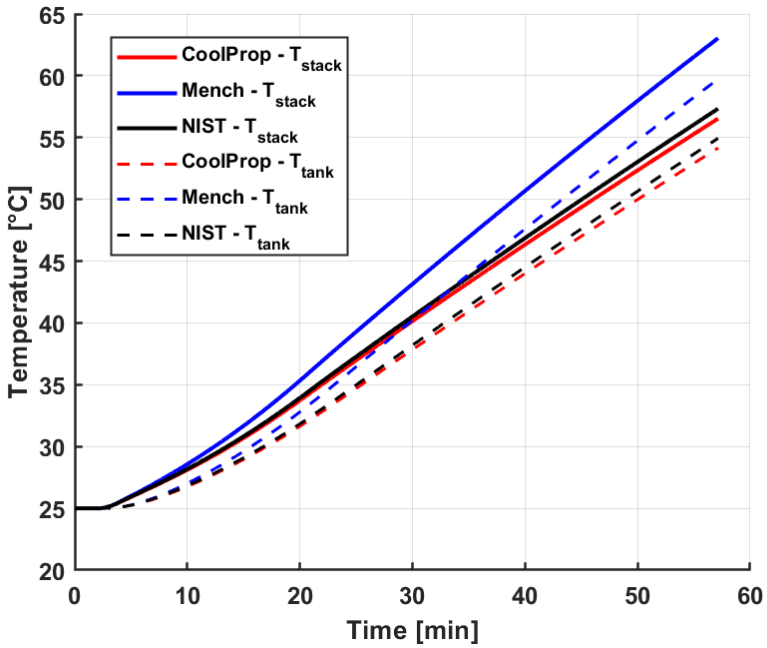

Figure 4.10 Comparing the approaches of enthalpy calculations

The results obtained using data from Mench (2008) are considerably higher, as they correspond to a broader temperature range for water in the vapor phase. Although this dataset was used to calculate the reaction enthalpy in V_{Nernst}, it primarily represents vapor-phase conditions. In contrast, the NIST-based polynomial functions (*NIST*

Chemistry WebBook, 2025) and the CoolProp data integrated into MATLAB show strong consistency. Therefore, the NIST polynomial dataset was adopted for the subsequent sensitivity analyses due to its faster computational performance.

The temperature of the water tank varies according to the temperature of the water returning from the electrolyzer stack; a larger tank mass results in a slower temperature change. Hence, it was considered an important variable to investigate. Figure 4.11 presents the electrolyzer stack temperatures for water tank masses ranging from 2 to 20 kg.

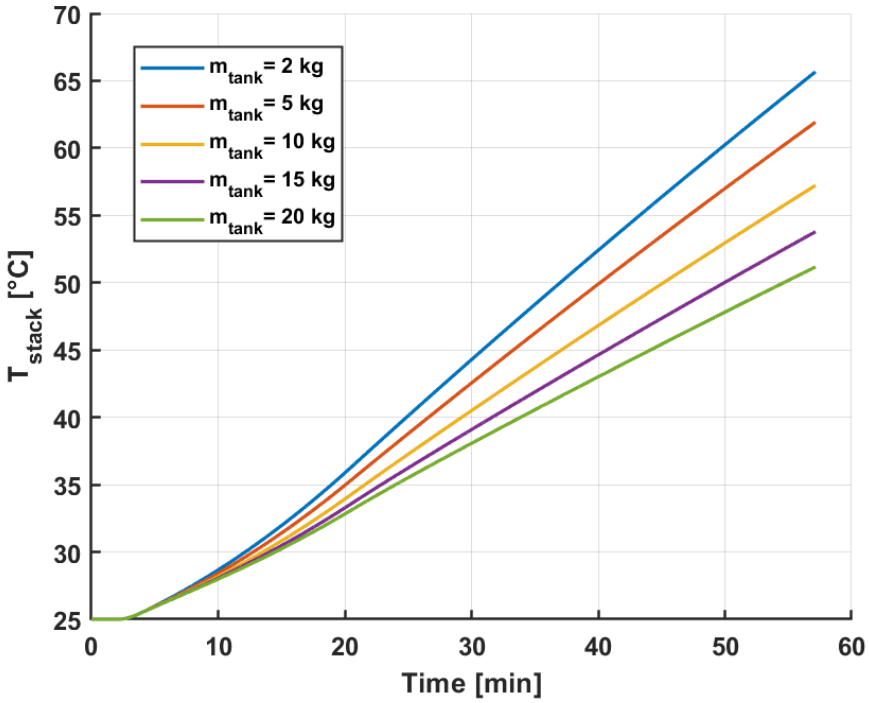

Figure 4.11 Effects of the water tank mass on stack temperature

As expected, the stack temperature reaches its lowest value when the electrolyte tank mass is at its maximum. This behavior arises because the water returning from the stack cannot elevate the temperature of a larger tank as rapidly, leading to a slower overall thermal response and lower recirculation temperature. In contrast, a smaller tank exhibits faster heat-up dynamics, as the higher inlet temperature promotes faster thermal coupling and accelerates the stack heating process.

The inlet mass flow rate to the stack is another critical parameter that significantly influences the stack's heating behavior. Correspondingly, stack temperature profiles for different flow rates (0.001-0.1 kg/s) are represented in Figure 4.12.

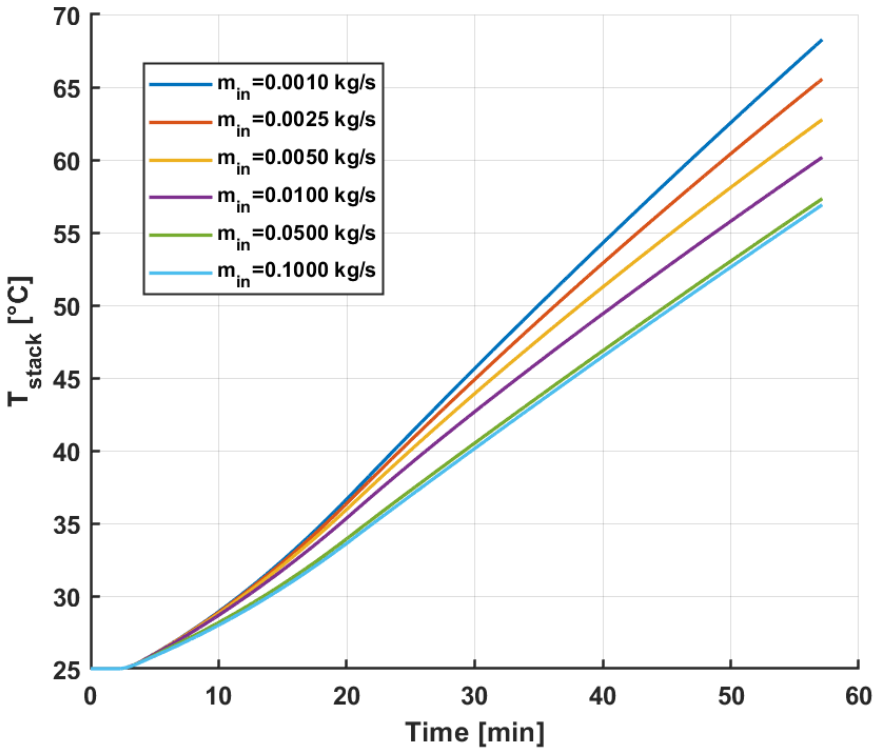

Figure 4.12 Effects of the inlet water mass flow rate on stack temperature

The rate of temperature rise in the stack is slowed by increasing the inlet flow rate; however, after a certain point, this effect becomes insignificant. Stack temperatures are approximately 57 °C at mass flow rates of 0.1 kg/s and 0.05 kg/s, but temperatures can rise as high as 68 °C at a much lower flow rate of 0.001 kg/s. Therefore, it is essential to maintain an optimal flow rate for effective operation. At this stage, the influence of stack configuration was not considered in the calculations.

Finally, the impact of heat capacity (C), one of the key parameters, was examined. The stack temperature variations for different heat capacities (10-200 kJ/K) are presented in Figure 4.13.

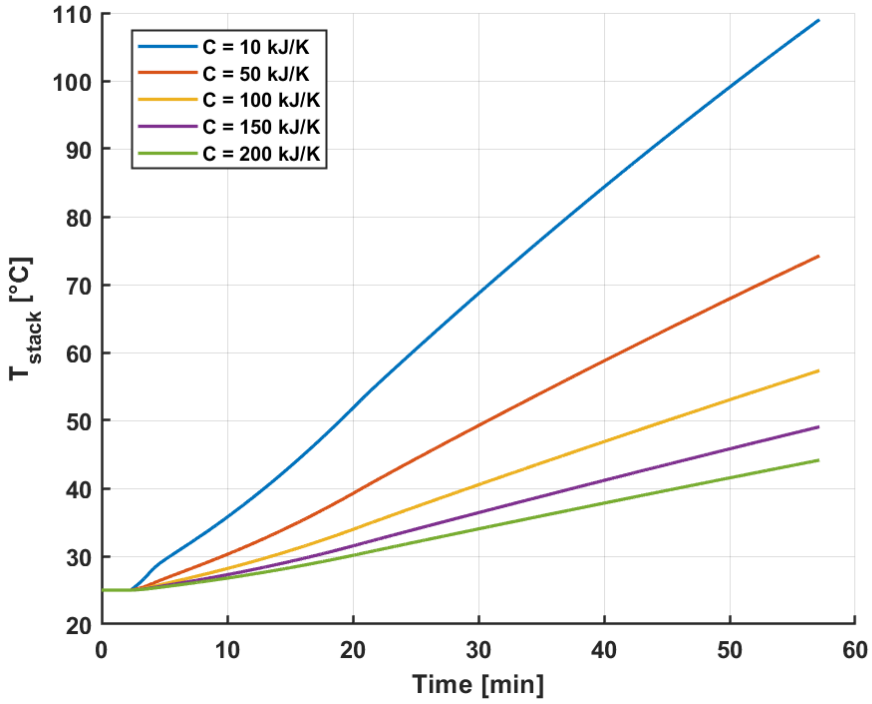

Figure 4.13 Effects of heat capacity on stack temperature

The stack heating rate is severely affected by the heat capacity. While a higher C value results in a slower heating profile, an increased C value causes the temperature to rise more quickly. At the end of the analysis, Capacity values higher than 150 kJ/K result in a stack temperature lower than 50 °C. However, when the heat capacity value was low, such as 10 kJ/K, the stack temperature was even higher than 100°C, reaching 110°C.

The modeling in MATLAB was followed by the development and implementation of the system in Simulink. Since the model is an algebraic loop and Fsolve is not supported in Simulink, the structure of the stack model in Simulink is validated against the MATLAB model, using a fixed inlet temperature value set to a constant 320 K. The tank heating profile is shown in Figure 4.14, comparing Simulink and MATLAB results.

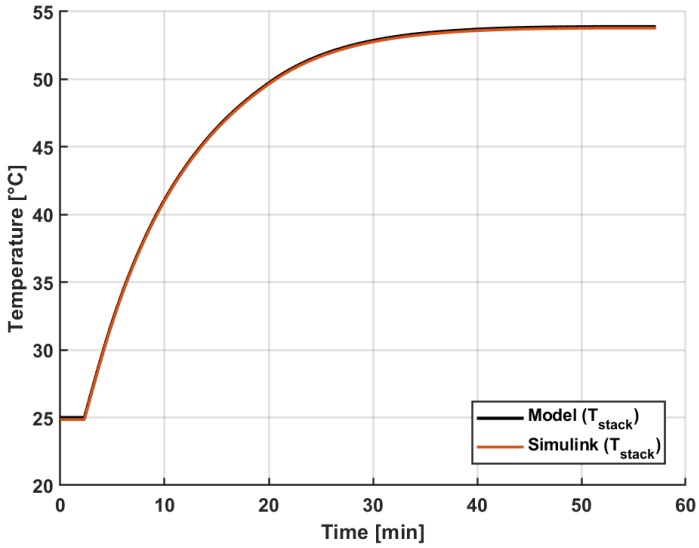

Figure 4.14 Comparison of the stack models in MATLAB and Simulink

The Simulink and MATLAB solutions show identical results under the condition where no water tank is implemented, and the inlet temperature remains constant at 320 K. Following this comparison, water tanks were implemented, as previously shown in Figure 3.5. The results of comparing MATLAB with Simulink with integration on the water tank are presented in Figure 4.15.

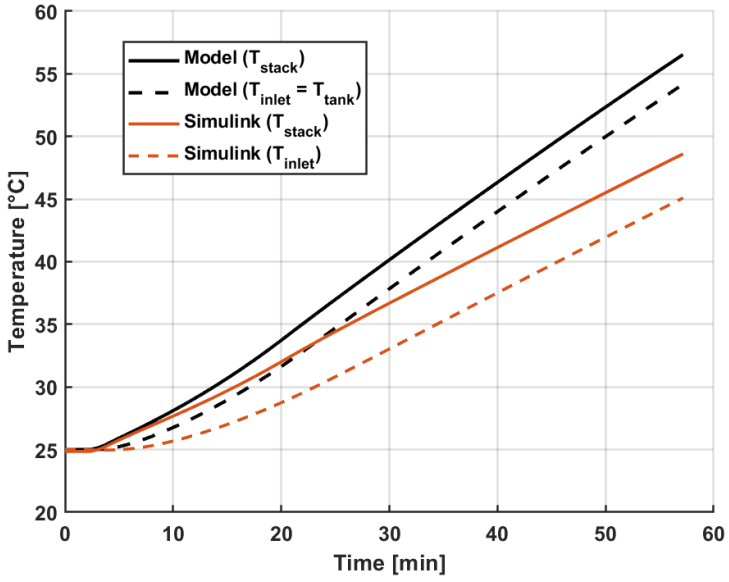

Figure 4.15 Comparison of BoP models in MATLAB and Simulink

Using the same values for the stack and tanks, the results were significantly different for MATLAB and Simulink models. Since axiality components and pipes

were used in the Simulink analysis, it is believed that their behavior greatly affected the results. At the end of the simulations, for Matlab, the stack temperature and tank temperature were approximately 56°C and 54°C, respectively. However, the Simulink results were 48.5°C and 45°C, much lower than the MATLAB results. Nevertheless, the water mass left in the tank was the same for both results, at 9.73 kg.

4.2.2 Simulation of Integrated PV-AEMWE-MH System

This section presents the results of the fully integrated system simulation under a realistic solar irradiance profile. The primary goal is to assess the system's dynamic operational integrity, focusing on the simultaneous performance of the MPPT-controlled PV array, the AEMWE stack, and the $LaNi_5$ Metal Hydride storage unit. A key component of this analysis involves a sensitivity study on the thermal management of the MH storage system. As can be seen in Table 4.4, the heat transfer coefficient varies depending on the application environment, method, and working fluid (*Fundamentals of Heat and Mass Transfer*, 2006). In general, it changes according to the adopted thermal management strategy. Thus, sensitivity studies were performed by varying the convective heat transfer coefficient (h_c), which serves as an indicator of the system's thermal management strategy (e.g., from passive cooling to forced flow). The critical impact of this thermal dissipation on hydrogen absorption kinetics and overall storage capacity over the simulation period has been quantified and discussed.

Table 4.4 Values of the convection heat transfer coefficient depending on the process (*Fundamentals of Heat and Mass Transfer*, 2006)

Process	Convection Heat Transfer Coefficient ($W/m^2 \cdot K$)
Free convection	
Gases	: 2 - 25
Liquids	: 50 - 1000
Forced convection	
Gases	: 25 - 250
Liquids	: 100-20,000
Convection with phase change	
Boiling or condensation	: 2500 - 100,000

Firstly, July in Izmir was chosen as the reference period, as it represents the most demanding thermal operating conditions due to peak solar irradiance and high ambient temperatures. While this period offers the maximum solar energy potential, it simultaneously exposes the metal hydride storage system to the most severe temperature conditions, caused by increased hydrogen production rates and higher ambient temperatures. Under these conditions, hydrogen production reaches its peak; therefore, the number of metal hydride tanks was determined based on July's operating conditions.

The time-varying inputs driving the system's performance are the ambient temperature and solar irradiance profiles, initially obtained from the JRC Photovoltaic Geographical Information System (PVGIS) - European Commission (2025). The hourly input values for the PV-AEMWE system, defining the conditions for the one-day simulation, are presented in Table 4.5.

Table 4.5 Hourly solar and ambient temperature data and corresponding resistance values in July

Time (h)	Temperature (°C)	Irradiance (W/m^2)	Resistance (Ω)
1	23.09	0	–
2	22.5	0	–
3	21.97	0	–
4	21.5	0.62831	3344.2
5	21.55	52.75	57.254
6	23.26	206.24	16.02
7	25.44	409.27	8.3761
8	27.77	597.02	5.8284
9	29.85	759.23	4.6173
10	31.61	853	4.1125
11	32.94	893.85	3.916
12	33.79	869.15	4.0076
13	34.19	785.66	4.3983
14	34.16	644.54	5.2915
15	33.71	464.72	7.1923
16	32.84	261.71	12.315
17	31.59	72.619	40.541
18	30.05	14.433	180
19	28.52	0	–
20	27.25	0	–
21	26.29	0	–
22	25.4	0	–
23	24.59	0	–
24	23.85	0	–

The irradiance values shown in the table are the effective measurements after optical adjustments, which reflect an average reduction of about 9% during sunlit hours. Similarly, the resistance (Ω) values represent the instantaneous equivalent load resistance calculated by the MPPT algorithm rather than a direct environmental measurement.

The reliability of the overall integrated system model necessitates the accurate validation of all sub-components, beginning with the electrical power source. The PV subsystem model, based on the TrinaSolar Duomax TSM-DEG5-60C-280W module, was validated by comparing its simulated performance against the manufacturer's specifications under Standard Test Conditions (STC) (1000 W/m^2, 25 °C).

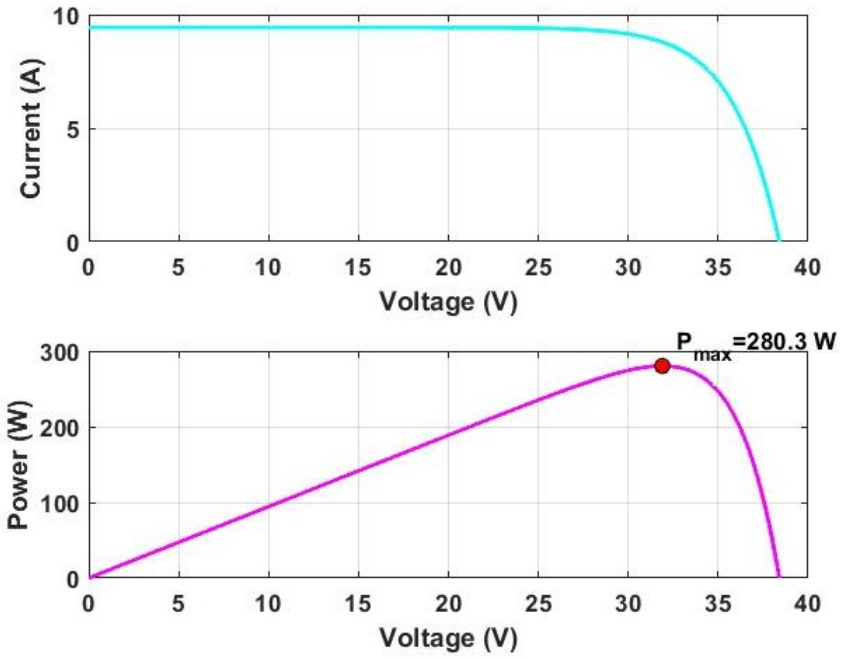

Figure 4.16 Results of the MPPT model

Table 4.6 compares the key electrical parameters, which represent the detected maximum operating points and the curve's limit points, obtained from the simulation output with the manufacturer’s data sheets (Trinasolar , 2017).

Table 4.6 Comparison of simulation results of MPPT-PV with manufacturer's data sheets (Trinasolar , 2017)

Parameter		Simulation Results	Manufacturer Spesc. (±3%)
P_{max} (W)	Peak Power	280.3	280.0
V_{MPP} (V)	Max. Power Voltage	31.896	31.7
I_{MMP} (A)	Max. Power Current	8.788	8.84
V_{OC} (V)	Open-Circuit Voltage	38.406	38.4
I_{SC} (A)	Short-Circuit Current	9.513	9.44

The simulated maximum power of 280.3 W shows excellent agreement with the rated power provided by the manufacturer, with a deviation of only 0.11%. Notably, the minimal deviations observed in the V_{MPP} and I_{MMP} values confirm that the MPPT model accurately locates the maximum operating point successfully. This fidelity ensures reliable MPPT tracking under fluctuating irradiance and temperature conditions.

Following this, the comparison between the metal hydride model developed in Simulink and the experimental data reported by Tong et al. (2019) is presented in Figure 4.17. Figure 4.17a illustrates the time-dependent weight fraction (%), while Figure 4.17b shows the average temperature of the MH bed.

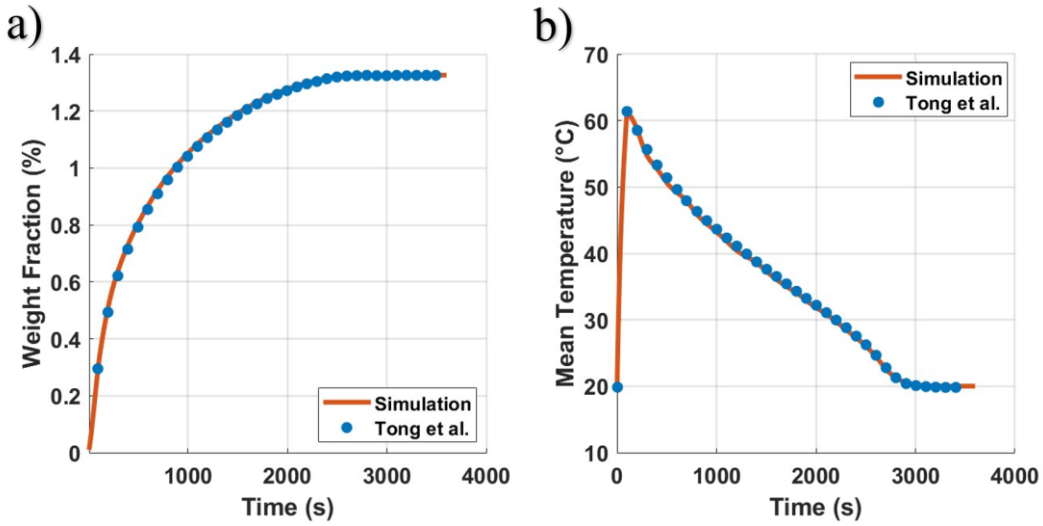

Figure 4.17 Validation of the metal hydride model developed in Simulink against the experimental data of Tong et al. (2019), presenting a) time-dependent weight fraction (%) b) average temperature of the MH bed.

After validating the components of the system, the integrated PV-AEMWE system was simulated, and the transient results in Figure 4.18, show its dynamic response over a 24-hour period in July.

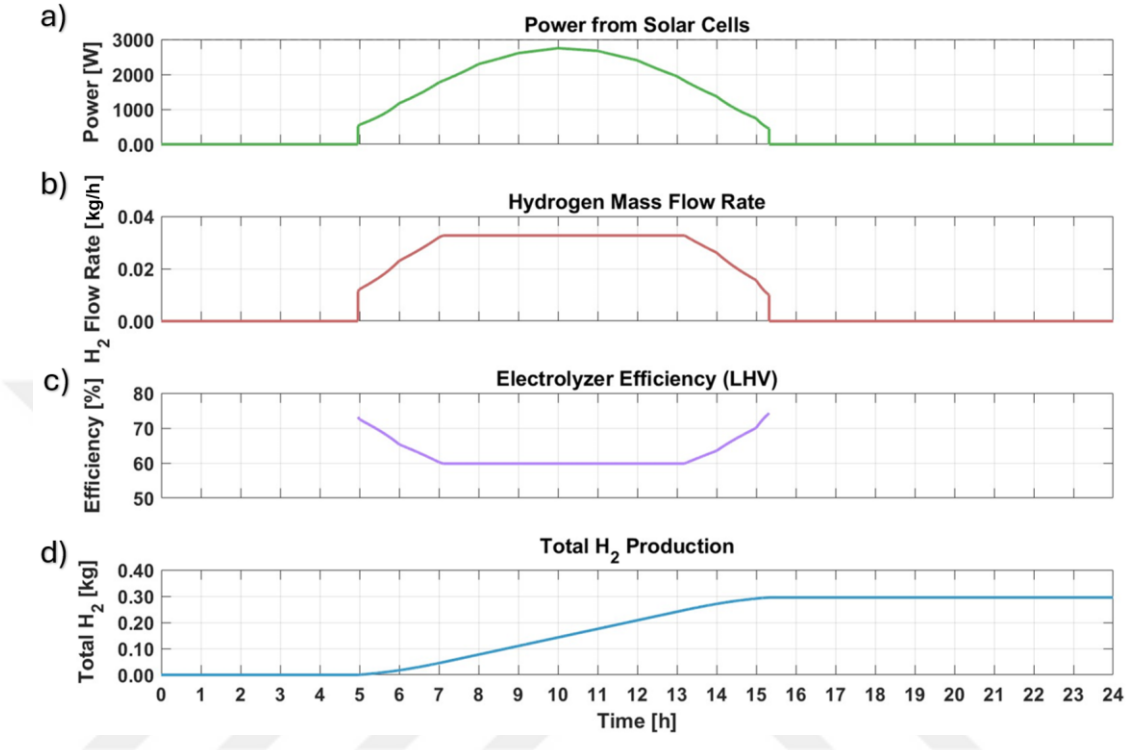

Figure 4.18 Daily performance of the PV-AEMWE during summer, showing a) PV power (W), b) H_2 mass flow rate (kg/h), c) electrolyzer efficiency (LHV%), and d) total H_2 production (kg).

Power generation commenced around the 5th hour and ceased around the 15th hour, aligning perfectly with the daylight hours of the input profile. The system successfully achieved a peak electrical output of 2749 W near midday. As the available electrical power increases, the hydrogen mass flow rate (Figure 4.18b) increases accordingly until the electrolyzer reaches its maximum allowable power limit of 1818 W, corresponding to operation at the maximum current density of 3.5 A/cm^2. The hydrogen mass flow rate reaches its maximum at approximately 7.1 h and remains nearly constant at around 0.0326 kg/h. During this period, additional available power above the electrolyzer limit cannot be utilized by the stack. The flow rate then begins to decrease after hour 13.19, following the reduction in available electrical power.

Simultaneously, the electrolyzer efficiency, based on LHV, is depicted in Figure 4.18c and shows a minimum of 60% efficiency at peak power. This reduction is an

expected trade-off, as operation at higher current densities leads to increased losses, resulting in lower instantaneous efficiency but a higher hydrogen production rate. Despite the efficiency drop, the system successfully maintained an average efficiency of 62.3% (LHV) throughout the operational period. This average efficiency value is critically dependent on the stack's design; a higher number of cells would theoretically lead to higher efficiency by reducing the current density per cell. However, this design choice must be balanced against the resulting increase in initial capital costs. Cumulative hydrogen production (Figure 4.18d) increased steadily during the operational window, totaling 0.295 kg by the end of the day. This figure defines the total daily mass available for storage in the MH tanks. Based on the total hydrogen production, the required number of tanks was calculated as 5.4922, with each tank having a height of 0.9 m and a radius of 0.02 m. Accordingly, 6 tanks were considered in the analysis to fully accommodate the daily hydrogen production.

Regarding energy utilization, although the electrolyzer efficiency did not fall below the minimum operational threshold (55%), the available PV power exceeded the maximum allowable power of the electrolyzer during certain periods. To prevent energy waste under these conditions, a battery storage system was considered to capture the surplus electrical energy. Therefore, Figure 4.19 presents the time-dependent excess power and the corresponding cumulative energy, showing the electrical power that cannot be utilized by the electrolyzer and the total unused energy over the day.

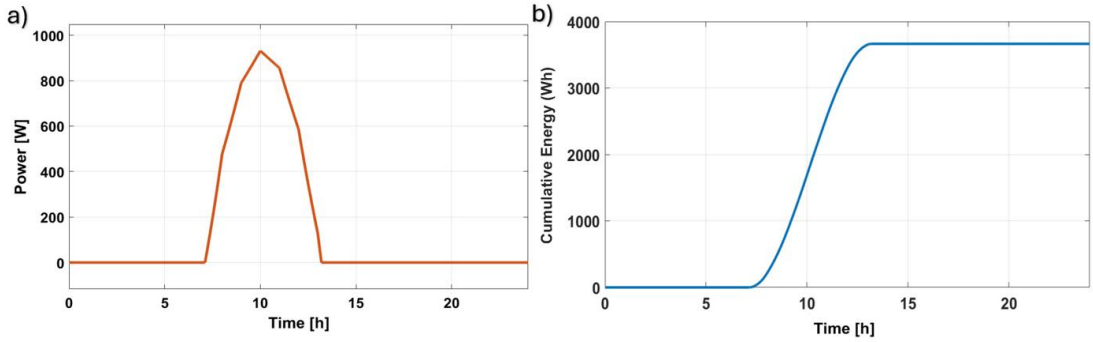

Figure 4.19 a) Surplus electrical power profile and b) daily accumulation of unused electrical energy

In the Figure 4.19a, the excess power appears between 7.1 h and 13.19 h, reaches a maximum of 931.1 W at 10 h, and then decreases. These values are in agreement with

the time intervals and peak power points indicated in Figure 4.18. As depicted in Figure 4.19b, the total unused electrical energy accumulated over the day amounts to approximately 3666 Wh. Considering the surplus power profile, a battery with a charge power of approximately 1 kW and an energy capacity of around 4 kWh is sufficient to capture excess PV generation over the day.

Hydrogen produced by the electrolyzer stack is sent to the MH storage subsystem and stored directly as it is produced. The system's control strategy relies on a PID and an on/off controller. The hydrogen flow rate is dynamically regulated by the PID controller to maintain the internal tank pressure at a conservative set point of 25 bar, below the maximum allowable pressure of 30 bar specified by the commercial metal hydride tank. Thermal regulation is prioritized due to the exothermic absorption reaction: the maximum operational temperature for the tanks was set at 60°C, immediately pausing hydrogen filling until the temperature drops to a safe resumption level of 50°C with an on/off controller. The control logic enables the simultaneous co-filling of two or more tanks when their temperatures and pressures fall within safe ranges.

Thermal heat removal plays a critical role in governing absorption kinetics; therefore, a sensitivity study was conducted using four distinct heat transfer coefficient values from 5 to 2000 $W/m^2 \cdot K$. Within the specific context of the summer scenario in Izmir, coefficients of 10, 50, 500, and 2000 $W/m^2 \cdot K$ were chosen to represent a wide range of heat transfer methods, from natural convection to advanced forced cooling strategies. The impact of these coefficients on the maximum bed temperatures of the tanks, as they respond to varying ambient temperatures and ongoing absorption processes, is illustrated in Figure 4.20.

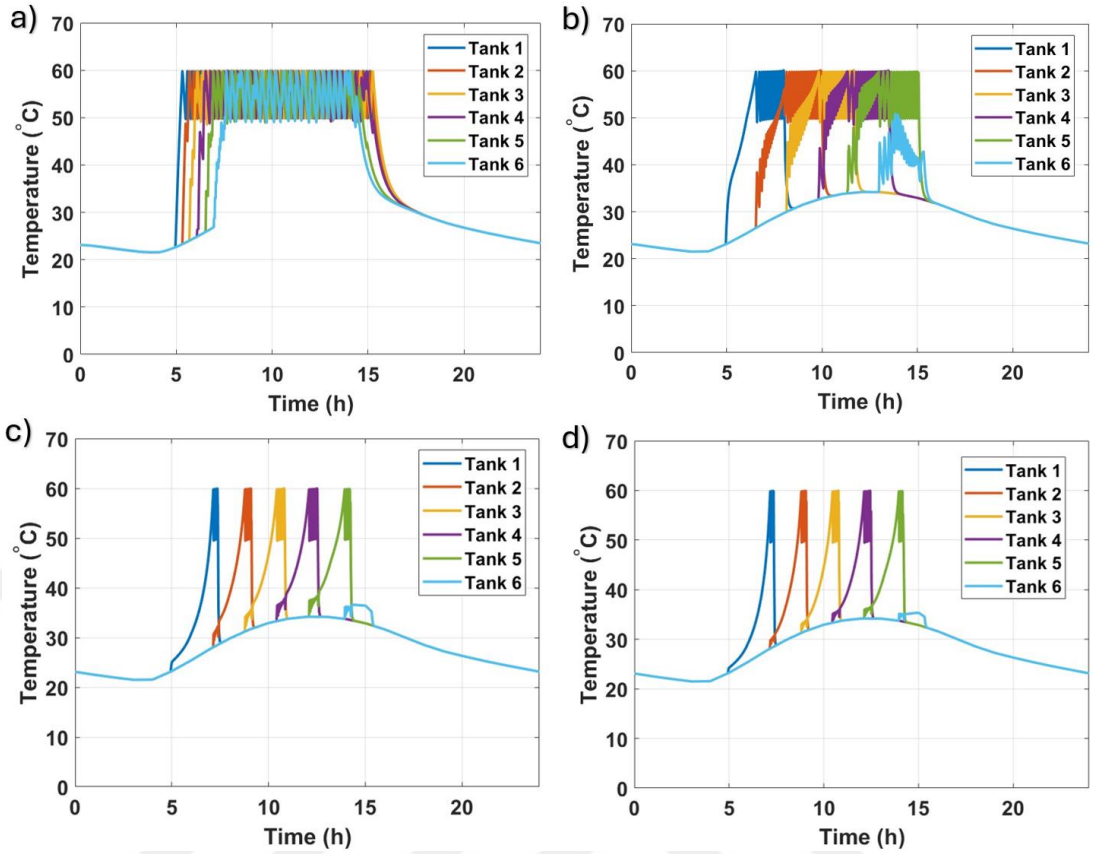

Figure 4.20 Maximum metal hydride bed temperature profiles during summer for convection coefficients of a) h_c = 10, b) h_c = 50, c) h_c = 500, d) h_c = 2000 (W/m^2·K)

The analysis was based on the thermal control limits (60°C maximum operating temperature, 50°C restart temperature) and directly investigated the tanks' transient thermal response to different convective heat transfer coefficients. As expected, increasing the hc accelerates heat transfer through the tank wall, leading to rapid thermal cycling at higher values and severely limited heat transfer at lower values. A key observation is that a high heat transfer coefficient delays the moment when the tanks reach their maximum temperature limit. This delay indicates a longer absorption period, as the system becomes more efficient at transferring heat; consequently, absorption can continue for a longer time before reaching the 60°C ceiling. For instance, at a low coefficient, when h_c is 10 W/m^2·K (Fig. 4.20a), the tanks reach their maximum temperature in 5.32 hours. When h_c is increased to 500 W/m^2·K (Fig. 4.20c), this duration extends to 7.15 hours.

Furthermore, increasing h_c reduces the cooling duration. By accelerating the transition from the maximum operating temperature back down to the minimum threshold, the tanks reach the refill-ready range much sooner. The impact is most severe under conditions simulating natural convection, h_c = 10 W/m^2·K. In this case, the minimal heat transfer leads to prolonged periods of thermal unavailability, limiting the instantaneous absorption and creating larger intervals between the filling cycles of individual tanks.

While the maximum temperature serves as the primary safety constraint, average bed temperature profiles are also presented to better characterize the system's overall behavior. The transient evolution of the average tank temperature for different convective heat transfer coefficients (h_c = 10, 50, 500, and 2000 W/m^2·K) is presented in Figure 4.24.

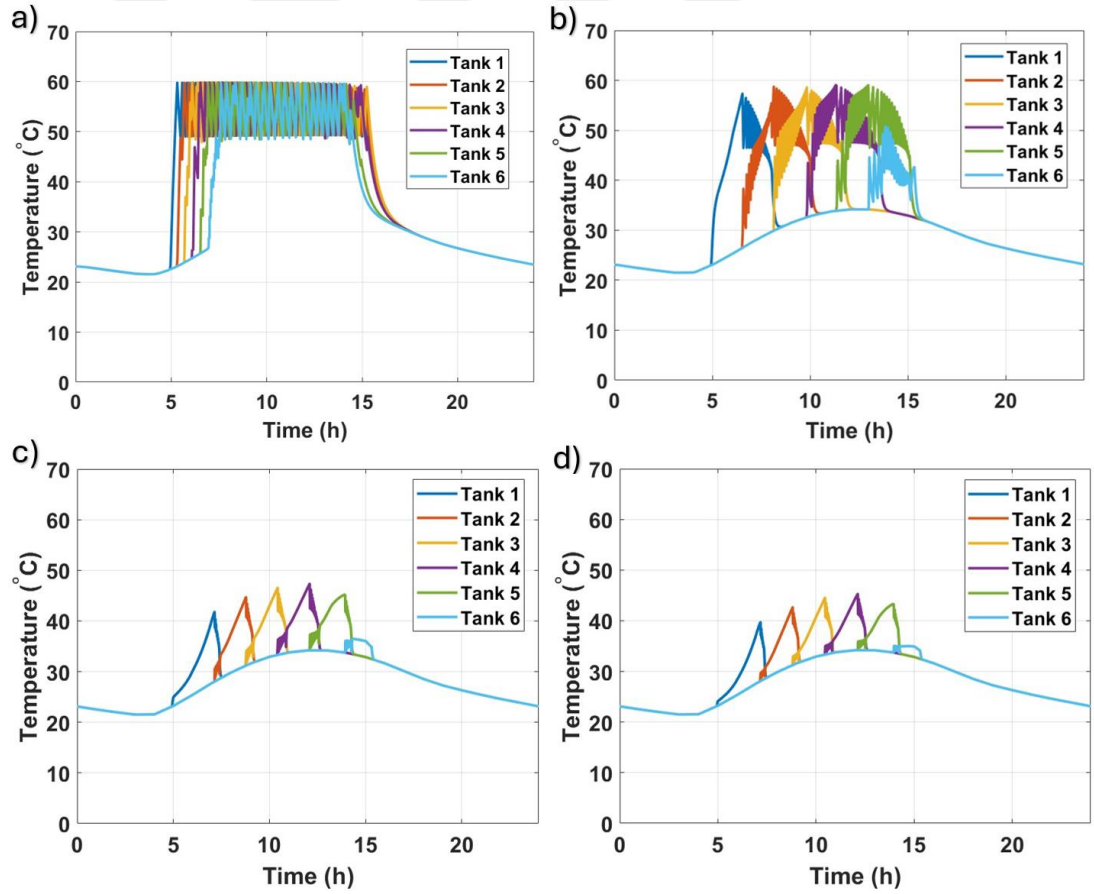

Figure 4.21. Mean temperatures of each metal hydride tank bed during summer for convection coefficients of a) h_c = 10, b) h_c = 50, c) h_c = 500, d) h_c = 2000 (W/m^2·K)

At lower heat transfer coefficients (h_c = 10 and 50 W/m^2·K), there is a clear increase in the average temperature (Fig. 4.21a–b). In contrast, for higher heat transfer coefficients (h_c = 500 and 2000 W/m^2·K), the average temperature does not even surpass 50°C (Fig. 4.21c–d). Additionally, compared to the average and maximum temperatures (Fig. 4.20), they stay closer at lower h_c values. As h_c rises, the improved heat transfer causes a larger gap between the maximum and average temperatures, keeping the average temperature much lower. Specifically, for 10 W/m^2·K, no noticeable difference is observed between the temperature profiles in Fig. 4.20a and Fig. 4.21a. However, when comparing Fig. 4.20d and Fig. 4.21d, although the shapes of the curves remain similar, the temperature levels are roughly 15-20 °C lower.

Furthermore, it should be noted that the gas temperature is assumed to be equal to the average bed temperature. Under this assumption, as the mean bed temperature approaches the maximum bed temperature, the difference between the equilibrium pressure and the gas pressure decreases, resulting in a lower absorption rate. This effect is particularly pronounced at lower heat transfer coefficients. When heat dissipation is insufficient, the elevated bed temperature causes the equilibrium pressure to approach the gas pressure closely, which limits the absorption process. In this case, absorption can only continue once the tank temperature decreases, allowing gas to enter the tank.

Mean temperature, gas pressure, and density inside the tank are directly related; therefore, a change in ρ_{gas} serves as a direct indicator of the ongoing absorption kinetics and the final state of the residual hydrogen in the tanks. Figure 4.22 presents the gas density dynamics for the six tanks under different thermal management scenarios, where h_c is 10, 50, 500, and 2000 W/m^2·K, respectively.

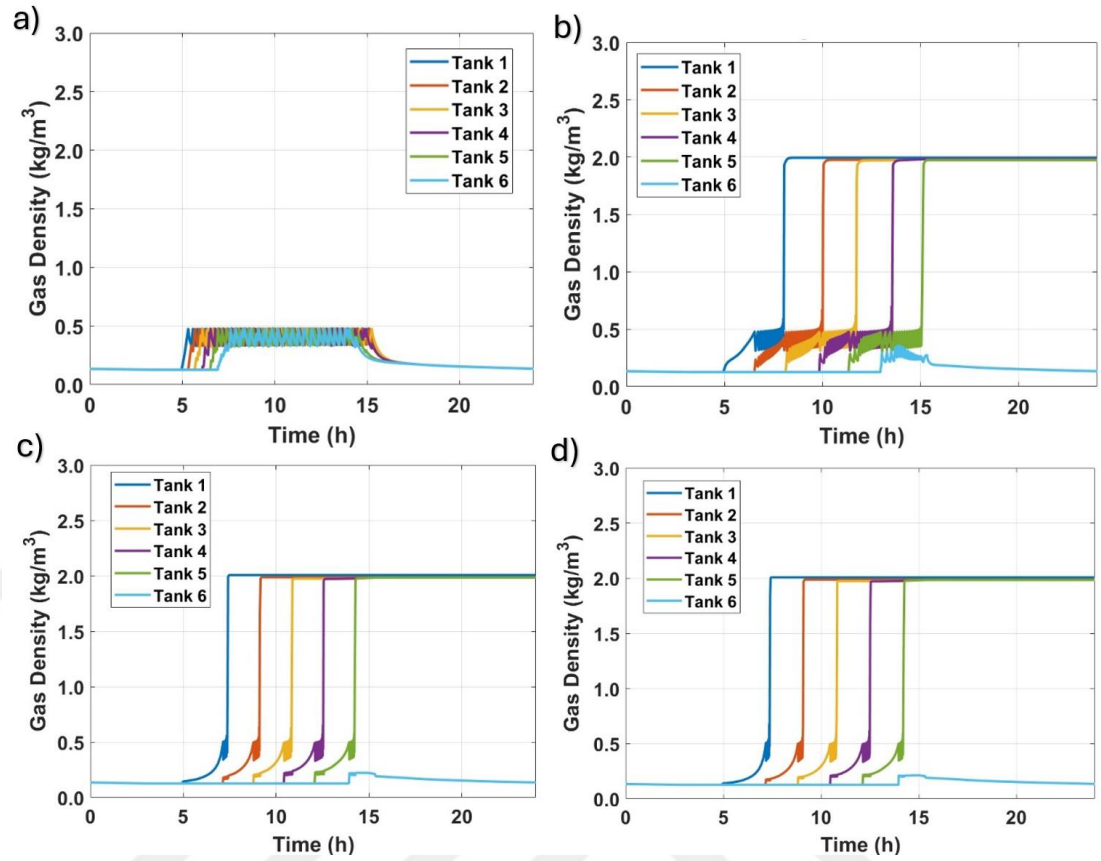

Figure 4.22 Gas densities of each metal hydride tank bed during summer for convection coefficients of a) h_c = 10, b) h_c = 50, c) h_c = 500, d) h_c = 2000 (W/m^2·K)

As shown in Figure 4.22a, the observed decrease in gas density indicates that the tanks are not fully filled. This behavior arises because hydrogen absorption continues, albeit at a reduced rate, leading to a gradual consumption of the gas phase and a corresponding decrease in gas density until equilibrium is reached. Under low heat transfer coefficients, heat removal from the tank is limited, resulting in a rapid temperature increase that restricts further hydrogen absorption. In tanks that are not fully filled, absorption therefore continues slowly throughout the day, preventing the accumulation of gas inside the tank. In contrast, the other cases (Fig. 4.22b–c–d) allow full tank filling, as hydrogen gas can continue to be supplied to the remaining space. For example, comparing the cases with 50 and 500 W/m^2·K (Fig. 4.22b and Fig. 4.22c), the gas density inside the tank reaches approximately 2 kg/m^3 after 7.4 and 8.3 hours, respectively. At high heat transfer coefficients, the exothermic heat released during the absorption reaction is rapidly removed from the system, preventing or

delaying the tank temperature from reaching the operational upper limit of 60 °C. This enables the filling process to proceed in an almost continuous manner.

To further illustrate the underlying thermal and absorption behavior, Figure 4.23 presents the temperature, gas density, and pressure evolution of the first MH tank (Tank 1) under lower and higher convection conditions.

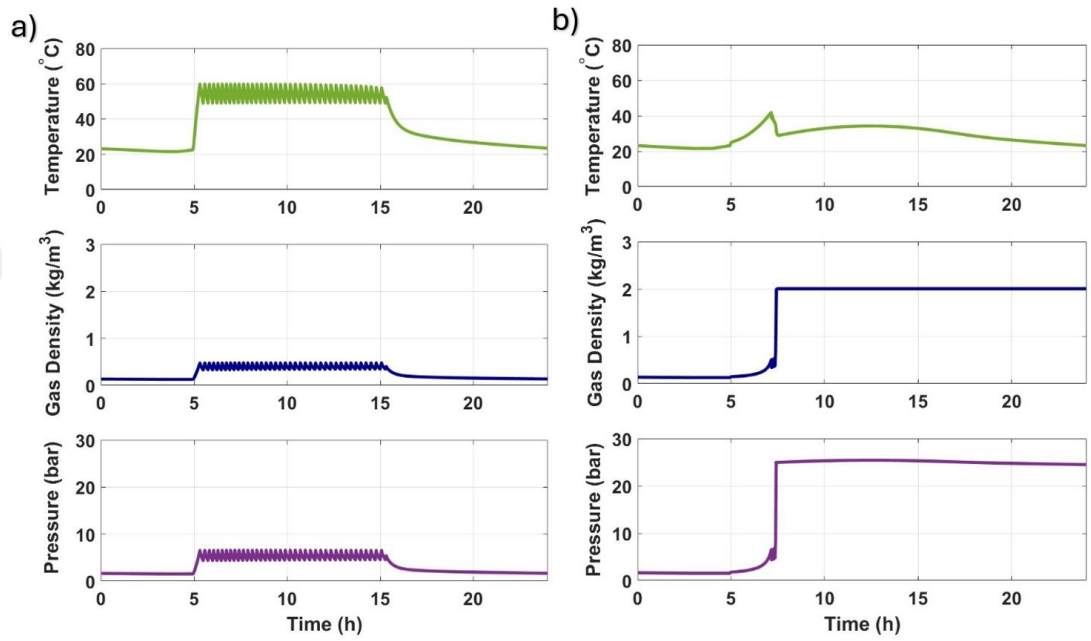

Figure 4.23 Mean temperature, H_2 gas density, and pressure changes over time in Tank 1 during summer for a) h_c = 10 W/m^2·K, b) h_c = 500 W/m^2·K

In Figure 4.23a, the bed temperature rapidly reaches the operational upper limit of 60°C and remains constrained by the on/off controller for an extended period. This thermal bottleneck forces the system into a repetitive cycle of pausing and resuming the gas inlet to prevent overheating. Consequently, the gas density profile remains at low levels and displays a fluctuating trend, which directly reflects the intermittent hydrogen inflow. In contrast, Figure 4.23b exhibits a more stable temperature evolution, which allows absorption to proceed in a smoother and more continuous manner. Consequently, the gas density continues to increase as the tank is filled until the internal gas pressure reaches the control limit. Once the tank is fully saturated, the PID controller effectively takes over to maintain stable pressure conditions at the allowed set point of 25 bar.

The previous analysis showed that the thermal behavior directly limited the operational time of the metal hydride tanks and, as a result, directly influenced the weight fraction (wf%). Building upon this finding, Figure 4.24 presents the final wf% values, achieved by each tank for the differing convective heat transfer coefficients.

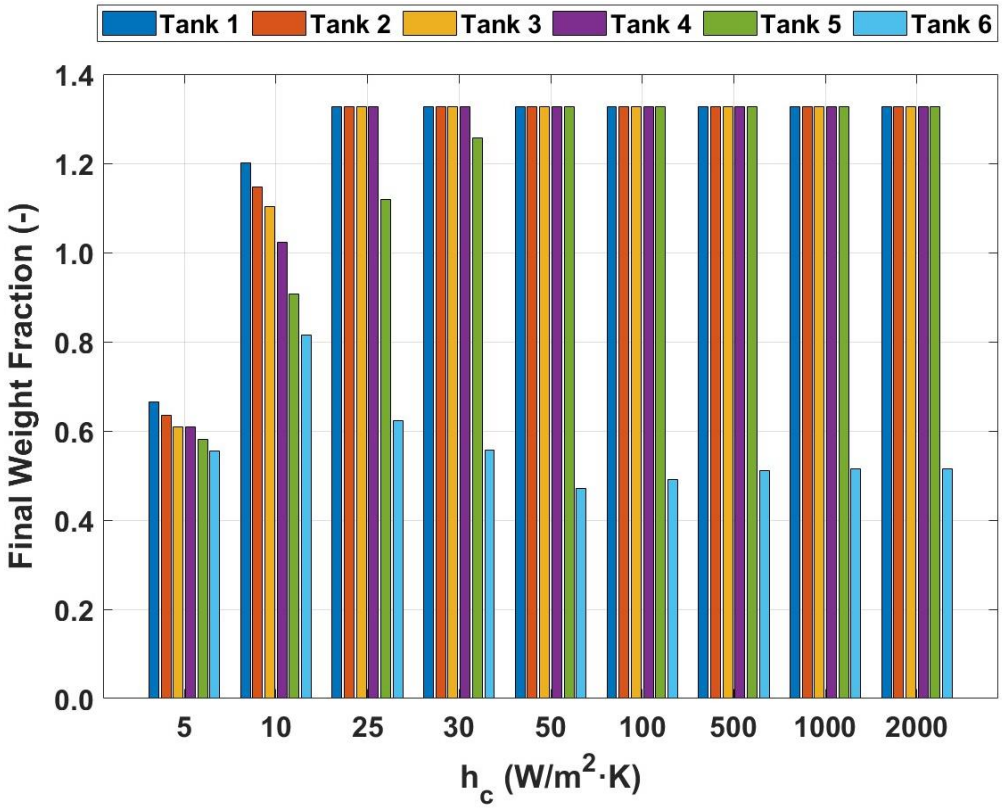

Figure 4.24 Weight fraction values of each metal hydride tank bed during summer with convection coefficients varying from 5 to 2000 W/m^2·K

The system's performance is most adversely impacted in the case where h_c = 5 W/m^2·K, resulting in the lowest overall storage capacity, as expected. Due to insufficient heat removal, the tanks subsequently receive less hydrogen gas, and the absorption process is severely limited. This indicates that a purely passive cooling configuration is inadequate for coupling metal hydride storage with transient hydrogen production. Under this condition, the weight fraction of all tanks remains below 0.7 wf%, with an average value of 0.61 wf%, and a maximum of 0.665 wf%, which is substantially lower than the nominal full capacity of 1.3 wf%.

When the convection coefficient is increased to 10 W/m^2·K, the pause times between successive filling stages are reduced, and a noticeable improvement in storage

performance is observed. The average weight fraction increases to approximately 1.03 wf%, indicating partial mitigation of the thermal limitation, although full utilization of the storage capacity is still not achieved.

On the other hand, the scenarios with higher values, h = 500 and h = 2000 $W/m^2 \cdot K$, both successfully mitigate the thermal limitation, achieving the maximum system capacity. Allowing the system to store the entire calculated daily production of 0.2950 kg. It should be noted that the simulations required the use of 6 tanks to fully meet the calculated storage requirement for the total daily hydrogen production. Consequently, the mean weight fraction for all tanks is approximately 1.19% once the daily produced hydrogen is fully absorbed. The slight variation observed in the final weight fraction of the last available tanks (e.g., Tank 5 versus Tank 6) is not indicative of a cooling failure or a difference in total storage capacity, but rather reflects the serial filling sequence used to distribute the final, residual mass required to meet the tank storage goal.

Following the analysis of July operating conditions, the system behavior is further examined under winter conditions to investigate the influence of reduced ambient temperatures and solar irradiance on hydrogen production and the cooling requirements of the metal hydride storage system. January is selected as the representative month for winter conditions. The hourly input values defining the conditions for the one-day simulation are presented in Table 4.7, initially obtained from JRC - Photovoltaic Geographical Information System (PVGIS) (European Commission, 2025).

Table 4.7 Hourly solar and ambient temperature data and corresponding resistance values in January

Time (h)	Temperature (°C)	Irradiance (W/m^2)	Resistance (Ω)
1	4.91	0	-
2	4.72	0	-
3	4.56	0	-
4	4.42	0	-
5	4.28	0	-
6	4.15	0	-
7	4.19	123.94	27.988
8	5.65	285.87	12.688
9	7.29	433.27	8.5236
10	8.56	507.43	7.3101

Table 4.7 (Continued)

Time (h)	Temperature (°C)	Irradiance (W/m^2)	Resistance (Ω)
11	9.51	512.89	7.21
12	10.12	490.4	7.5045
13	10.42	427.87	8.5223
14	10.39	319.06	11.233
15	10.01	191.35	18.172
16	9.2	2.0397	1241.6
17	8.22	0	-
18	7.43	0	-
19	6.79	0	-
20	6.48	0	-
21	6.03	0	-
22	5.66	0	-
23	5.34	0	-
24	5.09	0	-

Figure 4.25, shows system response over a 24-hour period for an average day in January, Izmir, utilizing the system presented previously, based on the data given in Table 4.7.

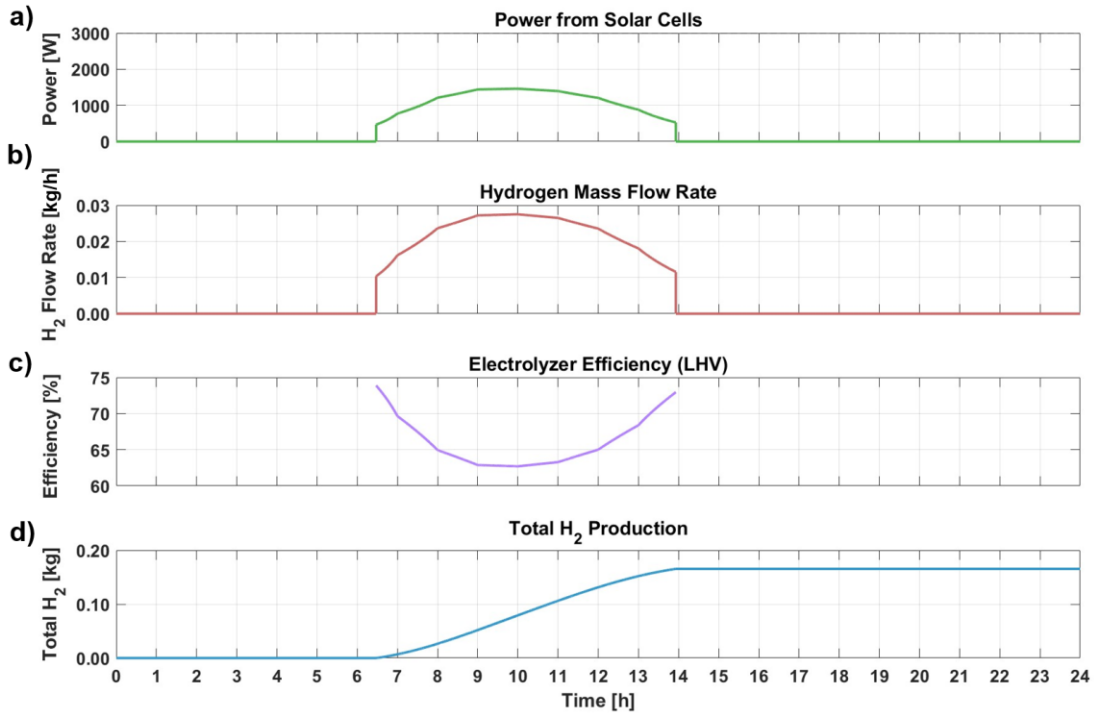

Figure 4.25 Daily performance of the PV-AEMWE during winter, showing a) PV power (W), b) H_2 mass flow rate (kg/h), c) electrolyzer efficiency (LHV%), and d) total H_2 production (kg).

During winter conditions, a total of 0.1656 kg of hydrogen is produced. The maximum electrical power from the photovoltaic panels reaches 1462.6 W, which is considerably lower than in summer. The lowest electrolyzer efficiency, based on the lower heating value (LHV), is 62.71%. Due to the reduced operating current compared to summer, the electrolyzer operates at a higher overall efficiency, resulting in an increased average efficiency throughout the day. The peak hydrogen mass flow rate occurs around midday, reaching 0.0275 kg/s. Comparing winter results (Figure 4.25) with the summer results (Figure 4.18), the decrease in available solar power causes a proportional drop in hydrogen production. Nevertheless, the number of metal hydride tanks remained at 6, consistent with the summer configuration. Due to lower hydrogen production in winter, the total storage need decreases. Based on the calculated total hydrogen production of 0.1656 kg, the required number of tanks is estimated to be 3.08. Therefore, it is unlikely that all six tanks will be fully used during winter operation.

For the winter analysis, the simulations were performed over a wide range of convective heat transfer coefficients (h_c = 5-2000 W/m^2·K) in order to directly evaluate the influence of heat transfer under reduced ambient temperatures. As previously discussed, the reliance on heat transfer effects is less pronounced in winter, since lower ambient temperatures naturally enhance convective heat transfer. Consequently, the selected cases primarily focus on low convection coefficients (h_c = 5 and 10 W/m^2·K), while intermediate and higher values (h_c = 50 and 500 W/m^2·K) are included for comparison. The corresponding maximum tank bed temperature profiles for those h_c values are presented in Figure 4.26.

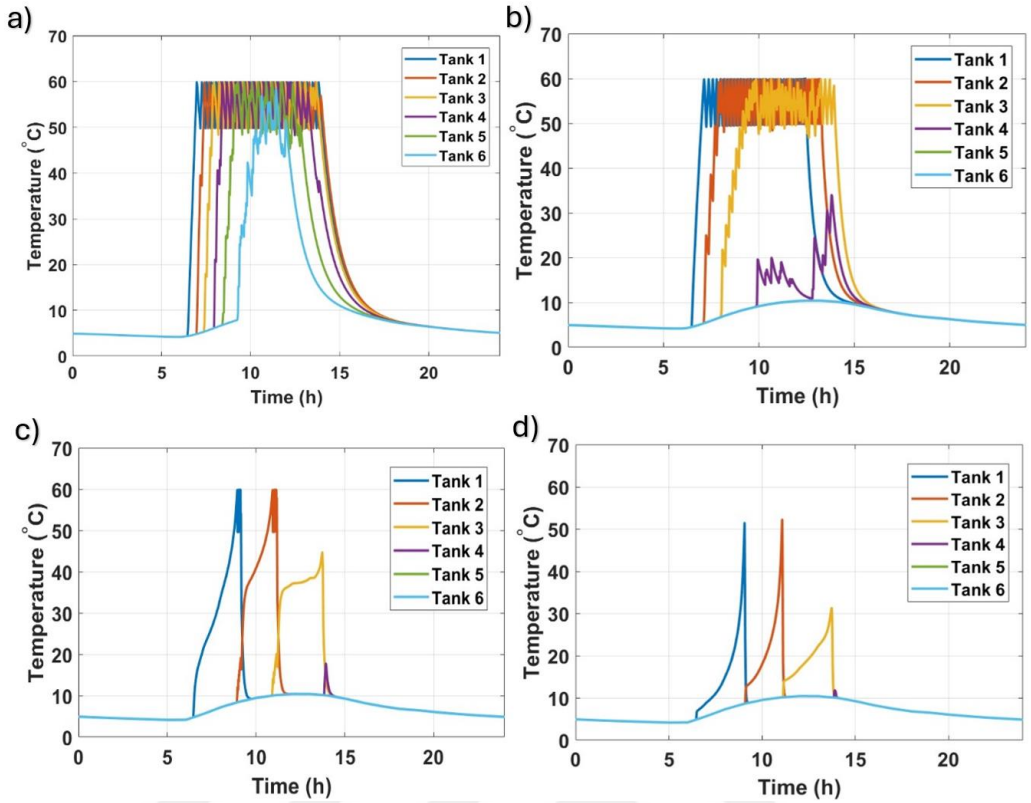

Figure 4.26 Maximum metal hydride bed temperature profiles during winter for convection coefficients of a) h_c = 5, b) h_c = 10, c) h_c = 50, d) h_c = 500 (W/m^2·K)

As previously stated, the number of tanks that should have been used was 3.08, but according to Figure 4.26a, up to 6 tanks were used. If the number of tanks had been decreased, it may have led to potential hydrogen waste. Examining the time taken to reach the maximum temperature, in the case of h_c 5 W/m^2·K, the tanks reach their maximum in approximately 7 hours and cool down to the lower limit in approximately 11 minutes, after which filling continues. When h_c is set to 10 W/m^2·K, this time decreases to 7.12 hours, and the cooling time decreases to approximately 7 minutes.

At higher coefficients, such as 50 W/m^2·K, it reaches its maximum in 8.9 hours, whereas at 500 W/m^2·K, it does not reach its maximum at all. This indicates that the on/off controller is not activated, and filling is performed continuously. Following this, the average temperature curves in the tank beds are presented in Figure 4.27 for the same h_c values.

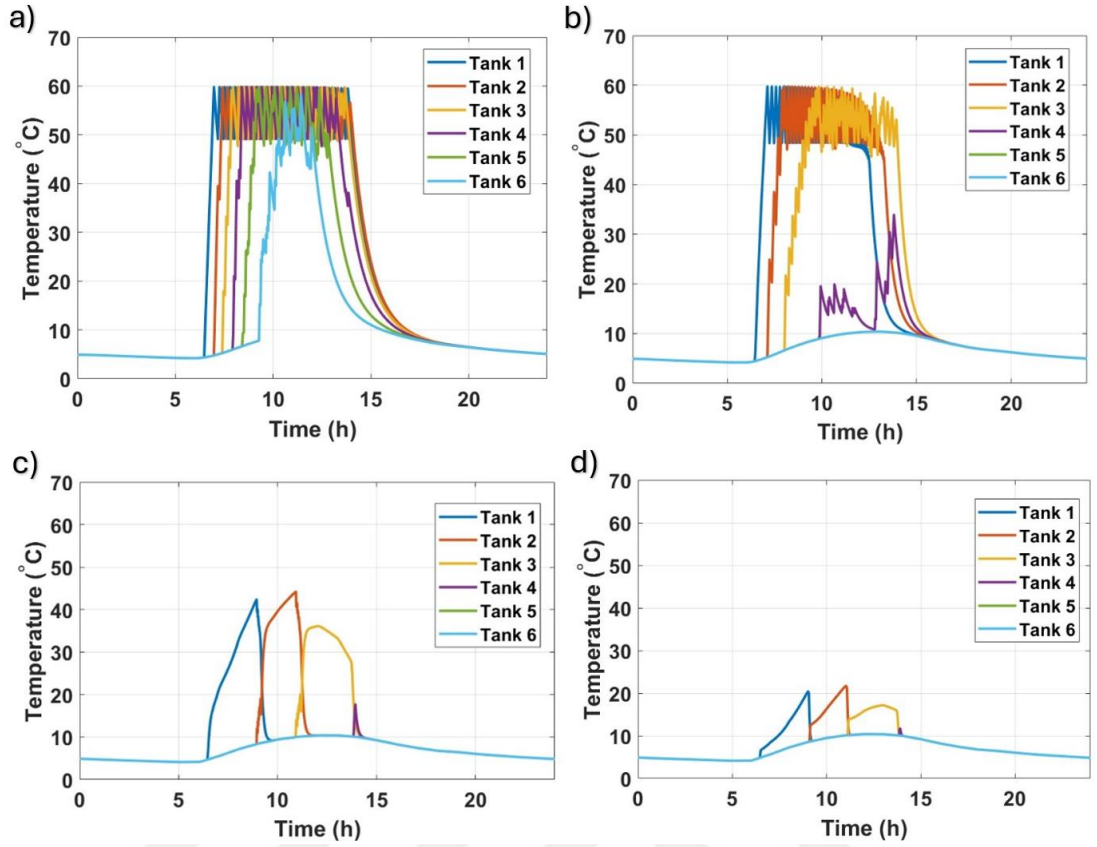

Figure 4.27 Mean metal hydride bed temperature profiles during winter for convection coefficients of a) h_c = 5, b) h_c = 10, c) h_c = 50, d) h_c = 500 (W/m^2·K)

Consistent with the summer scenario findings, the maximum and average temperatures are also very close under winter conditions at low convective heat transfer coefficients. On the other hand, at higher h_c values, the average tank temperature does not reach its maximum temperature. A comparison of Figure 4.27c and Figure 4.27d, clearly illustrates a pronounced reduction in the average temperature with increasing h_c. For 50 W/m^2·K, the highest average temperature of the first tank reaches 42.4 °C at 8.94 hours, whereas for 500 W/m^2·K, it is 20.37 °C at around 9th hours.

Following this, gas density graphs for observing the final status of the tanks are presented. in Figure 4.28.

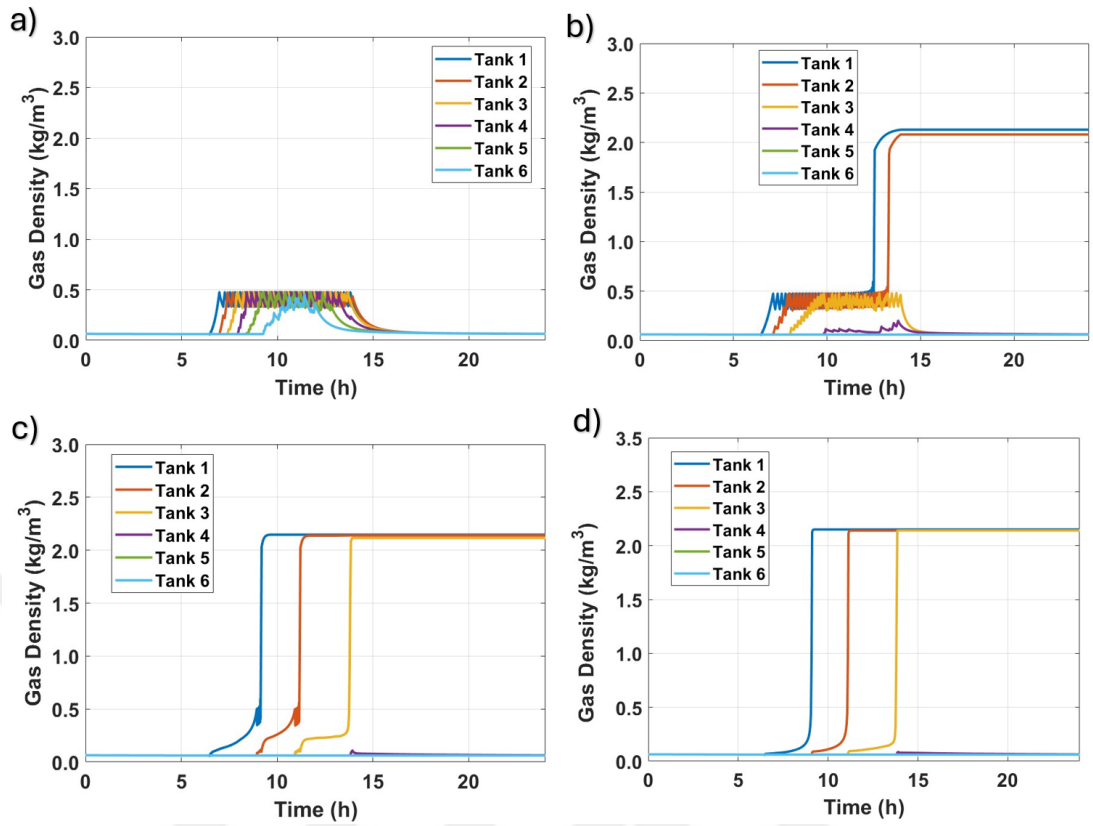

Figure 4.28 Gas densities of each metal hydride tank bed during winter for convection coefficients of a) h_c = 5, b) h_c = 10, c) h_c = 50, d) h_c = 500 (W/m^2·K)

Under winter operating conditions, a low convective heat transfer coefficient (Fig. 4.28a) limits heat removal from the tanks, preventing full tank filling and causing the gas density to gradually decrease toward the value corresponding to the equilibrium pressure by the end of the day. As the heat transfer coefficient increases, the tanks are able to reach their full storage capacity, allowing hydrogen gas to accumulate in the gas phase once the metal hydride becomes saturated.

From Fig. 4.28b and Fig. 4.28c-d, it can be observed that when h_c is 10 W/m^2·K, two tanks become fully saturated, while the remaining two tanks begin to fill but do not reach complete saturation within the operating period. In contrast, at higher convective heat transfer coefficients, the relevant tanks are fully charged and attain their maximum gas density values, indicating effective storage without thermal limitation.

The operating behavior of Tank 1 was also examined separately for convective heat transfer coefficients of 10 and 500 W/m²·K, in Figure 4.29.

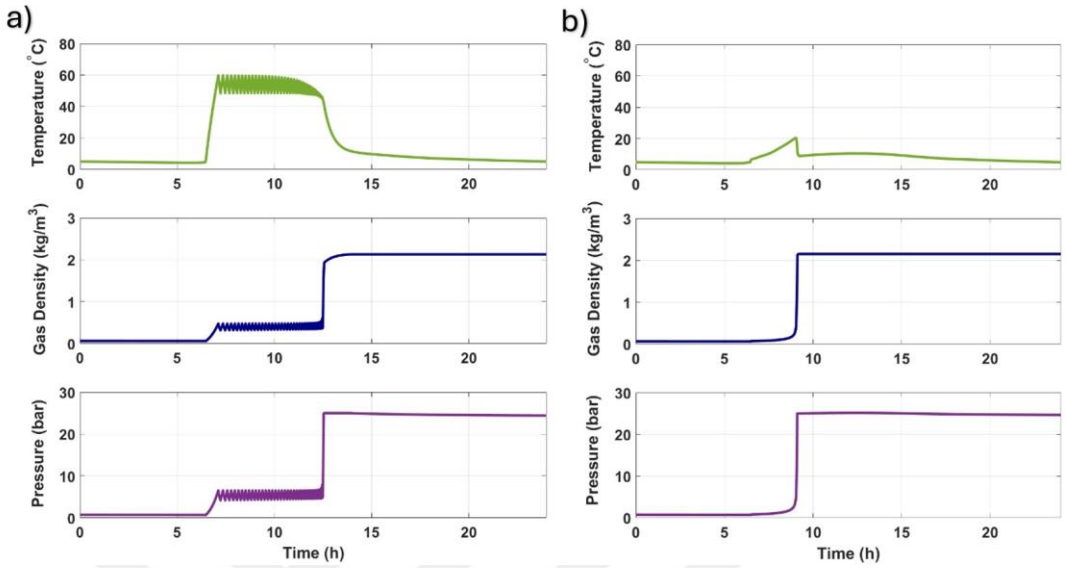

Figure 4.29 Temperature, gas density, and pressure changes over time in Tank 1 during winter for a) h_c = 10 W/m^2·K and b) h_c = 500 W/m^2·K

As previously discussed, the average temperature profiles exhibit a pronounced reduction with increasing h_c. For low heat transfer coefficients, the tank is frequently shut down by the temperature controller; however, at higher hc, the system operates continuously, indicating that shutdown is not required. The same operational trend is reflected in the gas density and pressure profiles. Despite these differences in thermal and dynamic behavior, both cases ultimately reach the specified maximum pressure limit of 25 bar, along with the corresponding maximum gas density.

Finally, the final weight fractions (wf%) for each tank are presented in Figure 4.30 to provide a quantitative assessment of how variations in convective heat transfer influence the hydrogen absorption performance of the metal hydride tanks.

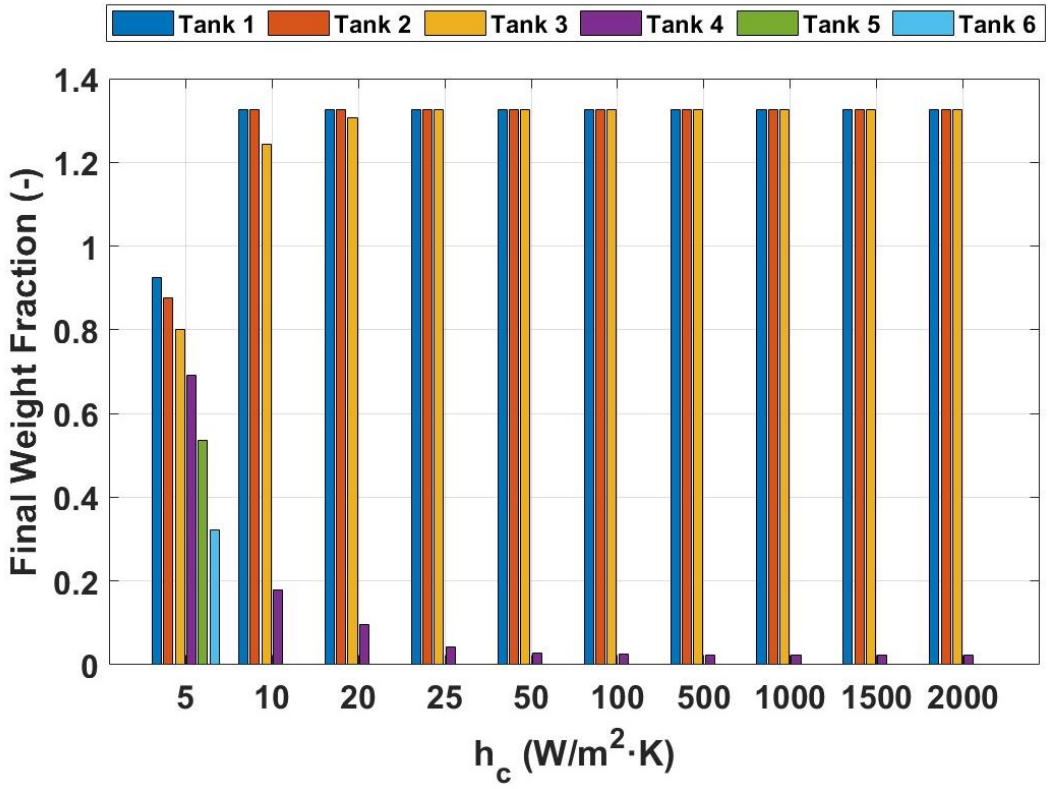

Figure 4.30 Final weight fraction values of each metal hydride tank bed during winter with convection coefficients varying from 5 to 2000 W/m^2·K

Ideally, three tanks are expected to reach a final weight fraction of approximately 1.33, while the fourth tank remains at a low value of around 0.02%. At lower convective heat transfer coefficients (h = 5–25 W/m^2·K), deviations from this ideal distribution are observed due to the intermittent opening and closing cycles imposed by the temperature controller. Nevertheless, despite these deviations, the results indicate that the entire amount of produced hydrogen can still be stored within the available tanks. At higher convective heat transfer coefficients (h = 100–2000 W/m^2·K), the temperature controller is no longer activated, allowing the tanks to be filled continuously and reach the ideal weight fraction values without interruption.

Finally, the influence of varying the convective heat transfer coefficient from 5 to 2000 W/m^2·K under both summer and winter conditions is summarized. Table 4.8 reports the corresponding hydrogen waste (%), peak heat extraction rate (kW), and total extracted heat over one day (kWh) for the summer conditions.

Table 4.8 Effect of convective heat transfer coefficient on hydrogen waste and heat extraction during summer

h_c ($W/m^2 \cdot K$)	Waste H_2 (%)	Peak Heat Extraction Rate (kW)	Total Extracted Heat in a day (kWh)
5	49.556	0.021	0.829
10	14.285	0.041	1.409
25	1.003	0.096	1.613
30	-	0.111	1.631
50	-	0.145	1.630
100	-	0.177	1.633
500	-	0.178	1.632
1000	-	0.178	1.631
1500	-	0.178	1.631
2000	-	0.178	1.631

As shown in Table 4.8, under conditions where the ambient temperature and hydrogen production rate are high, insufficient cooling due to a low convective heat transfer coefficient leads to hydrogen waste. For low values in the range of 5-25 $W/m^2 \cdot K$, it is observed that not all of the generated hydrogen can be stored. When h_c is set to 5 $W/m^2 \cdot K$, 0.146 kg of hydrogen remains unstored, corresponding to a waste of 49.56% relative to the total produced hydrogen of 0.295 kg. The unstored hydrogen amount decreases to 0.042 kg and 0.003 kg when h_c is 10 and 25 $W/m^2 \cdot K$, respectively, resulting in a waste of 14.28% and 1.003%. No waste was observed when the h_c value was equal to or greater than 30 $W/m^2 \cdot K$.

For the winter period, the corresponding values are presented in Table 4.9. It should be emphasized that the heat extraction term denotes the heat transferred from the metal hydride tanks to the ambient air through convection.

Table 4.9 Effect of convective heat transfer coefficient on hydrogen waste and heat extraction during winter.

h_c ($W/m^2 \cdot K$)	Waste H_2 (%)	Peak Heat Extraction Rate (kW)	Total Extracted Heat in a day (kWh)
5	-	0.031	0.942
10	-	0.061	0.929
20	-	0.113	0.926
25	-	0.136	0.919
50	-	0.149	0.910
100	-	0.148	0.903

Table 4.9 (Continued)

h_c (W/m²·K)	Waste H_2 (%)	Peak Heat Extraction Rate (kW)	Total Extracted Heat in a day (kWh)
500	-	0.147	0.897
1000	-	0.147	0.897
1500	-	0.147	0.896
2000	-	0.147	0.896

In winter, owing to the combined effects of lower hydrogen production and reduced ambient temperatures, the produced hydrogen can be fully stored under all investigated conditions.

Peak heat extraction represents the maximum heat transfer rate observed in a single tank, whereas the total extracted heat corresponds to the cumulative heat transfer from all six tanks over the course of one day. Considering both seasons (Table 4.8 and Table 4.9), increasing h_c beyond a certain threshold does not significantly affect either the peak heat extraction or the total extracted heat. In summer conditions (Table 4.8), both quantities increase with h_c due to prolonged absorption and higher thermal loads. In contrast, during winter operation (Table 4.9), although peak heat extraction increases with h_c, a slight decrease in total extracted heat is observed. It is believed that this behavior indicates faster hydrogen absorption, which shortens the overall storage duration during the day. Under summer conditions, where the number of tanks is more limited compared to winter scenarios, prolonged absorption at low h_c values leads to incomplete storage and consequently hydrogen waste.

The effect of variations in the convective heat transfer coefficient on the peak heat extraction rate and total heat extraction is presented graphically in Figure 4.31 for clearer visualization.

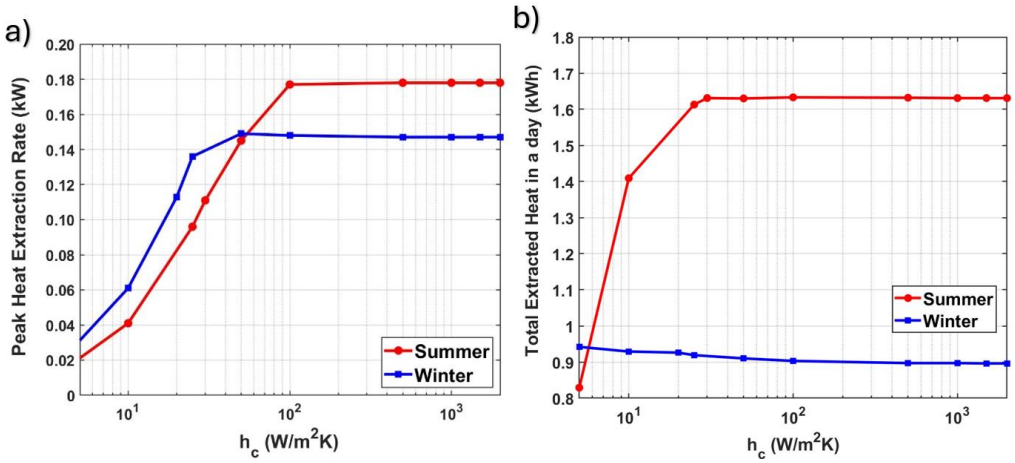

Figure 4.31 Effect of the convective heat transfer coefficient on the peak heat extraction rate and total extracted heat under summer and winter conditions

Figure 4.31a illustrates that, during winter conditions, the peak heat extraction rate stabilizes when heat transfer coefficient values exceed approximately 50 W/m^2·K. In contrast, under summer conditions, this stabilization occurs at a higher value, approximately 100 W/m^2·K. A more pronounced distinction between the two operating scenarios is evident in the total extracted heat values shown in Figure 4.31b. In summer, the total extracted heat stabilizes at an h_c value of around 30 W/m^2·K, indicating that beyond this point, further increases in h_c do not lead to additional heat transfer. In contrast, winter operation exhibits a similar trend but at a significantly lower total extracted heat level of about 0.42 kWh. It should be noted that these values are calculated over the entire day. This comparison demonstrates that the optimal heat transfer strategy is strongly dependent on seasonal operating conditions, thereby justifying the adoption of different cooling approaches for summer and winter operation.

CHAPTER FIVE
CONCLUSIONS

The 0-D mathematical model proposed in the study was established to predict the performance of PBI-based membranes in AEMWEs and to identify the main factors affecting their efficiency. The model closely aligns with experimental data in the literature and accurately reflects membrane performance under the same conditions. According to the model outcomes, at a current density of 20,000 A/m², the highest efficiency of 83.89% was achieved with the PBI/Polystyrene- P4HexPipSt/OPBI membrane, which has a thickness of 25 μm and operates at 1 M KOH at 80°C. Increasing the membrane thickness to 50 μm from 25 μm reduced the efficiency to 79.83%. The findings also indicate that different membrane structures respond differently to temperature changes. The ABPBI-c-PVBC/OH 1:2 membrane performed better at lower temperatures, such as 40°C, surpassing the P4HexPipSt/OPBI membrane by 6.36% due to its better conductivity. This will deepen the understanding of PBI membranes, enhance the model, and support progress in sustainable hydrogen production. Future research could enhance the model by validating it across a broader range of experiments and by incorporating additional factors, such as mass transport.

As part of the system-level studies, the heating profile of the stack and electrolyte tank was investigated, and the effects of inlet water flow rate, tank mass, and stack heat capacity, as well as different enthalpy calculation approaches, were further analyzed. Analyses were conducted in MATLAB and the Simulink environments. Two analytical approaches for enthalpies (Mench, 2008; NIST Chemistry WebBook, 2025) and functions derived directly from CoolProp in MATLAB were compared, where the CoolProp and NIST values showed good agreement. Stack heat capacity defines how rapidly the stack approaches thermal equilibrium; when compared under identical conditions, a higher heat capacity leads to a slower temperature increase. A lower tank mass and a slower inlet water mass flow rate cause the stack to heat up more rapidly. On the other hand, the effect of mass flow rate becomes less pronounced after a certain point.

At the end of the simulation, which lasted 3430 seconds and was performed using a heat capacity value of 100 kJ/kg, a water tank mass of 10 kg, and an inlet water flow rate of 0.05 kg/s, the stack and tank temperatures obtained from the MATLAB simulations were approximately 56°C and 54°C, respectively. Under the same operating conditions, the corresponding Simulink results were 48.5°C and 45°C. This deviation is thought to result from the addition of components, such as pipes, in the Simulink study, which align with real-world system configurations. Conducting experimental studies under various operating conditions would be valuable to determine which approach yields more reliable and accurate results.

Under typical July conditions in Izmir, the PV system achieves a maximum power output of 2.75 kW, producing a total of 19.98 kWh of electricity throughout the day. However, due to the maximum power limit of the electrolyzer (1.8 kW), a portion of the generated PV energy cannot be used for hydrogen production, resulting in approximately 16.3 kWh of usable energy for the electrolyzer over the day. Using a setup of 12 PV modules and 10 AEMWE cells, the total hydrogen production during summer is estimated at 0.2950 kg. In contrast, in January, the maximum PV output decreases to 1.46 kW, which is below the electrolyzer's power threshold. Consequently, the PV system supplies the electrolyzer continuously without any power restriction, leading to a daily production of 0.1656 kg of hydrogen. Following the production phase, the hydrogen is directed to metal hydride tanks, where the influence of the convective heat transfer coefficient on storage dynamics was evaluated for both seasonal conditions.

During the summer, hydrogen waste is observed at low convective heat transfer coefficients, ranging from 5 to 25 $W/m^2 \cdot K$, due to insufficient heat removal. The highest level of hydrogen waste occurs at a coefficient of 5 $W/m^2 \cdot K$, reaching approximately 49%. However, as the heat transfer coefficient increases to 30 $W/m^2 \cdot K$, the waste decreases to 1%. Further increases in the coefficient do not significantly enhance storage performance. In contrast, the analysis indicates that during the winter months, no hydrogen waste is observed across any of the assessed heat transfer coefficient values. This is attributed to the low hydrogen flow rate and lower ambient temperatures, which allow the tanks to operate more efficiently with fewer limitations

regarding temperature thresholds. For both seasonal scenarios, the effect of increasing the heat transfer coefficient diminishes beyond a certain threshold. Peak heat extraction stabilizes at coefficients above 100 $W/m^2 \cdot K$ in summer and above 50 $W/m^2 \cdot K$ in winter. Similarly, the total heat extracted over the day becomes insensitive to further increases in the coefficient beyond approximately 30 $W/m^2 \cdot K$ in summer, while it remains nearly constant across the entire investigated range in winter.

Future research could focus on system optimization, particularly on the configuration and coupling of the PV-EC-MH modules, as their integration can significantly influence the overall system efficiency. Furthermore, the implementation of advanced thermal management strategies coupling BoP and MH tanks could enhance cooling performance for both systems, as effective management is crucial.

REFERENCES

Abdel Haleem, A., Akutagawa, H., Nakayama, S., Bao, Y., Awaludin, Z., Nagasawa, K., Kuroda, Y., Nishiki, Y., & Mitsushima, S. (2023). Innovative membrane with selective gas permeability for alkaline water electrolysis: Dependable cell performance under industrial conditions. *Journal of Power Sources*, *587*, 233709. https://doi.org/10.1016/j.jpowsour.2023.233709

Abdi, Z. G., Chen, J. C., Chiu, T. H., Yang, H., & Yu, H. H. (2021). Synthesis of ionic polybenzimidazoles with broad ion exchange capacity range for anion exchange membrane fuel cell application. *Journal of Polymer Science*, *59*(18), 2069–2081. https://doi.org/10.1002/pol.20210409

Acevedo, Y., Prosser, J., Mcnamara, K., Huya-Kouadio Pi, J., & James, B. D. (2023). *Cost Analysis: Near-Term and Future Projections of Installation Costs for Low-Temperature Water Electrolysis*.

Agbli, K. S., Péra, M. C., Hissel, D., Rallières, O., Turpin, C., & Doumbia, I. (2011). Multiphysics simulation of a PEM electrolyser: Energetic Macroscopic Representation approach. *International Journal of Hydrogen Energy*, *36*(2), 1382–1398. https://doi.org/10.1016/j.ijhydene.2010.10.069

Aghbashlo, M., Peng, W., Tabatabaei, M., Kalogirou, S. A., Soltanian, S., Hosseinzadeh-Bandbafha, H., Mahian, O., & Lam, S. S. (2021). Machine learning technology in biodiesel research: A review. *Progress in Energy and Combustion Science*, *85*, 100904. https://doi.org/10.1016/j.pecs.2021.100904

Ahmed, K. W., Jang, M. J., Habibpour, S., Chen, Z., & Fowler, M. (2022). NiFeOx and NiFeCoOx Catalysts for Anion Exchange Membrane Water Electrolysis. *Electrochem*, *3*(4), 843–861. https://doi.org/10.3390/electrochem3040055

Alleori, R., Ancona, M. A., Bianchi, M., Falcetelli, F., Ferrari, F., Melino, F., Pilati, P., & Ricco, M. (2025). Experimental analysis on a Power-to-Hydrogen system based on PEM electrolysis and metal hydrides: Empirical correlations for optimal system design and performance improvement. *International Journal of Hydrogen Energy*, *128*, 306–318. https://doi.org/10.1016/j.ijhydene.2025.04.201

Amores, E., Rodríguez, J., & Carreras, C. (2014). Influence of operation parameters in the modeling of alkaline water electrolyzers for hydrogen production. *International Journal of Hydrogen Energy*, *39*(25), 13063–13078. https://doi.org/10.1016/j.ijhydene.2014.07.001

Aslam, S., Rani, S., Lal, K., Fatima, M., Hardwick, T., Shirinfar, B., & Ahmed, N. (2023). Electrochemical hydrogen production: sustainable hydrogen economy. *Green Chemistry*, *25*(23), 9543–9573. https://doi.org/10.1039/D3GC02849F

Awasthi, A., Scott, K., & Basu, S. (2011). Dynamic modeling and simulation of a proton exchange membrane electrolyzer for hydrogen production. *International Journal of Hydrogen Energy*, *36*(22), 14779–14786. https://doi.org/10.1016/j.ijhydene.2011.03.045

Ayers, K. E., & Marina, O. A. (2024). State of the art in low-temperature and high-temperature electrolysis. *MRS Bulletin*, *49*(12), 1226–1234. https://doi.org/10.1557/s43577-024-00806-6

Babic, U., Nilsson, E., Pătru, A., Schmidt, T. J., & Gubler, L. (2019). Proton Transport in Catalyst Layers of a Polymer Electrolyte Water Electrolyzer: Effect of the Anode Catalyst Loading. *Journal of The Electrochemical Society*, *166*(4), F214–F220. https://doi.org/10.1149/2.0341904jes

Bazarah, A., Majlan, E. H., Husaini, T., Zainoodin, A. M., Alshami, I., Goh, J., & Masdar, M. S. (2022). Factors influencing the performance and durability of polymer electrolyte membrane water electrolyzer: A review. In *International Journal of Hydrogen Energy* (Vol. 47, Issue 85, pp. 35976–35989). Elsevier Ltd. https://doi.org/10.1016/j.ijhydene.2022.08.180

Bernäcker, C. I., Rauscher, T., Büttner, T., Kieback, B., & Röntzsch, L. (2019). A Powder Metallurgy Route to Produce Raney-Nickel Electrodes for Alkaline Water Electrolysis. *Journal of The Electrochemical Society*, *166*(6), F357–F363. https://doi.org/10.1149/2.0851904jes

Beyrami, J., Nakashima, R. N., Nemati, A., & Frandsen, H. L. (2025). Lifetime and performance of solid oxide electrolysis stacks and systems under different

operation modes and conditions. *International Journal of Hydrogen Energy*, *102*, 980–995. https://doi.org/10.1016/j.ijhydene.2025.01.028

Bhogilla, S., Pandoh, A., & Singh, U. R. (2024). Cogeneration system combining reversible PEM fuel cell, and metal hydride hydrogen storage enabling renewable energy storage: Thermodynamic performance assessment. *International Journal of Hydrogen Energy*, *52*, 1147–1155. https://doi.org/10.1016/j.ijhydene.2023.08.028

Bin, S., Chen, Z., Zhu, Y., Zhang, Y., Xia, Y., Gong, S., Zhang, F., Shi, L., Duan, X., & Sun, Z. (2024). High-pressure proton exchange membrane water electrolysis: Current status and challenges in hydrogen production. *International Journal of Hydrogen Energy*, *67*, 390–405. https://doi.org/10.1016/j.ijhydene.2024.04.188

Boström, O., Choi, S.-Y., Xia, L., Meital, S., Lohmann-Richters, F., & Jannasch, P. (2023). Alkali-stable polybenzimidazole anion exchange membranes tethered with *N* , *N* -dimethylpiperidinium cations for dilute aqueous KOH fed water electrolyzers. *Journal of Materials Chemistry A*, *11*(39), 21170–21182. https://doi.org/10.1039/D3TA03216G

Brauns, J., Schönebeck, J., Kraglund, M. R., Aili, D., Hnát, J., Žitka, J., Mues, W., Jensen, J. O., Bouzek, K., & Turek, T. (2021). Evaluation of Diaphragms and Membranes as Separators for Alkaline Water Electrolysis. *Journal of The Electrochemical Society*, *168*(1), 014510. https://doi.org/10.1149/1945-7111/abda57

Büsch, L., Jakschik, M., Syniawa, D., Masuhr, C., Christ, L., Schachtsiek, J., Haalck, K., Nerlich, L., Frömsdorf, E., Schirmack, N., Ebert, B., Kirty, C., Adler, P., Schüppstuhl, T., & Kuhlenkötter, B. (2024). HyPLANT100: Industrialization from Assembly to the Construction Site for Gigawatt Electrolysis. *Hydrogen*, *5*(2), 185–208. https://doi.org/10.3390/hydrogen5020012

Campagna Zignani, S., Faro, M. Lo, Carbone, A., Italiano, C., Trocino, S., Monforte, G., & Aricò, A. S. (2022). Performance and stability of a critical raw materials-

free anion exchange membrane electrolysis cell. *Electrochimica Acta*, *413*, 140078. https://doi.org/10.1016/j.electacta.2022.140078

Carmo, M., Fritz, D. L., Mergel, J., & Stolten, D. (2013). A comprehensive review on PEM water electrolysis. *International Journal of Hydrogen Energy*, *38*(12), 4901–4934. https://doi.org/10.1016/j.ijhydene.2013.01.151

Cavaliere, P. (2023). *Water Electrolysis for Hydrogen Production*. Springer International Publishing. https://doi.org/10.1007/978-3-031-37780-8

Chen, B., Mardle, P., & Holdcroft, S. (2022). Probing the effect of ionomer swelling on the stability of anion exchange membrane water electrolyzers. *Journal of Power Sources*, *550*. https://doi.org/10.1016/j.jpowsour.2022.232134

Chen, C., Tse, Y.-L. S., Lindberg, G. E., Knight, C., & Voth, G. A. (2016). Hydroxide Solvation and Transport in Anion Exchange Membranes. *Journal of the American Chemical Society*, *138*(3), 991–1000. https://doi.org/10.1021/jacs.5b11951

Chen, G., Wang, T., Zhang, J., Liu, P., Sun, H., Zhuang, X., Chen, M., & Feng, X. (2018). Accelerated Hydrogen Evolution Kinetics on NiFe-Layered Double Hydroxide Electrocatalysts by Tailoring Water Dissociation Active Sites. *Advanced Materials*, *30*(10). https://doi.org/10.1002/adma.201706279

Chen, J. P., Chang, S.-Y., & Hung, Y.-T. (2005). Electrolysis. In *Physicochemical Treatment Processes* (pp. 359–378). Humana Press. https://doi.org/10.1385/1-59259-820-x:359

Chen, J., Shen, C., Wang, H., & Gao, S. (2025). β-H-free alkyl ether chains: Enhancing alkaline stability and optimizing phase-separated structures in poly(aryl piperidine) anion exchange membrane. *Journal of Power Sources*, *658*, 238173. https://doi.org/10.1016/j.jpowsour.2025.238173

Chen, J., Wang, S., Sun, Y., Zhang, C., & Lv, H. (2025). Multi-dimensional performance evaluation and energy analysis of proton exchange membrane water electrolyzer. *Applied Energy*, *377*, 124457. https://doi.org/10.1016/j.apenergy.2024.124457

Chen, M., Zheng, L., Santra, B., Ko, H.-Y., DiStasio Jr, R. A., Klein, M. L., Car, R., & Wu, X. (2018). Hydroxide diffuses slower than hydronium in water because its solvated structure inhibits correlated proton transfer. *Nature Chemistry*, *10*(4), 413–419. https://doi.org/10.1038/s41557-018-0010-2

Cheng, L., Guo, Z., & Xia, G. (2024). A Review on Research and Technology Development of Green Hydrogen Energy Systems with Thermal Management and Heat Recovery. *Heat Transfer Engineering*, *45*(4–5), 300–322. https://doi.org/10.1080/01457632.2023.2191435

Chiu, T.-H., Huang, S.-W., & Chen, J.-C. (2025). Polybenzimidazoles crosslinked by alkyne-azide cycloaddition for anion exchange membrane fuel cell application. *Journal of Polymer Research*, *32*(9), 321. https://doi.org/10.1007/s10965-025-04560-4

Choi, K. J., Kim, H., & Kim, S.-K. (2021). Multicomponent nonprecious hydrogen evolution catalysts for high performance and durable proton exchange membrane water electrolyzer. *Journal of Power Sources*, *506*, 230200. https://doi.org/10.1016/j.jpowsour.2021.230200

Cooper, N., Horend, C., Röben, F., Bardow, A., & Shah, N. (2022). A framework for the design & operation of a large-scale wind-powered hydrogen electrolyzer hub. *International Journal of Hydrogen Energy*, *47*(14), 8671–8686. https://doi.org/10.1016/j.ijhydene.2021.12.225

Coppola, R. E., Herranz, D., Escudero-Cid, R., Ming, N., D'Accorso, N. B., Ocón, P., & Abuin, G. C. (2020). Polybenzimidazole-crosslinked-poly(vinyl benzyl chloride) as anion exchange membrane for alkaline electrolyzers. *Renewable Energy*, *157*, 71–82. https://doi.org/10.1016/j.renene.2020.04.140

Crespi, E., Guandalini, G., Mastropasqua, L., Campanari, S., & Brouwer, J. (2023). Experimental and theoretical evaluation of a 60 kW PEM electrolysis system for flexible dynamic operation. *Energy Conversion and Management*, *277*, 116622. https://doi.org/10.1016/j.enconman.2022.116622

Dang, J., Li, Y., Liu, B., Hu, S., Yang, F., & Ouyang, M. (2023). Design and economic analysis of high-pressure proton exchange membrane electrolysis for renewable energy storage. *International Journal of Hydrogen Energy*, *48*(28), 10377–10393. https://doi.org/10.1016/j.ijhydene.2022.11.250

de Groot, M. T., & Vreman, A. W. (2021). Ohmic resistance in zero gap alkaline electrolysis with a Zirfon diaphragm. *Electrochimica Acta*, *369*, 137684. https://doi.org/10.1016/j.electacta.2020.137684

Ding, G., Lee, H., Li, Z., Du, J., Wang, L., Chen, D., & Sun, L. (2023). Highly Efficient and Durable Anion Exchange Membrane Water Electrolyzer Enabled by a Fe–Ni3S2 Anode Catalyst. *Advanced Energy and Sustainability Research*, *4*(1). https://doi.org/10.1002/aesr.202200130

Ding, S., Guo, B., Hu, S., Gu, J., Yang, F., Li, Y., Dang, J., Liu, B., & Ma, J. (2022). Analysis of the effect of characteristic parameters and operating conditions on exergy efficiency of alkaline water electrolyzer. *Journal of Power Sources*, *537*, 231532. https://doi.org/10.1016/j.jpowsour.2022.231532

Dionigi, F., & Strasser, P. (2016). NiFe-Based (Oxy)hydroxide Catalysts for Oxygen Evolution Reaction in Non-Acidic Electrolytes. *Advanced Energy Materials*, *6*(23). https://doi.org/10.1002/aenm.201600621

Disli, T., Çetinkaya, S. A., Ezan, M. A., & Colpan, C. O. (2024). Numerical investigations on the absorption of a metal hydride hydrogen storage tank based on various thermal management strategies. *International Journal of Hydrogen Energy*, *51*, 504–522. https://doi.org/10.1016/j.ijhydene.2023.07.122

Dong, D., Wei, X., Hooper, J. B., Pan, H., & Bedrov, D. (2018). Role of cationic groups on structural and dynamical correlations in hydrated quaternary ammonium-functionalized poly(*p* -phenylene oxide)-based anion exchange membranes. *Physical Chemistry Chemical Physics*, *20*(29), 19350–19362. https://doi.org/10.1039/C8CP02211A

Dong, D., Zhang, W., van Duin, A. C. T., & Bedrov, D. (2018). Grotthuss versus Vehicular Transport of Hydroxide in Anion-Exchange Membranes: Insight from

Combined Reactive and Nonreactive Molecular Simulations. *The Journal of Physical Chemistry Letters*, *9*(4), 825–829. https://doi.org/10.1021/acs.jpclett.8b00004

Du, N., Roy, C., Peach, R., Turnbull, M., Thiele, S., & Bock, C. (2022). Anion-Exchange Membrane Water Electrolyzers. *Chemical Reviews*, *122*(13), 11830–11895. https://doi.org/10.1021/acs.chemrev.1c00854

Du, Y., Ling, H., Zhao, L., Jiang, H., Kong, J., Liu, P., & Zhou, T. (2024). The development of solid oxide electrolysis cells: Critical materials, technologies and prospects. *Journal of Power Sources*, *607*, 234608. https://doi.org/10.1016/j.jpowsour.2024.234608

Dubey, V., & Daschakraborty, S. (2022). Translational Jump-Diffusion of Hydroxide Ion in Anion Exchange Membrane: Deciphering the Nature of Vehicular Diffusion. *The Journal of Physical Chemistry B*, *126*(12), 2430–2440. https://doi.org/10.1021/acs.jpcb.2c00240

Dubey, V., Maiti, A., & Daschakraborty, S. (2020). Predicting the solvation structure and vehicular diffusion of hydroxide ion in an anion exchange membrane using nonreactive molecular dynamics simulation. *Chemical Physics Letters*, *755*, 137802. https://doi.org/10.1016/j.cplett.2020.137802

Ďurovič, M., Hnát, J., & Bouzek, K. (2021). Electrocatalysts for the hydrogen evolution reaction in alkaline and neutral media. A comparative review. *Journal of Power Sources*, *493*, 229708. https://doi.org/10.1016/j.jpowsour.2021.229708

Ehlers, J. C., Feidenhans'l, A. A., Therkildsen, K. T., & Larrazábal, G. O. (2023). Affordable Green Hydrogen from Alkaline Water Electrolysis: Key Research Needs from an Industrial Perspective. In *ACS Energy Letters* (Vol. 8, Issue 3, pp. 1502–1509). American Chemical Society. https://doi.org/10.1021/acsenergylett.2c02897

Emonts, B., Müller, M., Hehemann, M., Janßen, H., Keller, R., Stähler, M., Stähler, A., Hagenmeyer, V., Dittmeyer, R., Pfeifer, P., Waczowicz, S., Rubin, M., Munzke, N., & Kasselmann, S. (2022). A Holistic Consideration of Megawatt

Electrolysis as a Key Component of Sector Coupling. *Energies*, *15*(10), 3656. https://doi.org/10.3390/en15103656

Endo, N., Goshome, K., Tetsuhiko, M., Segawa, Y., Shimoda, E., & Nozu, T. (2021). Thermal management and power saving operations for improved energy efficiency within a renewable hydrogen energy system utilizing metal hydride hydrogen storage. *International Journal of Hydrogen Energy*, *46*(1), 262–271. https://doi.org/10.1016/j.ijhydene.2020.10.002

Endo, N., Shimoda, E., Goshome, K., Yamane, T., Nozu, T., & Maeda, T. (2019). Construction and operation of hydrogen energy utilization system for a zero emission building. *International Journal of Hydrogen Energy*, *44*(29), 14596–14604. https://doi.org/10.1016/j.ijhydene.2019.04.107

Endrődi, B., Trapp, C. A., Szén, I., Bakos, I., Lukovics, M., & Janáky, C. (2025). Challenges and Opportunities of the Dynamic Operation of PEM Water Electrolyzers. *Energies*, *18*(9), 2154. https://doi.org/10.3390/EN18092154/S1

Espinosa-López, M., Darras, C., Poggi, P., Glises, R., Baucour, P., Rakotondrainibe, A., Besse, S., & Serre-Combe, P. (2018). Modelling and experimental validation of a 46 kW PEM high pressure water electrolyzer. *Renewable Energy*, *119*, 160–173. https://doi.org/10.1016/j.renene.2017.11.081

Fahr, S., Engel, F. K., Rehfeldt, S., Peschel, A., & Klein, H. (2024). Overview and evaluation of crossover phenomena and mitigation measures in proton exchange membrane (PEM) electrolysis. *International Journal of Hydrogen Energy*, *68*, 705–721. https://doi.org/10.1016/j.ijhydene.2024.04.248

Faid, A. Y., Barnett, A. O., Seland, F., & Sunde, S. (2021). Tuning Ni–MoO_2 Catalyst–Ionomer and Electrolyte Interaction for Water Electrolyzers with Anion Exchange Membranes. *ACS Applied Energy Materials*, *4*(4), 3327–3340. https://doi.org/10.1021/acsaem.0c03072

Faid, A. Y., Barnett, A. O., Seland, F., & Sunde, S. (2022). Ternary NiCoFe nanosheets for oxygen evolution in anion exchange membrane water electrolysis.

International Journal of Hydrogen Energy, *47*(56), 23483–23497. https://doi.org/10.1016/j.ijhydene.2022.05.143

Feng, Q., Yuan, X., Liu, G., Wei, B., Zhang, Z., Li, H., & Wang, H. (2017). A review of proton exchange membrane water electrolysis on degradation mechanisms and mitigation strategies. *Journal of Power Sources*, *366*, 33–55. https://doi.org/10.1016/j.jpowsour.2017.09.006

Firouz Tadavani, K., Abdolmaleki, A., Najafi Fath Dehghan, H., Molavian, M. R., & Zhiani, M. (2023). Multication Anion Exchange Membranes with Robust Chemical Stability and High Conductivity: Effect of the Equatorial Position on Membrane Alkaline Stability. *ACS Applied Energy Materials*, *6*(19), 9864–9874. https://doi.org/10.1021/acsaem.3c01202

Fortin, P., Khoza, T., Cao, X., Martinsen, S. Y., Oyarce Barnett, A., & Holdcroft, S. (2020). High-performance alkaline water electrolysis using Aemion™ anion exchange membranes. *Journal of Power Sources*, *451*, 227814. https://doi.org/10.1016/j.jpowsour.2020.227814

Galkina, I., Faid, A. Y., Jiang, W., Scheepers, F., Borowski, P., Sunde, S., Shviro, M., Lehnert, W., & Mechler, A. K. (2024). Stability of Ni–Fe-Layered Double Hydroxide Under Long-Term Operation in AEM Water Electrolysis. *Small*, *20*(26). https://doi.org/10.1002/smll.202311047

Gallandat, N., Romanowicz, K., & Züttel, A. (2017). An Analytical Model for the Electrolyser Performance Derived from Materials Parameters. *Journal of Power and Energy Engineering*, *05*(10), 34–49. https://doi.org/10.4236/jpee.2017.510003

García-Valverde, R., Espinosa, N., & Urbina, A. (2012). Simple PEM water electrolyser model and experimental validation. *International Journal of Hydrogen Energy*, *37*(2), 1927–1938. https://doi.org/10.1016/j.ijhydene.2011.09.027

Gatto, I., Caprì, A., Lo Vecchio, C., Zignani, S., Patti, A., & Baglio, V. (2023). Optimal operating conditions evaluation of an anion-exchange-membrane

electrolyzer based on FUMASEP® FAA3-50 membrane. *International Journal of Hydrogen Energy*, *48*(32), 11914–11921. https://doi.org/10.1016/j.ijhydene.2022.04.176

Ghosh, A. (2025). Solar-Powered Green Hydrogen from Electrolyzer (PV-H2): A Review. *Solar RRL*, *9*(14). https://doi.org/10.1002/SOLR.202500150

Gladik, A., Riedel, M., & Eichel, R.-A. (2025). Anion exchange membrane electrolysis at work—Investigating impact of starting parameters and start–stop operation on cold start behavior and degradation. *Journal of Power Sources*, *628*, 235878. https://doi.org/10.1016/j.jpowsour.2024.235878

Gomez Vidales, A., Millan, N. C., & Bock, C. (2023). Modeling of anion exchange membrane water electrolyzers: The influence of operating parameters. *Chemical Engineering Research and Design*, *194*, 636–648. https://doi.org/10.1016/j.cherd.2023.05.004

Green Industrial Hydrogen via steam electrolysis. (2019). https://doi.org/10.3030/826350

Guo, M., Ban, T., Wang, Y., Wang, X., Wang, Z., & Zhu, X. (2023). Polybenzimidazoles incorporating imidazole N-spirocyclic quaternary ammonium cation for anion exchange membranes water electrolysis. *Journal of Membrane Science*, *684*. https://doi.org/10.1016/j.memsci.2023.121903

Guo, M., Ban, T., Wang, Y., Wang, Y., Zhang, Y., Zhang, J., & Zhu, X. (2022). Exploring highly soluble ether-free polybenzimidazole as anion exchange membranes with long term durability. *Journal of Membrane Science*, *647*, 120299. https://doi.org/10.1016/j.memsci.2022.120299

Guo, M., Wang, Z., Xu, Y., & Zhu, X. (2024). Vinyl-based in-situ crosslinked polybenzimidazoles for anion exchange membranes water electrolysis. *Journal of Membrane Science*, *707*, 123026. https://doi.org/10.1016/j.memsci.2024.123026

Hager, L., Hegelheimer, M., Stonawski, J., Freiberg, A. T. S., Jaramillo-Hernández, C., Abellán, G., Hutzler, A., Böhm, T., Thiele, S., & Kerres, J. (2023). Novel side chain functionalized polystyrene/O-PBI blends with high alkaline stability for anion exchange membrane water electrolysis (AEMWE). *Journal of Materials Chemistry A*, *11*(41), 22347–22359. https://doi.org/10.1039/d3ta02978f

Hammi, Z., Labjar, N., Lotf, E. M., & Hajjaji, S. El. (2023). Production of Green Hydrogen Employing Proton Exchange Membrane Water Electrolyzer: Characterization of Electrolyte Membrane. A Critical Review. In *Journal of Membrane Science and Research* (Vol. 9, Issue 3). Amirkabir University of Technology - Membrane Processes Research Laboratory. https://doi.org/10.22079/JMSR.2023.1978109.1579

Han, J., Zhu, L., Pan, J., Zimudzi, T. J., Wang, Y., Peng, Y., Hickner, M. A., & Zhuang, L. (2017). Elastic Long-Chain Multication Cross-Linked Anion Exchange Membranes. *Macromolecules*, *50*(8), 3323–3332. https://doi.org/10.1021/acs.macromol.6b01140

Han, S., Ryu, J. H., Lee, W. B., Ryu, J., & Yoon, J. (2024). Translating the Optimized Durability of Co-Based Anode Catalyst into Sustainable Anion Exchange Membrane Water Electrolysis. *Small*, *20*(27). https://doi.org/10.1002/smll.202311052

Han, X., Suo, N., Chen, C., Lin, Z., Dou, Z., He, X., & Cui, L. (2019). Graphene oxide guiding the constructing of nickel-iron layered double hydroxides arrays as a desirable bifunctional electrocatalyst for HER and OER. *International Journal of Hydrogen Energy*, *44*(57), 29876–29888. https://doi.org/10.1016/j.ijhydene.2019.09.116

He, D., Chen, K., Chen, W., Luo, Z., Xiong, Z., Zou, G., Li, G., & Chen, B. (2025). Experimental study on the degradation of proton exchange membrane water electrolyzers under different dynamic loads and flow field configurations. *Journal of Power Sources*, *641*, 236844. https://doi.org/10.1016/j.jpowsour.2025.236844

Heavy Metal Debut: A World-Class Metal Hydride System | NREL. (n.d.). Retrieved October 12, 2025, from https://www.nrel.gov/news/detail/program/2024/heavy-metal-debut-a-world-class-metal-hydride-system

Hellström, M., Quaranta, V., & Behler, J. (2019). One-dimensional *vs.* two-dimensional proton transport processes at solid–liquid zinc-oxide–water interfaces. *Chemical Science*, *10*(4), 1232–1243. https://doi.org/10.1039/C8SC03033B

Henao, C., Agbossou, K., Hammoudi, M., Dubé, Y., & Cardenas, A. (2014). Simulation tool based on a physics model and an electrical analogy for an alkaline electrolyser. *Journal of Power Sources*, *250*, 58–67. https://doi.org/10.1016/j.jpowsour.2013.10.086

Henkensmeier, D., Cho, W.-C., Jannasch, P., Stojadinovic, J., Li, Q., Aili, D., & Jensen, J. O. (2024). Separators and Membranes for Advanced Alkaline Water Electrolysis. *Chemical Reviews*, *124*(10), 6393–6443. https://doi.org/10.1021/acs.chemrev.3c00694

Hong, D.-G., Park, H., Choi, Y., Lee, S. H., Hwang, H. J., Park, S., & Kim, S.-D. (2026). 1,000-hour life testing of 10-cell planar solid oxide electrolysis cell stacks at 650 °C: Effects of bipolar plate coatings on degradation suppression. *Journal of Power Sources, 661*, 238576. https://doi.org/10.1016/j.jpowsour.2025.238576

Hota, P., Das, A., & Maiti, D. K. (2023). A short review on generation of green fuel hydrogen through water splitting. *International Journal of Hydrogen Energy*, *48*(2), 523–541. https://doi.org/10.1016/j.ijhydene.2022.09.264

Hou, D., Qiao, G., Liu, L., Zhang, X., Yan, Y., & Du, S. (2025). Challenges in scaling up testing of catalyst coated membranes for proton exchange membrane water electrolyzers. *Frontiers in Energy Research*, *13*. https://doi.org/10.3389/fenrg.2025.1557069

Hu, C., Kang, H. W., Jung, S. W., Liu, M., Lee, Y. J., Park, J. H., Kang, N. Y., Kim, M., Yoo, S. J., Park, C. H., & Lee, Y. M. (2024). High Free Volume Polyelectrolytes for Anion Exchange Membrane Water Electrolyzers with a

Current Density of 13.39 A cm $^{-2}$ and a Durability of 1000 h. *Advanced Science*, *11*(5). https://doi.org/10.1002/advs.202306988

Hu, X., Huang, Y., Liu, L., Ju, Q., Zhou, X., Qiao, X., Zheng, Z., & Li, N. (2021). Piperidinium functionalized aryl ether-free polyaromatics as anion exchange membrane for water electrolysers: Performance and durability. *Journal of Membrane Science*, *621*, 118964. https://doi.org/10.1016/j.memsci.2020.118964

Huang, M., Tao, J., Ma, L., Zhuang, X., Wang, H., Bing Tao, H., & Zheng, N. (2024). Is it stable for the asymmetric pressure operation of PEM water Electrolyzer? *Chemical Engineering Journal*, *498*, 155209. https://doi.org/10.1016/j.cej.2024.155209

Hydrogen Production Cost by AEM Water Electrolysis, Document ID: FM-7024-B. (2020). www.ionomr.com

Hyun, J., & Kim, H.-T. (2020). Impact of Solvent on Catalyst Layer for Anion Exchange Membrane Fuel Cell. *ECS Meeting Abstracts*, *MA2020-02*(37), 2370–2370. https://doi.org/10.1149/MA2020-02372370mtgabs

IEA. (2025). *Global Hydrogen Review 2025*. www.iea.org

Ikhsan, M. M., Yang, C., Ghotia, K., Egert, F., Ansar, S.-A., Żurowska, O., Rózga, M., Michalak, A., Kraglund, M. R., Aili, D., Park, H. S., Razmjooei, F., & Henkensmeier, D. (2025). Sulfonated polybenzimidazole for low-alkalinity ion solvating membrane water electrolysis. *Nature Energy*. https://doi.org/10.1038/s41560-025-01876-9

Incropera, F. P., DeWitt, D. P., Bergman, T. L., & Lavine, A. S. (2006). *Fundamentals of heat and mass transfer (6th ed.). John Wiley & Sons*.

International Renewable Energy Agency (IRENA). (2020). *Green Hydrogen Cost Reduction: Scaling up electrolysers to meet the 1.5°C climate goal*. www.irena.org/publications

Ito, H., Wang, R., Hirose, R., Kageyama, A., Ishida, M., & Ohashi, M. (2023). Cathode Dry Operation of Anion Exchange Membrane Water Electrolysis. *ECS Meeting*

Abstracts, *MA2023-01*(36), 2083–2083. https://doi.org/10.1149/MA2023-01362083mtgabs

James, B. D., Acevedo, Y. M., Mcnamara, K. R., Prosser, J. H., & Huya-Kouadio, J. M. (2024). *Hydrogen Production Cost with Anion Exchange Membrane Electrolysis*. www.sainc.com

Jang, D., Cho, H.-S., & Kang, S. (2021). Numerical modeling and analysis of the effect of pressure on the performance of an alkaline water electrolysis system. *Applied Energy*, *287*, 116554. https://doi.org/10.1016/j.apenergy.2021.116554

Jensen, M. Ø., Röthlisberger, U., & Rovira, C. (2005). Hydroxide and Proton Migration in Aquaporins. *Biophysical Journal*, *89*(3), 1744–1759. https://doi.org/10.1529/biophysj.104.058206

Jheng, L. cheng, Hsu, S. L. chung, Lin, B. yun, & Hsu, Y. lun. (2014). Quaternized polybenzimidazoles with imidazolium cation moieties for anion exchange membrane fuel cells. *Journal of Membrane Science*, *460*, 160–170. https://doi.org/10.1016/j.memsci.2014.02.043

Jiang, B., Liu, S., Cheng, L., Zhou, L., Cui, H., Liu, M., Wen, M., Wang, C., Wang, W., Li, S., & Sun, X. (2024). Mass synthesis of Pt/C catalysts with high Pt loading for low-overpotential hydrogen evolution. *International Journal of Hydrogen Energy*, *58*, 268–278. https://doi.org/10.1016/j.ijhydene.2024.01.183

Jin, H., Ruqia, B., Park, Y., Kim, H. J., Oh, H. S., Choi, S. Il, & Lee, K. (2021). Nanocatalyst Design for Long-Term Operation of Proton/Anion Exchange Membrane Water Electrolysis. In *Advanced Energy Materials* (Vol. 11, Issue 4). Wiley-VCH Verlag. https://doi.org/10.1002/aenm.202003188

Jolaoso, L. A., Bello, I. T., Ojelade, O. A., Yousuf, A., Duan, C., & Kazempoor, P. (2023). Operational and scaling-up barriers of SOEC and mitigation strategies to boost H2 production- a comprehensive review. *International Journal of Hydrogen Energy*, *48*(85), 33017–33041. https://doi.org/10.1016/j.ijhydene.2023.05.077

JRC Photovoltaic Geographical Information System (PVGIS) - European Commission. (n.d.). Retrieved November 12, 2025, from https://re.jrc.ec.europa.eu/pvg_tools/en/

Kang, Z., Pak, M., & Bender, G. (2021). Introducing a novel technique for measuring hydrogen crossover in membrane-based electrochemical cells. *International Journal of Hydrogen Energy*, *46*(29), 15161–15167. https://doi.org/10.1016/j.ijhydene.2021.02.054

Karas, F., Hnát, J., Paidar, M., Schauer, J., & Bouzek, K. (2014). Determination of the ion-exchange capacity of anion-selective membranes. *International Journal of Hydrogen Energy*, *39*(10), 5054–5062. https://doi.org/10.1016/j.ijhydene.2014.01.074

Karibayev, M., Kalybekkyzy, S., Wang, Y., & Mentbayeva, A. (2022). Molecular Modeling in Anion Exchange Membrane Research: A Brief Review of Recent Applications. *Molecules*, *27*(11), 3574. https://doi.org/10.3390/molecules27113574

Khalid, H., Najibah, M., Park, H. S., Bae, C., & Henkensmeier, D. (2022). *membranes Properties of Anion Exchange Membranes with a Focus on Water Electrolysis*. https://doi.org/10.3390/membranes

Khalid Ratib, M., M. Muttaqi, K., Islam, M. R., Sutanto, D., & Agalgaonkar, A. P. (2024). Electrical circuit modeling of proton exchange membrane electrolyzer: The state-of-the-art, current challenges, and recommendations. *International Journal of Hydrogen Energy*, *49*, 625–645. https://doi.org/10.1016/j.ijhydene.2023.08.319

Kiessling, A., Fornaciari, J. C., Anderson, G., Peng, X., Gerstmayr, A., Gerhardt, M. R., McKinney, S., Serov, A., Kim, Y. S., Zulevi, B., Weber, A. Z., & Danilovic, N. (2021). Influence of Supporting Electrolyte on Hydroxide Exchange Membrane Water Electrolysis Performance: Anolyte. *Journal of The Electrochemical Society*, *168*(8), 084512. https://doi.org/10.1149/1945-7111/ac1dcd

Kim, M., Lee, D., Qi, M., & Kim, J. (2024). Techno-economic analysis of anion exchange membrane electrolysis process for green hydrogen production under uncertainty. *Energy Conversion and Management*, *302*, 118134. https://doi.org/10.1016/j.enconman.2024.118134

Koch, S., Disch, J., Kilian, S. K., Han, Y., Metzler, L., Tengattini, A., Helfen, L., Schulz, M., Breitwieser, M., & Vierrath, S. (2022). Water management in anion-exchange membrane water electrolyzers under dry cathode operation. *RSC Advances*, *12*(32), 20778–20784. https://doi.org/10.1039/D2RA03846C

Kriston, Á., Xie, T., Gamliel, D., Ganesan, P., & Popov, B. N. (2013). Effect of ultra-low Pt loading on mass activity of polymer electrolyte membrane fuel cells. *Journal of Power Sources*, *243*, 958–963. https://doi.org/10.1016/j.jpowsour.2013.05.078

Krivina, R. A., Lindquist, G. A., Beaudoin, S. R., Stovall, T. N., Thompson, W. L., Twight, L. P., Marsh, D., Grzyb, J., Fabrizio, K., Hutchison, J. E., & Boettcher, S. W. (2022). Anode Catalysts in Anion-Exchange-Membrane Electrolysis without Supporting Electrolyte: Conductivity, Dynamics, and Ionomer Degradation. *Advanced Materials*, *34*(35). https://doi.org/10.1002/adma.202203033

Kulkarni, M. P., Thomas, O. D., Peckham, T. J., & Holdcroft, S. (2012). High ion exchange capacity, sulfonated polybenzimidazoles. *ACS Symposium Series*, *1096*, 221–231. https://doi.org/10.1021/bk-2012-1096.ch013

Kumar, K., Alam, M., & Dutta, V. (2019). Techno-economic analysis of metal hydride-based energy storage system in microgrid. *Energy Storage*, *1*(3). https://doi.org/10.1002/est2.62

Kumar, N., Lee, S. Y., & Park, S. J. (2024). Advancements in hydrogen storage technologies: A comprehensive review of materials, methods, and economic policy. In *Nano Today* (Vol. 56). Elsevier B.V. https://doi.org/10.1016/j.nantod.2024.102302

Lamy, C. (2016). From hydrogen production by water electrolysis to its utilization in a PEM fuel cell or in a SO fuel cell: Some considerations on the energy efficiencies. *International Journal of Hydrogen Energy*, *41*(34), 15415–15425. https://doi.org/10.1016/j.ijhydene.2016.04.173

LBE-20C (Alkaline Water Electrolyzer Large Stack - 20 Cell). (n.d.). Retrieved October 15, 2025, from https://www.fuelcellstore.com/alkaline-water-electrolyzer-stack-20-cell

Lee, D., Kim, M., Kim, J., Moon, I., & Kim, J. (2024). Advanced CFD simulation of two-phase anion exchange membrane water electrolysis. *International Journal of Hydrogen Energy*, *88*, 322–332. https://doi.org/10.1016/j.ijhydene.2024.09.180

Lee, J. Y., Choi, Y. Bin, Lee, H. J., Lim, K. H., Park, H.-Y., Jang, J. H., & Lee, S. Y. (2025). Optimized structure of asymmetric polybenzimidazole membranes to improve anion exchange membrane water electrolysis performance. *Materials Today Energy*, *48*, 101755. https://doi.org/10.1016/j.mtener.2024.101755

Lee, J. Y., Lim, D. H., Chae, J. E., Choi, J., Kim, B. H., Lee, S. Y., Yoon, C. W., Nam, S. Y., Jang, J. H., Henkensmeier, D., Yoo, S. J., Kim, J. Y., Kim, H. J., & Ham, H. C. (2016). Base tolerant polybenzimidazolium hydroxide membranes for solid alkaline-exchange membrane fuel cells. *Journal of Membrane Science*, *514*, 398–406. https://doi.org/10.1016/j.memsci.2016.05.012

Lee, S. A., Kim, J., Kwon, K. C., Park, S. H., & Jang, H. W. (2022). Anion exchange membrane water electrolysis for sustainable large-scale hydrogen production. *Carbon Neutralization*, *1*(1), 26–48. https://doi.org/10.1002/cnl2.9

Lei, J., Wang, Z., Zhang, Y., Ju, M., Fei, H., Wang, S., Fu, C., Yuan, X., Fu, Q., Farid, M. U., Kong, H., An, A. K., Deng, R., Liu, F., & Wang, J. (2024). Understanding and resolving the heterogeneous degradation of anion exchange membrane water electrolysis for large-scale hydrogen production. *Carbon Neutrality 2024 3:1*, *3*(1), 1–24. https://doi.org/10.1007/S43979-024-00101-Y

Lei, L., Zhang, J., Yuan, Z., Liu, J., Ni, M., & Chen, F. (2019). Progress Report on Proton Conducting Solid Oxide Electrolysis Cells. *Advanced Functional Materials*, *29*(37). https://doi.org/10.1002/adfm.201903805

León, M. I., Valentín-Reyes, J., Romero-Castañón, T., Beltrán, J., Flores-Hernández, J. R., & Nava, J. L. (2022). Water movement through an anion exchange membrane fuel cell (AEMFC): Influence of gas humidity and flow rate. *Applied Energy*, *324*, 119722. https://doi.org/10.1016/j.apenergy.2022.119722

Li, C., & Baek, J. B. (2020). Recent Advances in Noble Metal (Pt, Ru, and Ir)-Based Electrocatalysts for Efficient Hydrogen Evolution Reaction. In *ACS Omega* (Vol. 5, Issue 1, pp. 31–40). American Chemical Society. https://doi.org/10.1021/acsomega.9b03550

Li, C., & Baek, J.-B. (2021). The promise of hydrogen production from alkaline anion exchange membrane electrolyzers. *Nano Energy*, *87*, 106162. https://doi.org/10.1016/j.nanoen.2021.106162

Li, D., Motz, A. R., Bae, C., Fujimoto, C., Yang, G., Zhang, F.-Y., Ayers, K. E., & Kim, Y. S. (2021). Durability of anion exchange membrane water electrolyzers. *Energy & Environmental Science*, *14*(6), 3393–3419. https://doi.org/10.1039/D0EE04086J

Li, D., Park, E. J., Zhu, W., Shi, Q., Zhou, Y., Tian, H., Lin, Y., Serov, A., Zulevi, B., Baca, E. D., Fujimoto, C., Chung, H. T., & Kim, Y. S. (2020). Highly quaternized polystyrene ionomers for high performance anion exchange membrane water electrolysers. *Nature Energy*, *5*(5), 378–385. https://doi.org/10.1038/s41560-020-0577-x

Li, F., Chan, S. H., & Tu, Z. (2024). Recent Development of Anion Exchange Membrane Fuel Cells and Performance Optimization Strategies: A Review. *The Chemical Record*, *24*(1). https://doi.org/10.1002/tcr.202300067

Li, H., Zhang, C., Xiang, W., Amin, M. A., Na, J., Wang, S., Yu, J., & Yamauchi, Y. (2023). Efficient electrocatalysis for oxygen evolution: W-doped NiFe nanosheets with oxygen vacancies constructed by facile electrodeposition and

corrosion. *Chemical Engineering Journal*, *452*. https://doi.org/10.1016/j.cej.2022.139104

Li, H., Zhang, L., Wang, S., & Yu, J. (2019). Accelerated oxygen evolution kinetics on NiFeAl-layered double hydroxide electrocatalysts with defect sites prepared by electrodeposition. *International Journal of Hydrogen Energy*, *44*(54), 28556–28565. https://doi.org/10.1016/j.ijhydene.2019.09.155

Li, J. (2022). Oxygen Evolution Reaction in Energy Conversion and Storage: Design Strategies Under and Beyond the Energy Scaling Relationship. In *Nano-Micro Letters* (Vol. 14, Issue 1). Springer Science and Business Media B.V. https://doi.org/10.1007/s40820-022-00857-x

Li, J., Liu, C., Ge, J., Xing, W., & Zhu, J. (2023). Challenges and Strategies of Anion Exchange Membranes in Hydrogen-electricity Energy Conversion Devices. *Chemistry – A European Journal*, *29*(26), e202203173. https://doi.org/10.1002/CHEM.202203173

Li, L., Zhang, G., Wang, B., Yang, T., & Yang, S. (2020). Electrochemical formation of PtRu bimetallic nanoparticles for highly efficient and pH-universal hydrogen evolution reaction. *Journal of Materials Chemistry A*, *8*(4), 2090–2098. https://doi.org/10.1039/c9ta12300h

Li, S., Zhu, X., Liu, D., & Sun, F. (2018). A highly durable long side-chain polybenzimidazole anion exchange membrane for AEMFC. *Journal of Membrane Science*, *546*, 15–21. https://doi.org/10.1016/j.memsci.2017.09.064

Li, Y. S., Zhao, T. S., & Yang, W. W. (2010). Measurements of water uptake and transport properties in anion-exchange membranes. *International Journal of Hydrogen Energy*, *35*(11), 5656–5665. https://doi.org/10.1016/j.ijhydene.2010.03.026

Li, Y., Zhang, T., Deng, X., Liu, B., Ma, J., Yang, F., & Ouyang, M. (2022). Active pressure and flow rate control of alkaline water electrolyzer based on wind power prediction and 100% energy utilization in off-grid wind-hydrogen coupling

system. *Applied Energy*, *328*, 120172. https://doi.org/10.1016/j.apenergy.2022.120172

Lira Garcia Barros, R., Kraakman, J. T., Sebregts, C., van der Schaaf, J., & de Groot, M. T. (2024). Impact of an electrode-diaphragm gap on diffusive hydrogen crossover in alkaline water electrolysis. *International Journal of Hydrogen Energy*, *49*, 886–896. https://doi.org/10.1016/j.ijhydene.2023.09.280

Liu, B., Li, H., Cao, B., Jiang, J., Gao, R., & Zhang, J. (2018). Few Layered N, P Dual-Doped Carbon-Encapsulated Ultrafine MoP Nanocrystal/MoP Cluster Hybrids on Carbon Cloth: An Ultrahigh Active and Durable 3D Self-Supported Integrated Electrode for Hydrogen Evolution Reaction in a Wide pH Range. *Advanced Functional Materials*, *28*(30). https://doi.org/10.1002/adfm.201801527

Liu, L., Ma, H., Khan, M., & Hsiao, B. S. (2024). Recent Advances and Challenges in Anion Exchange Membranes Development/Application for Water Electrolysis: A Review. *Membranes*, *14*(4), 85. https://doi.org/10.3390/membranes14040085

Liu, M. J., Yang, F. H., Mei, J. C., Guo, X., Wang, H. Y., He, M. Y., Yao, Y. A., Zhang, H. F., & Liu, C. Bin. (2023). MOF Template-Derived Carbon Shell-Embedded CoP Hierarchical Nanosheet as Bifunctional Catalyst for Overall Water Splitting. *Nanomaterials*, *13*(17). https://doi.org/10.3390/nano13172421

Liu, Q., Han, J., Liu, B., Wang, Y., Pang, Y., Mu, T., Dong, K., & Zhao, C. (2025). Achieving high alkaline stability and efficient water electrolysis via multication-dipole synergistic anion exchange membranes. *Journal of Membrane Science*, *734*. https://doi.org/10.1016/j.memsci.2025.124480

Liu, X., Tian, J., Zhou, C., Jiang, J., Cheng, X., Yang, L., Wu, Q., Wang, X., & Hu, Z. (2023). Constructing membrane electrodes of low Pt areal loading with the new support of N-doped carbon nanocages for PEMFC. *FlatChem*, *40*, 100515. https://doi.org/10.1016/j.flatc.2023.100515

Liu, Y., Liu, S., Wang, Y., Zhang, Q., Gu, L., Zhao, S., Xu, D., Li, Y., Bao, J., & Dai, Z. (2018). Ru Modulation Effects in the Synthesis of Unique Rod-like Ni@Ni_2P–Ru Heterostructures and Their Remarkable Electrocatalytic Hydrogen

Evolution Performance. *Journal of the American Chemical Society*, *140*(8), 2731–2734. https://doi.org/10.1021/jacs.7b12615

Loh, A., Li, X., Sluijter, S., Shirvanian, P., Lai, Q., & Liang, Y. (2023). Design and Scale-Up of Zero-Gap AEM Water Electrolysers for Hydrogen Production. *Hydrogen*, *4*(2), 257–271. https://doi.org/10.3390/hydrogen4020018

Lu, B., Jing, Y., Yin, J., Zhu, K., Ye, K., & Li, X. (2024). NiCoP as bifunctional catalyst for efficient electrolysis of urea-assisted hydrogen production at high current density. *Journal of Power Sources*, *615*. https://doi.org/10.1016/j.jpowsour.2024.235065

Lu, Q., Yan, X., Guo, W., Li, G., Wang, J., Jiang, N., Wang, X., Ba, T., Liu, P., Zhou, J., Wang, J., Hu, L., Zhou, T., Huang, R., Hu, B., Zhang, K., & Ren, Z. (2025). Research progress on alkaline anion exchange membranes (AEMs) for the application of hydrogen production by water electrolysis. *Nano Research*, *18*(3), 94907252. https://doi.org/10.26599/NR.2025.94907252

Lu, W., Yang, Z., Huang, H., Wei, F., Li, W., Yu, Y., Gao, Y., Zhou, Y., & Zhang, G. (2020). Piperidinium-Functionalized Poly(Vinylbenzyl Chloride) Cross-linked by Polybenzimidazole as an Anion Exchange Membrane with a Continuous Ionic Transport Pathway. *Industrial & Engineering Chemistry Research*, *59*(48), 21077–21087. https://doi.org/10.1021/acs.iecr.0c04548

Luan, X., Guo, L., Li, H., Xiao, W., Xu, G., Chen, D., Li, C., Du, Y., Wu, Z., & Wang, L. (2024). Ultrafast Quasi-Solid-State Microwave Construction of Spongy Cobalt–Molybdenum Phosphide for Hydrogen Production Over Wide pH Range. *Small*. https://doi.org/10.1002/smll.202404830

Lv, H., Chen, J., Zhou, W., Shen, X., & Zhang, C. (2023). Mechanism analyses and optimization strategies for performance improvement in low-temperature water electrolysis systems via the perspective of mass transfer: A review. *Renewable and Sustainable Energy Reviews*, *183*, 113394. https://doi.org/10.1016/j.rser.2023.113394

Ma, L., & Wang, T. (2024). Rational Understanding Hydroxide Diffusion Mechanism in Anion Exchange Membranes during Electrochemical Processes with RDAnalyzer. *Angewandte Chemie International Edition*, *63*(34). https://doi.org/10.1002/anie.202403614

Mahmood, J., Li, F., Jung, S.-M., Okyay, M. S., Ahmad, I., Kim, S.-J., Park, N., Jeong, H. Y., & Baek, J.-B. (2017). An efficient and pH-universal ruthenium-based catalyst for the hydrogen evolution reaction. *Nature Nanotechnology*, *12*(5), 441–446. https://doi.org/10.1038/nnano.2016.304

Majasan, J. O., Cho, J. I. S., Dedigama, I., Tsaoulidis, D., Shearing, P., & Brett, D. J. L. (2018). Two-phase flow behaviour and performance of polymer electrolyte membrane electrolysers: Electrochemical and optical characterisation. *International Journal of Hydrogen Energy*, *43*(33), 15659–15672. https://doi.org/10.1016/j.ijhydene.2018.07.003

Makhsoos, A., Kandidayeni, M., Pollet, B. G., & Boulon, L. (2023). A perspective on increasing the efficiency of proton exchange membrane water electrolyzers– a review. In *International Journal of Hydrogen Energy* (Vol. 48, Issue 41, pp. 15341–15370). Elsevier Ltd. https://doi.org/10.1016/j.ijhydene.2023.01.048

Marius Holst, Stefan Aschbrenner, Tom Smolinka, Christopher Voglstätter, & Gunter Grimm. (2021). *Cost Forecast for Low Temperature Electrolysis-Technology Driven Bottom-Up Prognosis for Pem and Alkaline Water Electrolysis Systems*.

Meharban, F., Lin, C., Wu, X., Tan, L., Wang, H., Hu, W., Zhou, D., Li, X., & Luo, W. (2024). Scaling Up Stability: Navigating from Lab Insights to Robust Oxygen Evolution Electrocatalysts for Industrial Water Electrolysis. *Advanced Energy Materials*, *14*(41). https://doi.org/10.1002/aenm.202402886

Mei, W., Sun, L., & Zhao, Y. (2024). Overview of Hydrogen Energy and General Aspects of Water Electrolysis. In *Green Hydrogen Production by Water Electrolysis* (pp. 1–26). CRC Press. https://doi.org/10.1201/9781003368939-1

Mench, M. M. (2008). *Fuel Cell Engines*. Wiley. https://doi.org/10.1002/9780470209769

Methydor – Friendly Hydrogen Storage. (n.d.). Retrieved October 12, 2025, from https://methydor.com/#about-us

Moradi Nafchi, F., Afshari, E., & Baniasadi, E. (2024). Anion exchange membrane water electrolysis: Numerical modeling and electrochemical performance analysis. *International Journal of Hydrogen Energy*, *52*, 306–321. https://doi.org/10.1016/j.ijhydene.2023.05.173

Morandi, C. G., Peach, R., Krieg, H. M., & Kerres, J. (2015). Novel imidazolium-functionalized anion-exchange polymer PBI blend membranes. *Journal of Membrane Science*, *476*, 256–263. https://doi.org/10.1016/j.memsci.2014.11.049

Motealleh, B., Liu, Z., Masel, R. I., Sculley, J. P., Richard Ni, Z., & Meroueh, L. (2021). Next-generation anion exchange membrane water electrolyzers operating for commercially relevant lifetimes. *International Journal of Hydrogen Energy*, *46*(5), 3379–3386. https://doi.org/10.1016/j.ijhydene.2020.10.244

Msomi, P. F., Nonjola, P. T., Ndungu, P. G., & Ramontja, J. (2020). Poly (2, 6-dimethyl-1, 4-phenylene)/polysulfone anion exchange membrane blended with TiO2 with improved water uptake for alkaline fuel cell application. *International Journal of Hydrogen Energy*, *45*(53), 29465–29476. https://doi.org/10.1016/j.ijhydene.2020.08.012

Muhsen, H., Alshawabkeh, M., Al-Mahmodi, M., Ghanem, A., & Al-Halhouli, A. (2024). Sensitivity analysis of electrodes spacing media for evaluating alkaline electrolyzer performance through CFD modeling. *Renewable Energy Focus* , *49*. https://doi.org/10.1016/j.ref.2024.100575

Mulk, W. U., Aziz, A. R. A., Ismael, M. A., Ghoto, A. A., Ali, S. A., Younas, M., & Gallucci, F. (2024). Electrochemical hydrogen production through anion exchange membrane water electrolysis (AEMWE): Recent progress and associated challenges in hydrogen production. In *International Journal of Hydrogen Energy* (Vol. 94, pp. 1174–1211). Elsevier Ltd. https://doi.org/10.1016/j.ijhydene.2024.11.143

Najibah, M., Tsoy, E., Khalid, H., Chen, Y., Li, Q., Bae, C., Hnát, J., Plevová, M., Bouzek, K., Jang, J. H., Park, H. S., & Henkensmeier, D. (2021). PBI nanofiber mat-reinforced anion exchange membranes with covalently linked interfaces for use in water electrolysers. *Journal of Membrane Science*, *640*. https://doi.org/10.1016/j.memsci.2021.119832

Nara, Y., Tomita, M., Nagasawa, K., Kuroda, Y., Mitsushima, S., Kawakami, H., & Tanaka, M. (2024). All-Aromatic Polymer-Based Anion Conductive Ionomers with Different Ion Exchange Capacities for Water Electrolysis. *Advanced Engineering Materials*. https://doi.org/10.1002/adem.202400252

Nasrallah H, S. & Jemni, A. (1997). Heat and mass transfer models in metal-hydrogen reactor. *International Journal of Hydrogen Energy*, *22*(1), 67–76. https://doi.org/10.1016/S0360-3199(96)00039-0

Nechache, A., & Hody, S. (2021). Alternative and innovative solid oxide electrolysis cell materials: A short review. *Renewable and Sustainable Energy Reviews*, *149*, 111322. https://doi.org/10.1016/j.rser.2021.111322

Niblett, D., Delpisheh, M., Ramakrishnan, S., & Mamlouk, M. (2024). Review of next generation hydrogen production from offshore wind using water electrolysis. *Journal of Power Sources*, *592*, 233904. https://doi.org/10.1016/j.jpowsour.2023.233904

Aminaho, E. N., Aminaho, N. S., & Aminaho, F. (2025). Techno-economic assessments of electrolyzers for hydrogen production. Applied Energy, 399, 126515. https://doi.org/10.1016/j.apenergy.2025.126515

NIST Chemistry WebBook. (n.d.). Retrieved November 13, 2025, from https://webbook.nist.gov/chemistry/

Noor Azam, A. M. I., Ragunathan, T., Zulkefli, N. N., Masdar, M. S., Majlan, E. H., Mohamad Yunus, R., Shamsul, N. S., Husaini, T., & Shaffee, S. N. A. (2023). Investigation of Performance of Anion Exchange Membrane (AEM) Electrolysis with Different Operating Conditions. *Polymers*, *15*(5). https://doi.org/10.3390/polym15051301

Noussan, M., Raimondi, P. P., Scita, R., & Hafner, M. (2020). The Role of Green and Blue Hydrogen in the Energy Transition—A Technological and Geopolitical Perspective. *Sustainability*, *13*(1), 298. https://doi.org/10.3390/su13010298

Nyamsi, S. N., & Tolj, I. (2024). Metal hydride reactors and phase change materials: Enhancing energy storage for medium-high power vehicles. *Journal of Energy Storage*, *104*, 114545. https://doi.org/10.1016/j.est.2024.114545

Nzaba Madila, E. E., Makhsoos, A., Shanbhag, M. M., & Pollet, B. G. (2025). Advancements in electrolyser stack performance: A comprehensive review of Latest technologies and efficiency strategies. *International Journal of Hydrogen Energy*, *144*, 1168–1189. https://doi.org/10.1016/j.ijhydene.2025.04.047

Ostwald, W. (1890). *Elektrische Eigenschaften halbdurchlässiger Scheidewände*.

Ouabi, H., Lajouad, R., Kissaoui, M., & El Magri, A. (2024). Hydrogen production by water electrolysis driven by a photovoltaic source: A review. *E-Prime - Advances in Electrical Engineering, Electronics and Energy*, *8*, 100608. https://doi.org/10.1016/j.prime.2024.100608

Owner's Manual Electrolyzer 4.1. (n.d.). Retrieved October 12, 2025, from www.enapter.com

Palmas, S., Rodriguez, J., Mais, L., Mascia, M., Herrando, M. C., & Vacca, A. (2023). Anion exchange membrane: A valuable perspective in emerging technologies of low temperature water electrolysis. *Current Opinion in Electrochemistry*, *37*, 101178. https://doi.org/10.1016/j.coelec.2022.101178

Park, H., & Kohl, P. A. (2023). Alkaline membrane water electrolysis performance improvement from high ionic strength anolyte. *Journal of Power Sources*, *585*, 233643. https://doi.org/10.1016/j.jpowsour.2023.233643

Park, J. E., Kang, S. Y., Oh, S.-H., Kim, J. K., Lim, M. S., Ahn, C.-Y., Cho, Y.-H., & Sung, Y.-E. (2019). High-performance anion-exchange membrane water electrolysis. *Electrochimica Acta*, *295*, 99–106. https://doi.org/10.1016/j.electacta.2018.10.143

Park, Y. S., Jang, M. J., Jeong, J. Y., Lee, J., Jeong, J., Kim, C., Yang, J., & Choi, S. M. (2023). Optimization of Ionomer Content in Anode Catalyst Layer for Improving Performance of Anion Exchange Membrane Water Electrolyzer. *International Journal of Energy Research*, *2023*. https://doi.org/10.1155/2023/3764096

Park, Y. S., Yang, J., Lee, J., Jang, M. J., Jeong, J., Choi, W.-S., Kim, Y., Yin, Y., Seo, M. H., Chen, Z., & Choi, S. M. (2020). Superior performance of anion exchange membrane water electrolyzer: Ensemble of producing oxygen vacancies and controlling mass transfer resistance. *Applied Catalysis B: Environmental*, *278*, 119276. https://doi.org/10.1016/j.apcatb.2020.119276

Parra, D., Gillott, M., & Walker, G. S. (2016). Design, testing and evaluation of a community hydrogen storage system for end user applications. *International Journal of Hydrogen Energy*, *41*(10), 5215–5229. https://doi.org/10.1016/j.ijhydene.2016.01.098

Patcharavorachot, Y., Chalee, W., Saebea, D., & Arpornwichanop, A. (2023). Performance improvement of the proton-conducting solid oxide electrolysis cell coupled with dry methane reforming. *International Journal of Hydrogen Energy*, *48*(18), 6705–6721. https://doi.org/10.1016/j.ijhydene.2022.07.153

Photovoltaic Thermal (PV/T) Hybrid Solar Panel - MATLAB & Simulink. (n.d.). Retrieved November 12, 2025, from https://ch.mathworks.com/help/sps/ug/photovoltaic-thermal-pvt-hybrid-solar-panel.html

Qi, R., Gao, X., Lin, J., Song, Y., Wang, J., Qiu, Y., & Liu, M. (2021). Pressure control strategy to extend the loading range of an alkaline electrolysis system. *International Journal of Hydrogen Energy*, *46*(73), 35997–36011. https://doi.org/10.1016/j.ijhydene.2021.08.069

Rabillard, L., Thappily, P., Matheswaran, P., Inguanta, R., Kim, M., Lipkin, M., Kozlova, T. V., Latieff, F., & Mandin, P. (2025). Experimental Investigation of two low-cost 5 kW alkaline electrolyzer prototypes' performances depending on

size and applied voltage. *International Journal of Hydrogen Energy*, *125*, 100–107. https://doi.org/10.1016/j.ijhydene.2025.03.418

Raju, M., & Khaitan, S. (2011). Charging dynamics of metal hydride hydrogen storage bed for small wind hybrid systems. *International Journal of Hydrogen Energy*, *36*(17), 10797–10807. https://doi.org/10.1016/j.ijhydene.2011.05.144

Rasal, A. S., Chen, H. M., & Yu, W.-Y. (2024). Electronic structure engineering of electrocatalyst for efficient urea oxidation reaction. *Nano Energy*, *121*, 109183. https://doi.org/10.1016/j.nanoen.2023.109183

Razmjooei, F., Farooqui, A., Reissner, R., Gago, A. S., Ansar, S. A., & Friedrich, K. A. (2020). Elucidating the Performance Limitations of Alkaline Electrolyte Membrane Electrolysis: Dominance of Anion Concentration in Membrane Electrode Assembly. *ChemElectroChem*, *7*(19), 3951–3960. https://doi.org/10.1002/celc.202000605

Ren, Z., Wang, J., Yu, Z., Zhang, C., Gao, S., & Wang, P. (2022). Experimental studies and modeling of a 250-kW alkaline water electrolyzer for hydrogen production. *Journal of Power Sources*, *544*. https://doi.org/10.1016/j.jpowsour.2022.231886

Riaz, M. A., Trogadas, P., Aymé-Perrot, D., Sachs, C., Dubouis, N., Girault, H., & Coppens, M.-O. (2025). Water electrolysis technologies: the importance of new cell designs and fundamental modelling to guide industrial-scale development. *Energy & Environmental Science*, *18*(11), 5190–5214. https://doi.org/10.1039/D4EE05559D

Rizwan, M., Alstad, V., & Jäschke, J. (2021). Design considerations for industrial water electrolyzer plants. *International Journal of Hydrogen Energy*, *46*(75), 37120–37136. https://doi.org/10.1016/j.ijhydene.2021.09.018

Rodríguez, J., & Amores, E. (2020). CFD Modeling and Experimental Validation of an Alkaline Water Electrolysis Cell for Hydrogen Production. *Processes*, *8*(12), 1634. https://doi.org/10.3390/pr8121634

Rossi, R., Taylor, R., & Logan, B. E. (2023). Increasing the Electrolyte Salinity to Improve the Performance of Anion Exchange Membrane Water Electrolyzers. *ACS Sustainable Chemistry and Engineering*, *11*(23), 8573–8579. https://doi.org/10.1021/acssuschemeng.3c01245

Sakas, G., Rentschler, P., Kosonen, A., Holtappels, P., Ruuskanen, V., Kauranen, P., Ahola, J., & Dittmeyer, R. (2025). Dynamic mass and energy balance model of a 50 kW proton exchange membrane electrolyzer system. *Applied Energy*, *382*, 125199. https://doi.org/10.1016/j.apenergy.2024.125199

Salehmin, M. N. I., Husaini, T., Goh, J., & Sulong, A. B. (2022). High-pressure PEM water electrolyser: A review on challenges and mitigation strategies towards green and low-cost hydrogen production. In *Energy Conversion and Management* (Vol. 268). Elsevier Ltd. https://doi.org/10.1016/j.enconman.2022.115985

Salma, U., Zhang, D., & Nagao, Y. (2020). Imidazolium-Functionalized Fluorene-Based Anion Exchange Membrane (AEM) for Fuel Cell Applications. *ChemistrySelect*, *5*(4), 1255–1263. https://doi.org/10.1002/slct.201903246

Sana, B., Das, A., & Jana, T. (2019). Polybenzimidazole as alkaline anion exchange membrane with twin hydroxide ion conducting sites. *Polymer*, *172*, 213–220. https://doi.org/10.1016/j.polymer.2019.03.078

Sandstede, G., Cairns, E. J., Bagotsky, V. S., & Wiesener, K. (2010). History of low temperature fuel cells. In *Handbook of Fuel Cells*. Wiley. https://doi.org/10.1002/9780470974001.f104011

Sankar, S., Roby, S., Kuroki, H., Miyanishi, S., Tamaki, T., Anilkumar, G. M., & Yamaguchi, T. (2023). High-Performing Anion Exchange Membrane Water Electrolysis Using Self-Supported Metal Phosphide Anode Catalysts and an Ether-Free Aromatic Polyelectrolyte. *ACS Sustainable Chemistry & Engineering*, *11*(3), 854–865. https://doi.org/10.1021/acssuschemeng.2c03663

Scheepers, F., Stähler, M., Stähler, A., Rauls, E., Müller, M., Carmo, M., & Lehnert, W. (2021). Temperature optimization for improving polymer electrolyte

membrane-water electrolysis system efficiency. *Applied Energy*, *283*, 116270. https://doi.org/10.1016/j.apenergy.2020.116270

Sebbahi, S., Assila, A., Alaoui Belghiti, A., Laasri, S., Kaya, S., Hlil, E. K., Rachidi, S., & Hajjaji, A. (2024). A comprehensive review of recent advances in alkaline water electrolysis for hydrogen production. *International Journal of Hydrogen Energy*, *82*, 583–599. https://doi.org/10.1016/j.ijhydene.2024.07.428

Segawa, Y., Endo, N., Shimoda, E., Yamane, T., & Maeda, T. (2024). Pilot-scale hydrogen energy utilization system demonstration: A case study of a commercial building with supply and utilization of off-site green hydrogen. *International Journal of Hydrogen Energy*, *50*, 26–36. https://doi.org/10.1016/j.ijhydene.2023.06.294

Shaik, S., Kundu, J., Yuan, Y., Chung, W., Han, D., Lee, U., Huang, H., & Choi, S. (2024). Recent Progress and Perspective in Pure Water-Fed Anion Exchange Membrane Water Electrolyzers. *Advanced Energy Materials*, *14*(35). https://doi.org/10.1002/aenm.202401956

Shaya, N., & Glöser-Chahoud, S. (2024). A Review of Life Cycle Assessment (LCA) Studies for Hydrogen Production Technologies through Water Electrolysis: Recent Advances. In *Energies* (Vol. 17, Issue 16). Multidisciplinary Digital Publishing Institute (MDPI). https://doi.org/10.3390/en17163968

Shen, H., Gao, F.-Y., Li, H., Xu, J., Jaroniec, M., Zheng, Y., & Qiao, S.-Z. (2025). Durable Anion Exchange Membrane Water Electrolysis in Low-Alkaline Concentration Electrolyte. *Journal of the American Chemical Society*, *147*(26), 22677–22685. https://doi.org/10.1021/jacs.5c04194

Shih, A. J., Monteiro, M. C. O., Dattila, F., Pavesi, D., Philips, M., da Silva, A. H. M., Vos, R. E., Ojha, K., Park, S., van der Heijden, O., Marcandalli, G., Goyal, A., Villalba, M., Chen, X., Gunasooriya, G. T. K. K., McCrum, I., Mom, R., López, N., & Koper, M. T. M. (2022). Water electrolysis. *Nature Reviews Methods Primers*, *2*(1), 84. https://doi.org/10.1038/s43586-022-00164-0

Shiva Kumar, S., & Lim, H. (2022). An overview of water electrolysis technologies for green hydrogen production. *Energy Reports*, *8*, 13793–13813. https://doi.org/10.1016/j.egyr.2022.10.127

Siracusano, S., Baglio, V., Briguglio, N., Brunaccini, G., Di Blasi, A., Stassi, A., Ornelas, R., Trifoni, E., Antonucci, V., & Aricò, A. S. (2012). An electrochemical study of a PEM stack for water electrolysis. *International Journal of Hydrogen Energy*, *37*(2), 1939–1946. https://doi.org/10.1016/j.ijhydene.2011.06.019

Sirisomboonchai, S. (2020). *Developing highly efficient and durable electrocatalysts for water splitting over a wide pH range*.

Solar Cell - Photovoltaic solar cell - MATLAB. (n.d.). Retrieved November 12, 2025, from https://ch.mathworks.com/help/sps/ref/solarcell.html

Sun, L. X., Choo, Y. S. L., Gao, W. T., Gao, X. L., Chen, J. H., Cai, Z. H., Wang, J. J., Zhang, Q. G., Zhu, A. M., & Liu, Q. L. (2022). Self-Assembly of Porphyrin to Realize the High Ionic Conductivity of Anion-Exchange Membranes. *ACS Applied Energy Materials*, *5*(12), 15809–15818. https://doi.org/10.1021/acsaem.2c03348

Tamilarasi, B., Jithul, K. P., & Pandey, J. (2024). Non-noble metal-based electro-catalyst for the oxygen evolution reaction (OER): Towards an active & stable electro-catalyst for PEM water electrolysis. *International Journal of Hydrogen Energy*, *58*, 556–582. https://doi.org/10.1016/J.IJHYDENE.2024.01.222

Tan, L., Wang, H., Qi, C., Peng, X., Pan, X., Wu, X., Wang, Z., Ye, L., Xiao, Q., Luo, W., Gao, H., Hou, W., Li, X., & Zhan, T. (2024). Regulating Pt electronic properties on NiFe layered double hydroxide interface for highly efficient alkaline water splitting. *Applied Catalysis B: Environmental*, *342*, 123352. https://doi.org/10.1016/j.apcatb.2023.123352

Tang, J., Su, C., Zhong, Y., & Shao, Z. (2021). Oxide-based precious metal-free electrocatalysts for anion exchange membrane fuel cells: from material design to cell applications. *Journal of Materials Chemistry A*, *9*(6), 3151–3179. https://doi.org/10.1039/D0TA09346G

Tang, R., Yang, Y., Zhou, Y., & Yu, X. Y. (2024). Rational Design of Heterostructured Ru Cluster-Based Catalyst for pH Universal Hydrogen Evolution Reaction and High-Performance Zn-H2O Battery. *Advanced Functional Materials*, *34*(5). https://doi.org/10.1002/adfm.202301925

Tang, W., Yang, Y., Liu, X., Dong, J., Li, H., & Yang, J. (2021). Long side-chain quaternary ammonium group functionalized polybenzimidazole based anion exchange membranes and their applications. *Electrochimica Acta*, *391*. https://doi.org/10.1016/j.electacta.2021.138919

Tang, Z., Wu, B., Yan, K., Luo, J., Haq, M. U., & Zeng, L. (2025). Long-term stability for anion exchange membrane water electrolysis: Recent development and future perspectives. *Future Batteries*, *5*, 100024. https://doi.org/10.1016/j.fub.2025.100024

Thangavel, P., Lee, H., Kong, T. H., Kwon, S., Tayyebi, A., Lee, J. hoon, Choi, S. M., & Kwon, Y. (2023). Immobilizing Low-Cost Metal Nitrides in Electrochemically Reconstructed Platinum Group Metal (PGM)-Free Oxy-(Hydroxides) Surface for Exceptional OER Kinetics in Anion Exchange Membrane Water Electrolysis. *Advanced Energy Materials*, *13*(6). https://doi.org/10.1002/aenm.202203401

Tijani, A. S., Binti Kamarudin, N. A., & Binti Mazlan, F. A. (2018). Investigation of the effect of charge transfer coefficient (CTC) on the operating voltage of polymer electrolyte membrane (PEM) electrolyzer. *International Journal of Hydrogen Energy*, *43*(19), 9119–9132. https://doi.org/10.1016/j.ijhydene.2018.03.111

Titheridge, L. J., & Marshall, A. T. (2024). Techno-economic modelling of AEM electrolysis systems to identify ideal current density and aspects requiring further research. *International Journal of Hydrogen Energy*, *49*, 518–532. https://doi.org/10.1016/j.ijhydene.2023.08.181

Tong, L., Xiao, J., Yang, T., Bénard, P., & Chahine, R. (2019). Complete and reduced models for metal hydride reactor with coiled-tube heat exchanger. *International*

Journal of Hydrogen Energy, *44*(30), 15907–15916. *https://doi.org/10.1016/j.ijhydene.2018.07.102*

Trina Solar. (2017). Duomax dual glass 60-cell photovoltaic module (TSM-DEG5-60C-280W): Product datasheet (Version TSM_EN_2018_A). https://www.trinasolar.com

Tuckerman, M. E., Marx, D., & Parrinello, M. (2002). The nature and transport mechanism of hydrated hydroxide ions in aqueous solution. *Nature*, *417*(6892), 925–929. https://doi.org/10.1038/nature00797

Valverde, L., Pino, F. J., Guerra, J., & Rosa, F. (2016). Definition, analysis and experimental investigation of operation modes in hydrogen-renewable-based power plants incorporating hybrid energy storage. *Energy Conversion and Management*, *113*, 290–311. https://doi.org/10.1016/j.enconman.2016.01.036

Varcoe, J. R., Atanassov, P., Dekel, D. R., Herring, A. M., Hickner, M. A., Kohl, P. A., Kucernak, A. R., Mustain, W. E., Nijmeijer, K., Scott, K., Xu, T., & Zhuang, L. (2014). Anion-exchange membranes in electrochemical energy systems. In *Energy and Environmental Science* (Vol. 7, Issue 10, pp. 3135–3191). Royal Society of Chemistry. https://doi.org/10.1039/c4ee01303d

Vincent, I., Kruger, A., & Bessarabov, D. (2018). Hydrogen Production by water Electrolysis with an Ultrathin Anion-exchange membrane (AEM). *International Journal of Electrochemical Science*, *13*(12), 11347–11358. https://doi.org/10.20964/2018.12.84

Vincent, I., Lee, E.-C., & Kim, H.-M. (2021). Comprehensive impedance investigation of low-cost anion exchange membrane electrolysis for large-scale hydrogen production. *Scientific Reports*, *11*(1), 293. https://doi.org/10.1038/s41598-020-80683-6

Vinodh, R., Kalanur, S. S., Natarajan, S. K., & Pollet, B. G. (2023). Recent Advancements of Polymeric Membranes in Anion Exchange Membrane Water Electrolyzer (AEMWE): A Critical Review. *Polymers*, *15*(9), 2144. https://doi.org/10.3390/polym15092144

Vogt, H., & Balzer, R. J. (2005). The bubble coverage of gas-evolving electrodes in stagnant electrolytes. *Electrochimica Acta*, *50*(10), 2073–2079. https://doi.org/10.1016/j.electacta.2004.09.025

Volk, E. K., Kreider, M. E., Kwon, S., & Alia, S. M. (2024). Recent progress in understanding the catalyst layer in anion exchange membrane electrolyzers – durability, utilization, and integration. *EES Catalysis*, *2*(1), 109–137. https://doi.org/10.1039/D3EY00193H

Wang, C., Mo, B., He, Z., Xie, X., Zhao, C. X., Zhang, L., Shao, Q., Guo, X., Wujcik, E. K., & Guo, Z. (2018). Hydroxide ions transportation in polynorbornene anion exchange membrane. *Polymer*, *138*, 363–368. https://doi.org/10.1016/j.polymer.2018.01.079

Wang, C. R., Stansberry, J. M., Mukundan, R., Chang, H.-M. J., Kulkarni, D., Park, A. M., Plymill, A. B., Firas, N. M., Liu, C. P., Lang, J. T., Lee, J. K., Tolouei, N. E., Morimoto, Y., Wang, C., Zhu, G., Brouwer, J., Atanassov, P., Capuano, C. B., Mittelsteadt, C., … Zenyuk, I. V. (2025). Proton Exchange Membrane (PEM) Water Electrolysis: Cell-Level Considerations for Gigawatt-Scale Deployment. *Chemical Reviews*, *125*(3), 1257–1302. https://doi.org/10.1021/acs.chemrev.3c00904

Wang, C., Zhou, Z., Zhou, T., Luo, X., Gao, A., Zhou, Y., Yang, X., Li, Z., Yang, Q., & Qiao, J. (2024). Microstructural Tuning of High-Performance Bacterial Cellulose Anion Exchange Membranes via Constrained In Situ Polymerization and Double Chemical Cross-Linking. *Advanced Functional Materials*. https://doi.org/10.1002/adfm.202410009

Wang, H., Sun, F., Qi, J., Zhang, D., Sun, H., Wang, Q., Li, Z., Wu, Y. A., Hu, Z., & Wang, B. (2022). Recent progress on layered double hydroxides: comprehensive regulation for enhanced oxygen evolution reaction. In *Materials Today Energy* (Vol. 27). Elsevier Ltd. https://doi.org/10.1016/j.mtener.2022.101036

Wang, R., Ohashi, M., Ishida, M., & Ito, H. (2022). Water transport analysis during cathode dry operation of anion exchange membrane water electrolysis.

International Journal of Hydrogen Energy, *47*(97), 40835–40848. https://doi.org/10.1016/j.ijhydene.2022.09.181

Wang, T., Wang, X., Liu, Y., Zheng, J., & Li, X. (2016). A highly efficient and stable biphasic nanocrystalline Ni–Mo–N catalyst for hydrogen evolution in both acidic and alkaline electrolytes. *Nano Energy*, *22*, 111–119. https://doi.org/10.1016/j.nanoen.2016.02.023

Wei, X., Sharma, S., Waeber, A., Wen, D., Sampathkumar, S. N., Margni, M., Maréchal, F., & Van herle, J. (2024). Comparative life cycle analysis of electrolyzer technologies for hydrogen production: Manufacturing and operations. *Joule*, *8*(12), 3347–3372. https://doi.org/10.1016/j.joule.2024.09.007

Wijaya, G. H. A., Im, K. S., & Nam, S. Y. (2024). Advancements in commercial anion exchange membranes: A review of membrane properties in water electrolysis applications. *Desalination and Water Treatment*, *320*, 100605. https://doi.org/10.1016/j.dwt.2024.100605

Wolf, S. E., Winterhalder, F. E., Vibhu, V., de Haart, L. G. J. (Bert), Guillon, O., Eichel, R.-A., & Menzler, N. H. (2023). Solid oxide electrolysis cells – current material development and industrial application. *Journal of Materials Chemistry A*, *11*(34), 17977–18028. https://doi.org/10.1039/D3TA02161K

Wu, W., Ma, X., Zhu, Y., Hu, F., Huang, G., Wang, N., Ning, S., Zhu, Y., Kang Shen, P., & Zhu, J. (2023). Co2P-Fe2P heterogeneous nanoparticles: Efficient hydrogen oxidation/evolution electrocatalysts and surface reconstruction in alkaline media. *Chemical Engineering Journal*, *478*. https://doi.org/10.1016/j.cej.2023.147425

Xia, L., Holtwerth, S., Rodenbücher, C., Lehnert, W., Shviro, M., & Müller, M. (2024). Effects of mechanical pressure on anion exchange membrane water electrolysis: A non-negligible yet neglected factor. *Journal of Power Sources*, *590*, 233802. https://doi.org/10.1016/j.jpowsour.2023.233802

Xia, Y., Cheng, H., He, H., Hu, Z., & Wei, W. (2024). Efficiency Enhancement for Alkaline Water Electrolyzers Directly Driven by Fluctuating PV Power. *IEEE*

Transactions on Industrial Electronics, *71*(6), 5755–5765. https://doi.org/10.1109/TIE.2023.3288146

Xia, Y., Cheng, H., He, H., & Wei, W. (2023). Efficiency and consistency enhancement for alkaline electrolyzers driven by renewable energy sources. *Communications Engineering 2023 2:1*, *2*(1), 1–13. https://doi.org/10.1038/s44172-023-00070-7

Xie, Y., Luo, F., & Yang, Z. (2024). Strategies for the enhancements in catalytic performance and stability of anodic electrocatalyst in PEM water splitting. *Energy Reviews*, 100103. https://doi.org/10.1016/j.enrev.2024.100103

Xing, M., Zhu, S., Zeng, X., Wang, S., Liu, Z., & Cao, D. (2023). Amorphous/Crystalline Rh(OH)3/CoP Heterostructure with Hydrophilicity/ Aerophobicity Feature for All-pH Hydrogen Evolution Reactions. *Advanced Energy Materials*, *13*(44). https://doi.org/10.1002/aenm.202302376

Xu, Q., Zhang, L., Zhang, J., Wang, J., Hu, Y., Jiang, H., & Li, C. (2022). Anion Exchange Membrane Water Electrolyzer: Electrode Design, Lab-Scaled Testing System and Performance Evaluation. *EnergyChem*, *4*(5), 100087. https://doi.org/10.1016/j.enchem.2022.100087

Xu, Y., Cai, S., Chi, B., & Tu, Z. (2023). Technological limitations and recent developments in a solid oxide electrolyzer cell: A review. *International Journal of Hydrogen Energy*. https://doi.org/10.1016/j.ijhydene.2023.08.314

Xu, Y., Cai, S., Chi, B., & Tu, Z. (2024). Technological limitations and recent developments in a solid oxide electrolyzer cell: A review. *International Journal of Hydrogen Energy*, *50*, 548–591. https://doi.org/10.1016/j.ijhydene.2023.08.314

Xu, Y., Zhang, X., Liu, Y., Wang, R., Yang, Y., & Chen, J. (2022). A critical review of research progress for metal alloy materials in hydrogen evolution and oxygen evolution reaction. *Environmental Science and Pollution Research*, *30*(5), 11302–11320. https://doi.org/10.1007/s11356-022-24728-5

Xue, J., Zhang, J., Liu, X., Huang, T., Jiang, H., Yin, Y., Qin, Y., & Guiver, M. D. (2022). Toward alkaline-stable anion exchange membranes in fuel cells: cycloaliphatic quaternary ammonium-based anion conductors. *Electrochemical Energy Reviews*, *5*(2), 348–400. https://doi.org/10.1007/s41918-021-00105-7

Yang, J., Lam, T. Y., Luo, Z., Cheng, Q., Wang, G., & Yao, H. (2025). Renewable energy driven electrolysis of water for hydrogen production, storage, and transportation. In *Renewable and Sustainable Energy Reviews* (Vol. 218). Elsevier Ltd. https://doi.org/10.1016/j.rser.2025.115804

Yang, R., Wu, X., Chen, W., Wang, X., Li, T., Yan, X., Wang, L., Cui, F., & He, G. (2023). Engineering of Interconnected Ionic Channels in Polybenzimidazole Anion-Exchange Membranes. *Industrial & Engineering Chemistry Research*, *62*(41), 16746–16756. https://doi.org/10.1021/acs.iecr.3c02220

Younus, H. A., Al Hajri, R., Ahmad, N., Al-Jammal, N., Verpoort, F., & Al Abri, M. (2025). Green hydrogen production and deployment: opportunities and challenges. *Discover Electrochemistry 2025 2:1*, *2*(1), 1–38. https://doi.org/10.1007/S44373-025-00043-9

Yu, R., Cao, X., Chen, Q., Li, W., Huang, A., Wei, X., & Mao, J. (2023). D-Band Center Optimization of Edge-Rich Ultrathin RuZn Nanosheets With Moiré Superlattices for pH-Universal Hydrogen Evolution Reaction. *Small*, *19*(40). https://doi.org/10.1002/smll.202303440

Yu, Z., Tsen, W.-C., Qu, T., Cheng, F., Hu, F., Liu, H., Wen, S., & Gong, C. (2023). Highly ion-conductive anion exchange membranes with superior mechanical properties based on polymeric ionic liquid filled functionalized bacterial cellulose for alkaline fuel cells. *Journal of Materials Research and Technology*, *23*, 6187–6199. https://doi.org/10.1016/j.jmrt.2023.02.197

Zelovich, T., Vogt-Maranto, L., Hickner, M. A., Paddison, S. J., Bae, C., Dekel, D. R., & Tuckerman, M. E. (2019). Hydroxide Ion Diffusion in Anion-Exchange Membranes at Low Hydration: Insights from Ab Initio Molecular Dynamics.

Chemistry of Materials, *31*(15), 5778–5787. https://doi.org/10.1021/acs.chemmater.9b01824

Zhan, Y., Gao, X., Situ, A., Huang, R., Zhang, Z., Pang, Z., Zhang, J., Guan, X., Tang, X., Wu, X., & Chen, Z. (2024). Sub-2.5 nm monodisperse Mo2C nanoparticles on N-doped carbon: The facet engineering for boosting electrochemical hydrogen evolution. *International Journal of Hydrogen Energy*, *71*, 1326–1333. https://doi.org/10.1016/j.ijhydene.2024.05.341

Zhang, B., Hua, Y., & Gao, Z. (2022). Strategies to optimize water management in anion exchange membrane fuel cells. *Journal of Power Sources*, *525*, 231141. https://doi.org/10.1016/j.jpowsour.2022.231141

Zhang, J., Wang, T., Liu, P., Liu, S., Dong, R., Zhuang, X., Chen, M., & Feng, X. (2016). Engineering water dissociation sites in MoS2 nanosheets for accelerated electrocatalytic hydrogen production. *Energy and Environmental Science*, *9*(9), 2789–2793. https://doi.org/10.1039/c6ee01786j

Zhang, K., McDonald, M. B., Genina, I. E. A., & Hammond, P. T. (2018). A Highly Conductive and Mechanically Robust OH^- Conducting Membrane for Alkaline Water Electrolysis. *Chemistry of Materials*, *30*(18), 6420–6430. https://doi.org/10.1021/acs.chemmater.8b02709

Zhang, M., Gao, L., Yang, L., Shan, G., Wang, Y., Huo, X., Li, W., & Zhang, J. (2024). Temperature distribution evolution in zero-gap alkaline water electrolyzer: Experimental and modeling. *Fuel*, *367*, 131418. https://doi.org/10.1016/j.fuel.2024.131418

Zhang, Q., Yuan, Y., Zhang, J., Fang, P., Pan, J., Zhang, H., Zhou, T., Yu, Q., Zou, X., Sun, Z., & Yan, F. (2024). Machine Learning-Aided Design of Highly Conductive Anion Exchange Membranes for Fuel Cells and Water Electrolyzers. *Advanced Materials*. https://doi.org/10.1002/adma.202404981

Zhang, X., Liu, B., Yang, Y., Li, J., Li, J., Zhao, Y., Jia, L., & Sun, Y. (2023). Advances in component and operation optimization of solid oxide electrolysis

cell. *Chinese Chemical Letters*, *34*(5), 108035. https://doi.org/10.1016/j.cclet.2022.108035

Zhang, X., Song, Y., Wang, G., & Bao, X. (2017). Co-electrolysis of CO2 and H2O in high-temperature solid oxide electrolysis cells: Recent advance in cathodes. *Journal of Energy Chemistry*, *26*(5), 839–853. https://doi.org/10.1016/j.jechem.2017.07.003

Zheng, W., He, L., Tang, T., Ren, R., Lee, H., Ding, G., Wang, L., & Sun, L. (2024). Poly(Dibenzothiophene-Terphenyl Piperidinium) for High-Performance Anion Exchange Membrane Water Electrolysis. *Angewandte Chemie International Edition*, *63*(34), e202405738. https://doi.org/10.1002/ANIE.202405738

Zheng, Y., Serban, A., Zhang, H., Chen, N., Song, F., & Hu, X. (2023). Anion Exchange Ionomers Enable Sustained Pure-Water Electrolysis Using Platinum-Group-Metal-Free Electrocatalysts. *ACS Energy Letters*, *8*(12), 5018–5024. https://doi.org/10.1021/acsenergylett.3c01866

Zhou, Y., Liu, Y., Tang, H., & Lin, B. L. (2023). The RuO2/NiRu heterogeneous interface optimizes the d-band center of the Ni-Ru catalyst for high-performance alkaline hydrogen evolution reaction. *Journal of Materials Chemistry A*, *11*(20), 10720–10726. https://doi.org/10.1039/d2ta09660a